ANALYSIS OF THE CENTRAL $K_S^0 K^{\pm} \pi^{\mp}$ SYSTEM AND DETERMINATION OF THE $f_1(1285)$ BRANCHING RATIO AT 450 GeV/c

Stephen Clewer

Thesis submitted for the degree of
Doctor of Philosophy

School of Physics and Space Research
Faculty of Science
University of Birmingham

December 1994

Synopsis

This thesis presents the latest results from the WA91 experiment. The experiment selects central production reactions of the type $pp \rightarrow p_f(X^0)\ p_s$ at 450 GeV/c where s and f indicates fastest and slowest particles in the laboratory frame and X^0 is the central system.

The development of code to recover V^0 vertices for the WA91 experiment is described. This code has been implemented to study channels involving K^0's. The number of K^0 s recovered by the code represented 38% of the total number available.

In the centrally produced $K^0_S K^\pm \pi^\mp$ system, clear signals for both the $f_1(1285)$ and the $f_1(1420)$ are seen. Spin-parity analysis of both mesons using Zemach tensor formalism determined that both states have quantum numbers $J^{PG} = 1^{++}$. The $f_1(1285)$ was found to decay *via* the $a_0(980)\pi$ intermediate step. The $f_1(1420)$ was found to decay *via* $K^*\overline{K}$ only, no 0^{-+} wave being required to explain the observed data. When comparison is made with 85 and 300 GeV/c central $K^0_S K^\pm \pi^\mp$ data, the relative proportion of $f_1(1285)$ to $f_1(1420)$ is found to be consistent with 300 GeV/c data, and lower than that at 85 GeV/c, indicating different energy dependences for $f_1(1285)$ and $f_1(1420)$ production.

The branching ratio

$$\frac{f_1(1285) \rightarrow K\overline{K}\pi}{f_1(1285) \rightarrow 4\pi}$$

has been determined from the $K^0_S K^\pm \pi^\mp$ and $\pi^+\pi^-\pi^+\pi^-$ channels to be 0.29 ± 0.07, consistent with the Particle Data Group value.

To my parents.

Acknowledgements

I would like to thank Professors George Morrison and John Dowell for giving me the opportunity to undertake a PhD in the School of Physics and Space Research. I must also thank the SERC, and lately the DSS, for funding me throughout my three and a bit years.

Thanks must be extended towards John Kinson, head of the Omega group at Birmingham for keeping me on the straight and narrow, and to the rest of the group for the unique atmosphere: my supervisor Noel Carney, Orlando Villalobos Baillie for being able to help sort out my many problems, and Frank Votruba, for expounding some interesting opinions at the CERN coop over the years.

Special thanks must go to Andrew Kirk, spokesman of the WA91 experiment, for always finding the time to help me and answer my inane questions, and especially for his help and suggestions throughout my long term attachment at CERN. Thanks must also go to the rest of the WA91 Collaboration, especially to the Russian (and Georgian) members of the collaboration, Goram, Irakly and the boys for the excellent meeting in Russia, including the football game/vodka drinking I'll never forget, or indeed, remember. I must particularly thank John, Orlando, Andy and Noel for reading drafts of my thesis.

In the Birmingham particle physics group at large, I must thank Pete Watkins for helping me out when I was thinking of transferring to the group, and Lawrie Lowe being able to sort out my various computer problems.

The people that made my time living in Geneva enjoyable (mostly by going to pubs) also deserve a big mention: Warren 'Only One' Matthews for shortening my life expectancy considerably with the infamous *bb's*, and for some top meals, Jason 'Chewy two-fondue' Ward for liking curries as much as me, Stuart Clowes for getting me interested in guitars, Paul Phillips for the haircuts, Rob Akers for being an inspiration for several cartoons, Tara Shears for introducing me to poetry and the ex-Brummies Dave Rees and Steve Hillier. Thanks to the mad nannies, Kate and Kay, for livening up Geneva (I'll not forget the car trip back from Verbier in a hurry!). Many thanks to the new generation: Jim 'Bobbins' Edwards for being 'steady' and Ollie Cooke. Flannagans Irish Pub certainly deserves a mention for giving us somewhere to go of an evening and serving a pretty good pint of Guinness by Geneva standards.

Thanks must also go to the people in Brum for making life more interesting: Stuart 'Nicotine' Robertson, Andy 'Off to Manchester' Bayes, the housemate who was never there, Jim 'Brassic' Clayton for trying to wind me up for the past six odd years, Rich Barnes for always being prepared to go down the pub, Mike 'pyromaniac' Haben for the explosions, Tan Ahmed, despite coming from Newport, Paul 'Long-haired Layabout' Davies, Keith Norman for bringing things out to Geneva, Tim 'Workaholic' Nicholls, Lee West, Mark 'Spoony' Pearce, Dave Rigby for lots of interesting new words and for lending me his flat in times of need. Thanks to Dave 'Vote for me' Evans, for that interesting car ride in France one sunday ('*Hold on chaps!*'), for kicking me out of my office just when I was getting comfortable, and for lots of political debate, oh yes. Many thanks to Chris 'Carsurf' Dodenhoff, fellow WA91 lad and Gutty All-Star, for the destructive interference and for introducing me to that delectable (or something) Austrian rum, *Ströh*, the taste of which I never want to know again, ever.

I must say thanks to my ex-housemates; to Ollie 'Magnet Man' Ragg, for going out on all those guilt-ridden friday nights just before our finals and for six years of 'urrh' and V-signs, Simon 'Sproing!' Franklin for making me feel guilty by working all the time as an undergraduate and for giving me a place to stay in America, and also cheers to Pete Maunder, Andy Clifford and Ashley Hall.

My thanks and love must go to Tania, not least for giving me the motivation to knuckle down and start writing this thesis in the first place, and for her continuing support during the writing up.

Thanks to all my mates back home in Wales (*Cymru*, to those in the know) for keeping a welcome in the hillsides, and especially to Neil Tucker for being a good friend and always being ready for an ale and a curry on my return. I must thank my auntie and uncle, Pat and Gary, my nan and my brother Kevin, for being ever willing to help out a poor student all those years. Lastly, but by no means least, I must thank my parents, without whose love and support none of this would have been possible, and it is to them that I dedicate this thesis.

Steve Clewer

Birmingham

December 1994.

Beset, as we were,
with science's signposts, we whimpered
to no purpose that we were lost.

R.S Thomas, *Counterpoint*

Education is an admirable thing, but it is well to remember from time to time that nothing that is worth knowing can be taught.

Oscar Wilde, *The Critic as Artist*

Tirez le rideau, la farce est joueé

François Rabelais

Contents

List of Figures

List of Tables

Chapter 1

Introduction to Gluonic states

1.1 Introduction

Scientific research has long been concerned with trying to understand nature at the most basic level, but it is only very recently that a comprehensive picture of the fundamental interactions of matter has started to emerge.

For around a century, we have known that matter is made up of molecules consisting of atoms, themselves comprised of outer negative electrons and a very dense, positive nucleus. Since the discovery of radioactivity, it became apparent that the nucleus itself was composite, being found to consist of protons and neutrons. It was thought at the time that these, along with electrons, represented the fundamental constituents of matter.

The Strong force was postulated as the force that binds the nucleus together, overcoming the electromagnetic repulsion that would otherwise force it to break apart. A particle called the pion was introduced as the mediator of this force, in analogy to the photon in electromagnetic phenomena. The pion was discovered in 1947, but the advent of higher energy accelerators in the 50's and 60's revealed that subatomic behavior was more complex than previously supposed.

Experiments revealed that the neutron, proton and pion were but the lightest in a large spectrum of particles, collectively labelled *Hadrons* (particles that respond to the strong force, as opposed to electrons, which are blind to this force). It was found that these particles could be separated into two groups, dependent upon their intrisic spin. They have either half-integral spin and are called *Baryons* (such as p,

Type	Charge	Spin	Generations		
quarks	$+\frac{2}{3}$	$\frac{1}{2}$	u	c	t
	$-\frac{1}{3}$	$\frac{1}{2}$	d	s	b
leptons	-1	$\frac{1}{2}$	e	μ	τ
	0	$\frac{1}{2}$	ν_e	ν_μ	ν_τ

Table 1.1: Standard Model quark and lepton generations.

Σ^+, Δ^-) or have integral spin and are called *Mesons* (such as π^+ and K^-).

Consideration of the patterns of the particles that were experimentally observed led to the postulate that hadrons were themselves composite, being made of even smaller objects called *quarks*, having fractional charge. The observed particles could be produced by combining these quarks into one of two different bound configurations:

$$\begin{array}{ll} \text{Baryons} & qqq \\ \text{Mesons} & q\overline{q} \end{array}$$

The other group of fundamental particles found experimentally were the *Leptons*. This group contains the familiar electron, and also the heavier muon (μ) and tau (τ) particles together with the associated neutrinos for the three particles (which are believed to be massless). There were found to be 6 different types, or *Flavours* of quarks needed to reproduce the experimentally observed particle groups, having different masses and charges. The proton, for example, is made up of two up quarks and a down quark (uud).

These fundamental particles, quarks and leptons, combined with quantum field theories that describe their interactions constitute the *Standard Model*. The different types of quarks and leptons within the Standard Model are shown in table 1.1.

Particle physics experiments worldwide are currently testing this theory and its predictions in order to ascertain how well it actually describes particle interactions, and to look for any new results that may increase our understanding of them.

1.2 Gauge theories of matter

1.2.1 Quantum Electrodynamics

Electromagnetic interactions between charged particles are described well by *Quantum Electrodynamics* (QED), where the effect of the electromagnetic force is mediated by the exchange of a virtual boson, the photon (γ). A charged particle can emit a photon, in violation of conservation of energy, as long as it exists for a time allowed by the Heisenberg Uncertainty Principle $\Delta \mathrm{t} \approx \frac{\hbar}{\Delta E}$, where ΔE is the amount of energy 'borrowed'. This emitted photon could then be absorbed by another charged particle. In this way the electromagnetic force could be 'felt' by two charged particles in proximity. For example, the repulsion of two electrons is shown in figure 1.1.

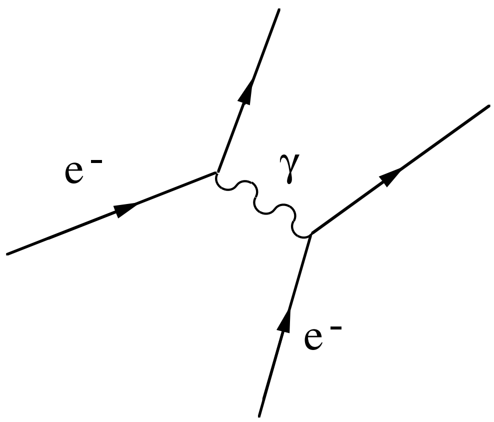

Figure 1.1: Mediation of electron repulsion *via* exchange of a virtual photon.

Interactions of this type have been described by QED and its predictions have found excellent agreement with experimental data.

The electromagnetic force, however, cannot be the force that holds particles such the proton together. A proton has two u quarks of the same charge, and hence the electromagnetic force produces a strong repulsion. The strong force, which was previously thought to act between hadrons must also be present within them, to overcome this repulsion.

1.2.2 Quantum Chromodynamics

When attempting to use the quark model to describe observed particles, the model quickly develops problems when considering particles such as the Δ^{++}, which is a uuu state, having spin $\frac{3}{2}$. This spin is produced by combining three identical u quarks in a symmetric manner. This is forbidden by Fermi statistics, which says that fermions should exist in an overall antisymmetric state, and yet is the only combination that produces the known properties of the Δ^{++}. The way this problem was solved was by the introduction of *Colour* charge. There are three 'colours' possible, labelled red, green and blue. Hence, the three u quarks in the Δ^{++} are now distinguished by their colour charge [1].

This is not, however, the only evidence for colour. Strong experimental evidence comes from e^+e^- collision data; the cross section ratio $\frac{\sigma(e^+e^- \to hadrons)}{\sigma(e^+e^- \to \mu^+\mu^-)}$, is proportional to the number of colours. From the experimentally observed data the colour factor required has the value three [2]. All states of quarks, both mesons and baryons, are believed to exist in an overall 'colourless' state; that is to say that the colour charges of the individual quarks cancel out (for the two quarks in a meson, one must have the anti-colour charge of the other for example).

The theory that describes the strong interaction is called *Quantum Chromodynamics* or QCD, and by analogy to QED the force acts through the exchange of virtual bosons, in this case *Gluons*. In the same way that the electric charge is the source of virtual photons in QED, the colour charge is the source of gluons. The gluon exchange between quarks is what binds the quarks to form mesons and baryons.

There is one very important difference between QED and QCD. The carriers of the electromagnetic interaction carry no charge, and as such are blind to each other and cannot self-interact. QED is thus described as an *Abelian* field. However the virtual gluons of QCD must carry colour charge, and as a consequence of this they will be able to interact with each other. QCD based models have predicted that because of this self-interaction, bound meson states should exist containing valence gluons.

1.2.3 Charge screening and confinement

The self-coupling of gluons has important consequences, if the effects of charge screening are compared for QED and QCD. In QED, an electron can emit a photon, or it can emit a photon that can annihilate to an e^+e^- pair, and so on. In this manner, the electron will exist not just as a 'bare' particle, but as a particle surrounded by other charged particles, positrons and electrons. This effect is illustrated in figure 1.2. Charge attraction means that the positrons will be preferentially closer to

Figure 1.2: Example of the electron loops than can be produced about a bare electron. These effects give rise to screening of the electronic charge in QED.

the electron, and in this way, the electron will be surrounded by a cloud of charge, polarized in such a way as to screen the full electron charge. The practical upshot of all this is that if one attempts to determine the electron charge by measuring the Coulomb force experienced by a test charge in the vicinity of the electron, then the result will be dependent on the position of the test charge; outside the cloud of positrons then the electron charge will be less than its true value, whereas when the test charge begins to penetrate the cloud, the observed charge will tend towards its true value. The variation of charge is calculable by considering all the possible QED configurations that can make up the cloud of charge.

The effect of colour charge surrounding a quark can also be considered in a similar manner. Colour screening around a quark should occur, the quark emitting a gluon which in turn can produce quark-antiquark pairs etc. However, because of the gluon self-coupling, then gluon vertices can be produced around the central quark as well. These effects are illustrated in figure 1.3.

Figure 1.3: Screening of the colour charge of a quark in QCD due to a) quark and b) gluon vertices.

This means that for a green quark, say, there will be more predominantly green charge near to the central quark. This is the converse of the situation in QED. If one now measures the colour charge of the quark, the colour charge will decrease on penetrating the gluon cloud. Two green quarks will interact asymptotically through colour fields of progressively reducing strength, until they behave as free, non-interacting particles. This 'antiscreening' is referred to as *Asymptotic freedom*.

Because of the colour screening, if two or more quarks are in close proximity, when they are separated their colour interaction becomes stronger. Through the interactions of gluons with one another between the two quarks, the lines of colour force concentrate between them, in a tube like region as in figure 1.4 a).

Figure 1.4: a) the q-q colour field between two quarks and b) the Coulomb field between e^+e^-.

This is different from the field connecting two electrons, as shown in figure 1.4

b). In the case of separating an e^+e^- pair, there is nothing to stop the lines of force from separating out, since the photons mediating the force cannot self-interact. The Coulomb potential energy drops off as $V(r) \propto \frac{1}{r}$. If the colour tube between the two quarks has a constant energy density per unit length, then as the two quarks separate, the potential energy between them will increase with separation, $V(r) \propto r$. The change in the observed charge with distance for both cases is illustrated in figure 1.5. This increase of colour charge at increasing separation means that the

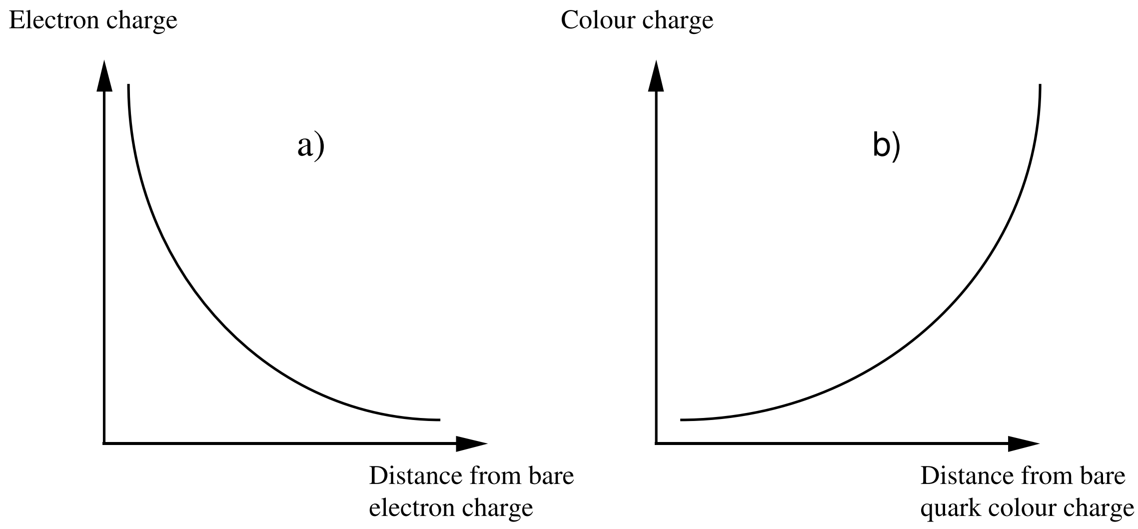

Figure 1.5: Change in the observed charge with distance for a) an electron and b) a quark.

two quarks cannot be separated. This is believed to be the reason for confinement of quarks into colourless hadrons.

1.3 Mesons

Mesons are bound quark states having integer spin. The mesons conventionally identified comprise a quark and an antiquark in a bound state, $q\overline{q}$. Since both the quark and antiquark have spin $\frac{1}{2}$, then both triplet states having $J = 1$ (*vector mesons*) and singlet states of $J = 0$ (*scalar mesons*) are expected. The parity, P, of a $q\overline{q}$ state is given by

$$P = (-1)^L(-1)$$

I	I_3	Wavefunction	Charge
1	1	$u\overline{d} = \pi^+$	+1
1	-1	$-\overline{u}d = \pi^-$	-1
1	0	$\sqrt{\frac{1}{2}}(d\overline{d} - u\overline{u}) = \pi^0$	0
0	0	$\sqrt{\frac{1}{2}}(d\overline{d} + u\overline{u}) = \eta$	0

Table 1.2: Construction of states in the $J^P = 0^-$ nonet, using only u and d quarks.

where L is the angular momentum between the two quarks. The (-1)^L comes from the space inversion under the parity operation. The other -1 arises because the q and the $\overline{q}$ have opposite intrinsic parities. The charge conjugation, C, of a $q\overline{q}$ state is given by

$$C = (-1)^{S+1}(-1)^L(-1) = (-1)^{L+S}$$

where S is the total intrinsic spin of the $q\overline{q}$ pair. Because the $q\overline{q}$ state is a bound quantum system, then it will have discrete energy levels corresponding to excited states. This leads to the conclusion that there should exist many possible mesonic states. These states should be able to be placed into groups, called nonets, each having similar mass and all having the same J^P.

Consider the lowest mass nonet, the pseudoscalars, where all the states have $J^P = 0^-$. If we consider only the u and d quarks then the combinations of table 1.2 can be constructed. The $|\eta\rangle$ is the isospin singlet state orthogonal to all the other states ($\langle\eta|\pi^0\rangle = 0$ for example). The singlet state is symmetric in quark labels if $d \rightarrow u$ and $\overline{d} \rightarrow \overline{u}$ whereas the triplet states all change sign.

If the s quark is included, then there are now nine possible states, as listed in table 1.3. These nine states break down into a singlet state, the η_0, and eight other states that can be transformed into each other by the interchange of u,d and s quarks. Note that the η_0 and η_8 are orthogonal to each other.

Nonets are conventionally represented in diagrams where the hypercharge, Y (where Y = B + S) of the particle is plotted against the projection of isospin, I_3. The two lowest lying nonets are represented in this way in figure 1.6.

I	I_3	S	Meson	Quark combination	Mass (MeV)
1	1	0	π^+	$u\overline{d}$	140
1	-1	0	π^-	$\overline{u}d$	
1	0	0	π^0	$\sqrt{\frac{1}{2}}(d\overline{d} - u\overline{u})$	135
$\frac{1}{2}$	$\frac{1}{2}$	$+1$	K^+	$u\overline{s}$	494
$\frac{1}{2}$	$-\frac{1}{2}$	$+1$	K^0	$d\overline{s}$	498
$\frac{1}{2}$	$-\frac{1}{2}$	-1	K^-	$\overline{u}s$	494
$\frac{1}{2}$	$\frac{1}{2}$	-1	$\overline{K}^0$	$\overline{d}s$	498
0	0	0	η_8	$\sqrt{\frac{1}{6}}(d\overline{d} + u\overline{u} - 2s\overline{s})$	549
0	0	0	η_0	$\sqrt{\frac{1}{3}}(d\overline{d} + u\overline{u} + s\overline{s})$	958

Table 1.3: Construction of pseudoscalar states ($J^P = 0^-$) formed from u,d and s quarks.

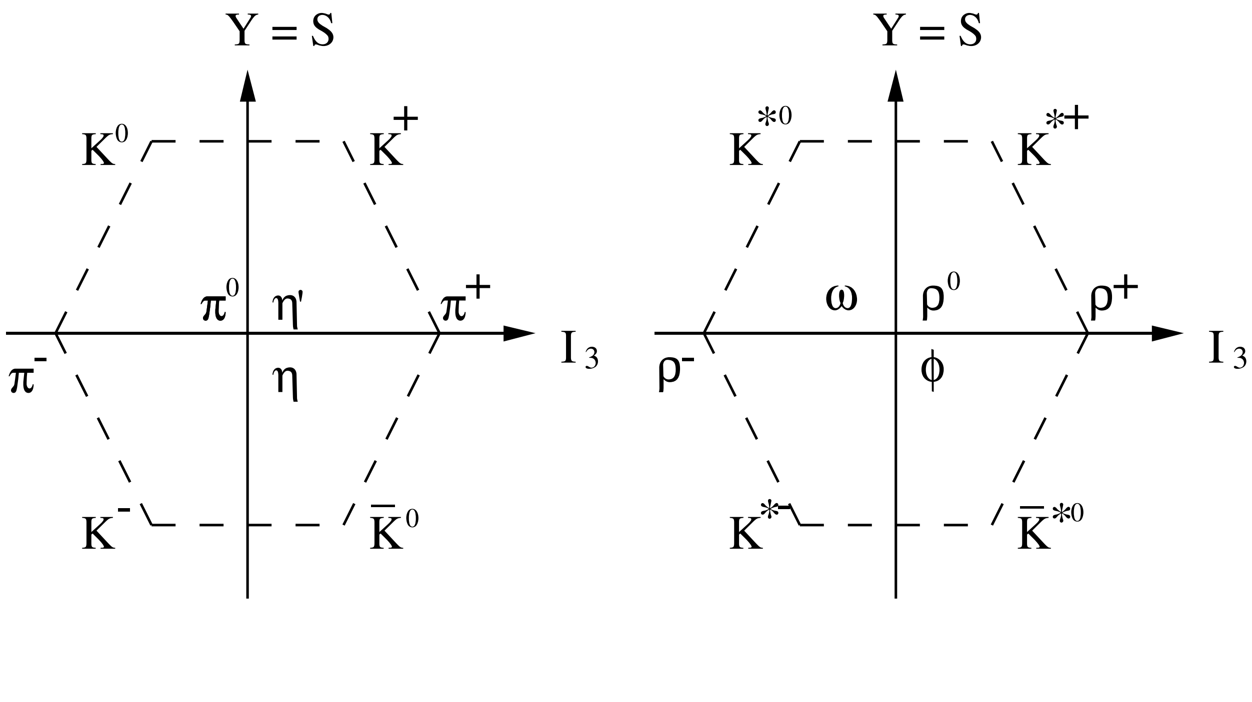

Figure 1.6: The pseudoscalar (0^-) and vector (1^-) meson nonets.

1.3.1 Mixing of States

As described above, there are two states, η_0 and η_8, which can be formed from the u, d and s quarks. There are two neutral particles that are experimentally observed with the quantum numbers $J^P = 0^-$, the η and η'. These physical states do not, however, correspond to the η_0 and η_8 states, but to quantum mechanical superpositions of the two. This is allowed since the two states have exactly the same quantum numbers. The mixing angle between the two states is approximately 11 degrees.

The same thing also occurs in the higher mass nonets. In the 1^- nonet, the neutral octet and singlet I=0 states mix so that the observed particles are to a good approximation made up of only strange or non-strange particles.

$$\phi \approx s\overline{s} \qquad \omega \approx \sqrt{\frac{1}{2}}(u\overline{u} + d\overline{d})$$

The mixing angle is approximately 40 degrees. These compositions are borne out by the decay modes of the two particles, where the dominant decay modes of both are

$$\begin{aligned} \phi &\rightarrow K^+K^- \\ &\rightarrow K^0\overline{K}^0 \quad (84\%) \\ \omega &\rightarrow \pi^+\pi^-\pi^0 \quad (90\%). \end{aligned}$$

1.3.2 Nonet assignments

One of the major concerns of meson spectroscopy is to classify observed mesonic states into nonets. The current nonet assignments for mesonic states made up of u, d and s quarks are shown in table 1.4. The masses, branching ratios and quantum numbers of these states serve to provide much information about QCD, and as such the correct identification of observed particles into nonets is an important aspect of particle physics. This task is sometimes made difficult due to the possibility of mixing of states, and there often being several states that may be reasonable candidates for a particular assignment. There may also be more than one state occupying the same mass region, making experimental resolution difficult. In addition to this,

$^{2S+1}L_J$	J^{PC}	I=1	I=0	I=$\frac{1}{2}$
$^1S_0$	0^{-+}	π	η, $\eta^{'}$	K
$^3S_1$	1^{--}	ρ	ω, ϕ	$K^*(892)$
$^1P_1$	1^{+-}	$b_1(1235)$	$h_1(1170)$, $h_1(1380)$	K_{1B}
$^3P_0$	0^{++}	$a_0(980)$	$f_0(1300)$, $f_0(980)$	$K_0^*(1430)$
$^3P_1$	1^{++}	$a_1(1260)$	$f_1(1285)$, $f_1(1510)$	K_{1A}
$^3P_2$	2^{++}	$a_2(1320)$	$f_2(1270)$, $f_2^{'}(1525)$	$K_2^*(1430)$

Table 1.4: The nonet assignments for mesons identified as $q\overline{q}$ states, for states made up of u, d and s quarks (The K_{1B} and K_{1A} states are nearly equal mixes of the $K_1(1270)$ and the $K_1(1400)$).

there are mesonic states predicted that are non $q\overline{q}$ in nature, and it is to these that we now turn.

1.4 Non-$q\overline{q}$ Mesonic States

Because of the non-Abelian nature of QCD, several different types of gluonic state are predicted to exist.

An important prediction is the existence of *Glueballs*, which are bound states of two or more gluons in an overall colour singlet. Several calculations have been made using various QCD based models in an attempt to calculate the glueball mass spectrum, but agreement between the models is only fair. However, most of the models do converge in assigning masses to lie in the 0.5 - 2 GeV/c^2 range [3], [4]. Recent predictions from lattice gauge theory [5],[6] for the lowest lying glueballs indicate that M(2^{++})/M(0^{++}) = 1.5 and that the mass of the lowest lying glueball is M(0^{++}) = 1240 - 1600 MeV.

The allowed J^{PC} values for two gluon states have been calculated from bag model considerations, and are 0^{++}, 2^{++}, 0^{-+}, 2^{-+}, in order of mass [7]. Two gluon states cannot form the 1^{++} or 1^{-+} states as a result of Yang's theorem [8]. The lowest three gluon states are predicted to have quantum numbers 0^{++}, 1^{+-}, although these states would lie higher in mass than the two gluon states. In the three gluon case then the state $J^{PC} = 1^{-+}$, which cannot be formed from $q\overline{q}$ states, is also predicted.

Another prediction is that bound states consisting of a mixture of quarks, anti-quarks and gluons (i.e. $q\overline{q}g$) should exist. These are the so-called *Hybrid* states. Recent predictions using the flux tube model [9] for the masses of the lowest lying states indicate that M $(1^{--}, 0^{-+}, 1^{-+}, 2^{-+}) \approx 1900$ MeV.

In addition, $q\overline{q}q\overline{q}$ states are believed to be possible. Bag model calculations [10] predict that the lowest lying $q\overline{q}q\overline{q}$ states would form nonets having the same quantum numbers as $q\overline{q}$ nonets. However, recent calculations for $q\overline{q}q\overline{q}$ states predict that most will break up into two colour-singlet mesons, having a decay width of the same order as their masses. This process is referred to as 'fall-apart' [11]. As such, they would be undetectable to experiment.

Molecular systems such as a bound K^*K state have also been predicted to exist and be experimentally detectable. These predictions are reviewed in [12], [7] and [13].

1.5 The experimental search for Gluonium

Over the last 30 years, hadron spectroscopy has explored the mass region where it is thought that exotic gluonic states may be found, and yet these states have not been conclusively identified. There are several possible reasons for this:

- Glueballs do not exist at all. In this case, QCD should be reviewed.
- Glueballs exist but cannot be detected, since they are very broad and form a continuum which cannot be disentangled from standard $q\overline{q}$ states.
- Some glueballs may be narrow enough to be observed, and some may already have been, but mis-identified as normal quarkonium states.
- Hadron spectroscopy has largely been carried out using reactions where the interaction is *via* channels dominated by the exchange of valence quarks as opposed to gluons, and hence the channels studied may not have been sufficiently 'glue rich' to produce glueballs.

In view of these problems, the search for exotic gluonia must proceed along the following guidelines:

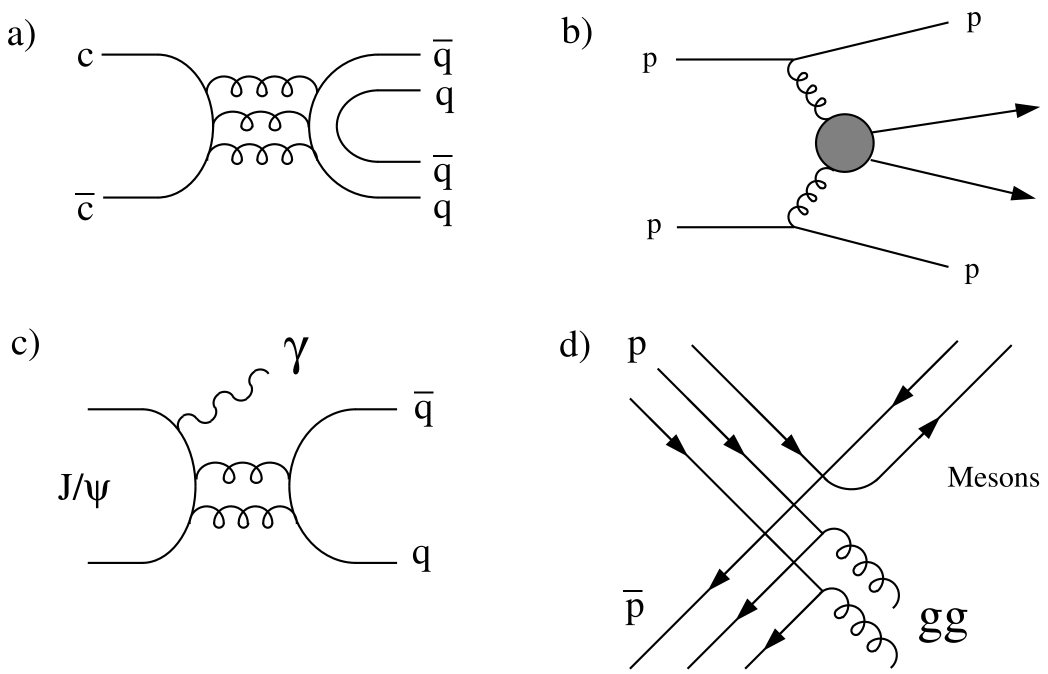

Figure 1.7: Reaction mechanisms that are believed to be gluon rich, where it is considered that gluonic states may be found.

- Look for 'oddball' states, i.e. states having J^{PC} quantum numbers that are not allowed for normal mesonic states, but which are predicted to be allowed for gluonia, e.g. $J^{PC} = 1^{-+}$.

- Normal $q\overline{q}$ states are grouped into nonets having the same J^{PC} and approximately the same mass. Hence, look for extra states with a J^{PC} of an already completed nonet, and a mass low enough for it not to be a member of the next radially excited nonet. There is a problem with this, however, in that only the lowest lying nonets are fully established. The higher mass nonets, where it is expected that the lowest mass gluonic states should occur are already crowded with $q\overline{q}$ states and their radial excitations so that the groupings into multiplets are far from certain. Because of this, for any new resonances found, it will be difficult to prove that they are of a non-$q\overline{q}$ nature.

- To look for states preferentially produced in gluon rich processes. If a resonance appears in a process that is believed to involve a gluonic mechanism, whilst it is suppressed in other processes then this may give some indication of

an exotic nature. For example, $\gamma\gamma$ collisions are thought not to be gluonium producing reactions since γs do not couple directly to gluons. Examples of processes that are believed to be gluon rich are shown in figure 1.7. They are:
(i) The hadronic (a) or radiative (c) J/Ψ decay.
(ii) Central production *via* Double Pomeron Exchange (DPE), as shown in figure 1.7 b). The pomeron is an object that is thought to be a multi-gluonic state, and DPE is thus essentially gluon-gluon scattering. It is this process that is studied by the WA91 experiment at CERN. The experimental setup that selects this reaction will be discussed in greater depth in the chapter 2.
(iii) Proton-antiproton scattering (fig 1.7 d) where the annihilation region is a source of gluons, and thus may form a suitable area where gluonic states may be formed.

It is hoped that by employment of the above methods, states may be found which will have an unambiguous non-$q\overline{q}$ assignment.

1.6 Some non-$q\overline{q}$ candidates

1.6.1 The $f_0(980)$ and $a_0(980)$

As mentioned previously, four quark states are believed to fall apart into two colour singlets. However, an exception to this rule was found by Weinstein and Isgur for scalars corresponding to the $qs\overline{qs}$ system [14]. The ground state of this four quark system was found to consist of weakly-bound states of kaon and antikaon. Weinstein and Isgur referred to these states as $K\overline{K}$ molecules. The scalars $f_0(980)$ and $a_0(980)$ were considered candidates for these states, since their masses were just below the $K\overline{K}$ threshold and they had strong couplings to strange final states. The $\gamma\gamma$ couplings of the two were subsequently found to be less than the expected values for light $^3P_0$ $q\overline{q}$ states [15]. The status of the $K\overline{K}$ molecule assignment has recently been discussed by Weinstein and Isgur [16],[17] where the points in favour of a $K\overline{K}$ assignment are mentioned.

Further results from radiative decays and $\gamma\gamma$ partial widths are required in order to provide further information about the nature of these two states.

1.6.2 The $f_J(1710)$

This was considered in early references as a candidate for being a glueball since it was discovered in radiative ψ decay [18] and has no obvious assignment in the $q\overline{q}$ spectrum. It was observed in the WA76 central production experiment at 300 GeV in both K^+K^- and K^0K^0 decay modes [19]. This spin of this state is currently under dispute with the WA76 experiment favouring a $J^{PC} = 2^{++}$ assignment. Another experiment [20] also favours this assignment from partial wave analysis of the K^0K^0 mass spectrum. The MARK III collaboration (which had previously produced results that supported a 2^{++} assignment) have produced results indicating that the $f_J(1710)$ is a $J^{PC} = 0^{++}$ object [21]. It must be noted that the available statistics for this resonance put some limit on current analysis. The $f_J(1710)$ has recently been suggested as being a $K^*\overline{K^*}$ molecule candidate, the system being bound by one pion exchange [22],[13]. Further experimental data are required in order to better define this resonance and to understand its nature.

1.6.3 The $f_0(1520)$

A recent Crystal Barrel study [23] of the proton annihilation reactions $p\overline{p} \to \pi^0\pi^0\pi^0$ and $p\overline{p} \to \eta\eta\pi^0$ finds two broad $J^{PC} = 0^{++}$ states, the $f_0(1365)$ with mass 1365^{+20}_{-55} MeV and width $\Gamma = 268 \pm 70$ MeV and the $f_0(1520)$, with a mass 1520 ± 25 and width $\Gamma = 148^{+20}_{-25}$ MeV. The $f_0(1365)$ is believed to be consistent with a $^3P_0$ $q\overline{q}$ state, which would be made up of $u\overline{u} + d\overline{d}$. The $f_0(1520)$ mass means that if it were a $q\overline{q}$ state it would have to be made up of $s\overline{s}$, but it has been observed in channels such as $\eta\eta$ and $\pi\pi$ [23]. The mass of the $f_0(1520)$ is consistent with predictions for the mass of the 0^{++} glueball, and its coupling to flavour singlet final states is also consistent with this interpretation. Further study of its decays is needed in order to enable any detailed interpretations of its structure.

1.6.4 The $G/f_0(1590)$

The GAMS collaboration was the first experiment to observe the $G/f_0(1590)$, having found it in π^-p charge exchange reaction [24],[25]. This state has $J^{PC} = 0^{++}$ and has been observed to decay to $\eta\eta$ and $\eta\eta'$. In particular, the GAMS collaboration have reported a large branching ratio to $\eta\eta'$ [26]. This is important since a large $\eta\eta'$ decay mode could be a signal of glueball decay [27]. The statistics for the $\eta\eta'$ are poor, and so higher statistics are required to validate this branching ratio. An object compatible with being the $G/f_0(1590)$ has also recently been observed by the Crystal Barrel collaboration in the $p\overline{p} \to \eta\eta\pi^0$ reaction [28]. The observation in this annihilation reaction, where gluonic states are believed to be produced, serves to give further evidence for a possible gluonic nature.

1.6.5 The X(1450) and X(1900)

The WA76 collaboration, the central production experiment that preceeded WA91, reported the observation of two previously unobserved mesons, which it called the X(1450) and X(1900), decaying to the central $\pi^+\pi^-\pi^+\pi^-$ system in the reaction $pp \to p(\pi^+\pi^-\pi^+\pi^-)p$ at 300 GeV/c [29]. The X(1450) has not been observed in any other production mechanism although this mass region has been studied thoroughly. One of the main aims of the WA91 experiment was to confirm the existence of these states and to determine their quantum numbers. The WA91 experiment at 450 GeV/c [30] did indeed confirm the earlier data. The X(1450) was found to have mass and width M = 1446 ± 5 MeV, $\Gamma = 56 \pm 12$ MeV and quantum numbers $J^{PC} = 0^{++}$, whilst the X(1900) has mass and width M = 1926 ± 12 MeV, $\Gamma = 56 \pm 12$ MeV and quantum numbers $J^{PC} = 2^{++}$. The analysis also concluded that the X(1900) may be made up of two $J^{PC} = 2^{++}$ states. The X(1450) is of particular interest since it has only been produced in central production , and it does not fit into the conventional ground state $q\overline{q}$ nonet. The WA91 collaboration has recently taken further data at 450 GeV/c, and this should enable further study of these two mesons.

It is clear from the results presented that several states exist as potential candidates for being non-$q\overline{q}$ mesons. These states have been found in many different reaction mechanisms. In the cases referred to above, evidence for the non-$q\overline{q}$ nature is being produced, but further statistics and study are required to produce overwhelming evidence.

One difficulty encountered in meson spectroscopy is that different experiments tend to be sensitive to particular channels because of their different experimental layouts. By comparing data for the same channels for different experiments, further important information about states may be gained. As an example of how this problem is being solved, the WA91 experiment, which has good charged track measurement, is being combined with the GAMS collaboration which has good neutral particle identification, in experiment WA102 at CERN. This combination will enable channels such as centrally produced $\eta\eta$ to be investigated in greater depth, for example. Through continued effort to improve experimental techniques, a greater understanding of non-$q\overline{q}$ candidates will be developed.

Chapter 2

WA91 Experimental Details

2.1 Introduction

The WA91 experiment [31] is designed to study exclusive final states formed in the reaction

$$pp \rightarrow p_f (X^0)\ p_s$$

where the subscripts f and s indicate the fastest and slowest particles in the laboratory frame respectively and X^0 represents the central system that is believed to be produced by a double exchange process. At high centre-of-mass energies these double exchange processes are thought to be dominated by Double Pomeron Exchange (DPE), where the Pomeron is thought to have a large gluonic content [32], leading to the conclusion that Pomeron-Pomeron scattering could be a source of gluonic states [33] : DPE is also thought to be enhanced when the four-momentum transferred (t) at the exchange vertices is near zero [34]. The reaction required, in the centre-of-mass frame, is represented pictorially in figure 2.1. Since Pomeron exchange at each vertex is favoured by small momentum transfer, this implies that the fast and slow final state particles will be very fast and very slow i.e. they will have values of Feynman x (x_F) near $+1$ and -1 respectively. The centrally produced system should be well separated in x_F from the fast and slow particles. An example of the x_F distribution required is shown in figure 2.2 which shows x_F for the final state particles in the centrally produced $\eta\pi^+\pi^-$ channel for the WA91 experiment at 450 GeV/c.

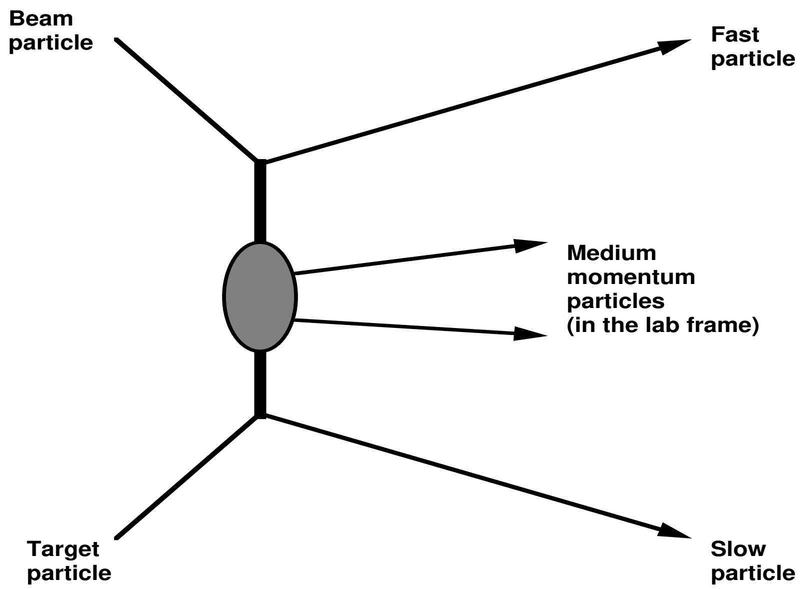

Figure 2.1: Central production as viewed from the centre of mass. This is the kind of reaction selected by WA91.

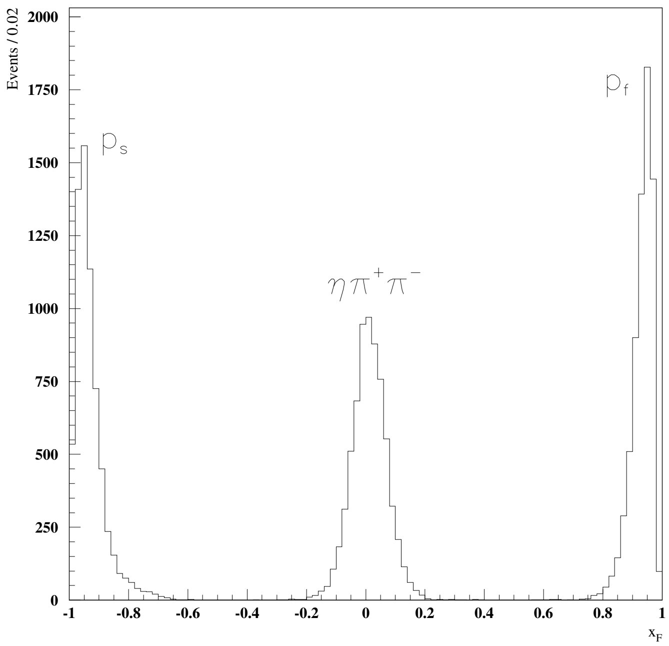

Figure 2.2: The x_F distribution for the final state particles in the centrally produced $\eta\pi^+\pi^-$ channel at 450 GeV/c.

Since the Pomeron is believed to be a multigluonic object, then this implies that it will have quantum numbers 0 for strangeness and other flavours. Because of this, the final fast and slow particles must also be protons. The trigger necessary for obtaining central production events of the kind outlined above thus relies upon measuring a well separated slow and fast proton for a particular event, and the means of doing this will be discussed subsequently.

2.2 WA91 Experimental Layout

The layout of the Omega spectrometer used for the period of data taking during the Autumn of 1992 is shown in figure 2.3. The spectrometer is a multi-user detector designed for measuring fixed-target interactions that produce many final-state particles. It consists of a pair of superconducting Helmholtz coils that are capable of producing a central field of up to 1.8T. For the WA91 experiment the field used was 1.35T.

The WA91 experiment follows on from the original WA76 experiment which took data in 1982 using a π^+/p beam of 85 GeV/c, and a further run in 1986, using a 300 GeV/c proton beam. A summary of the results of this experiment is given in [31].

Many of the principal results of the WA76 experiment involved strange charged channels, such as the K^+K^- and $K_S^0K^\pm\pi^\mp$. These mass spectra are of considerable interest in meson spectroscopy. However, the statistics for neutral channels were low, since the GENEVA Photon Detector used as a calorimeter in WA76 was placed a long way from the target, and had a low acceptance. The WA91 experiment has been set up to look predominantly at neutral channels, using a different electromagnetic calorimeter, OLGA (Omega Lead Glass Array) to detect photons. Its position is nearer to the target to give an improved acceptance for neutral particle decays such as $\pi^0 \to \gamma\gamma$ and $\eta \to \gamma\gamma$. WA91 uses a higher momentum incident proton beam of 450 GeV/c and there have been several changes from the original WA76 layout in order to increase particle acceptances and track measurement.

The various components of the Omega spectrometer used in the 1992 setup are described below.

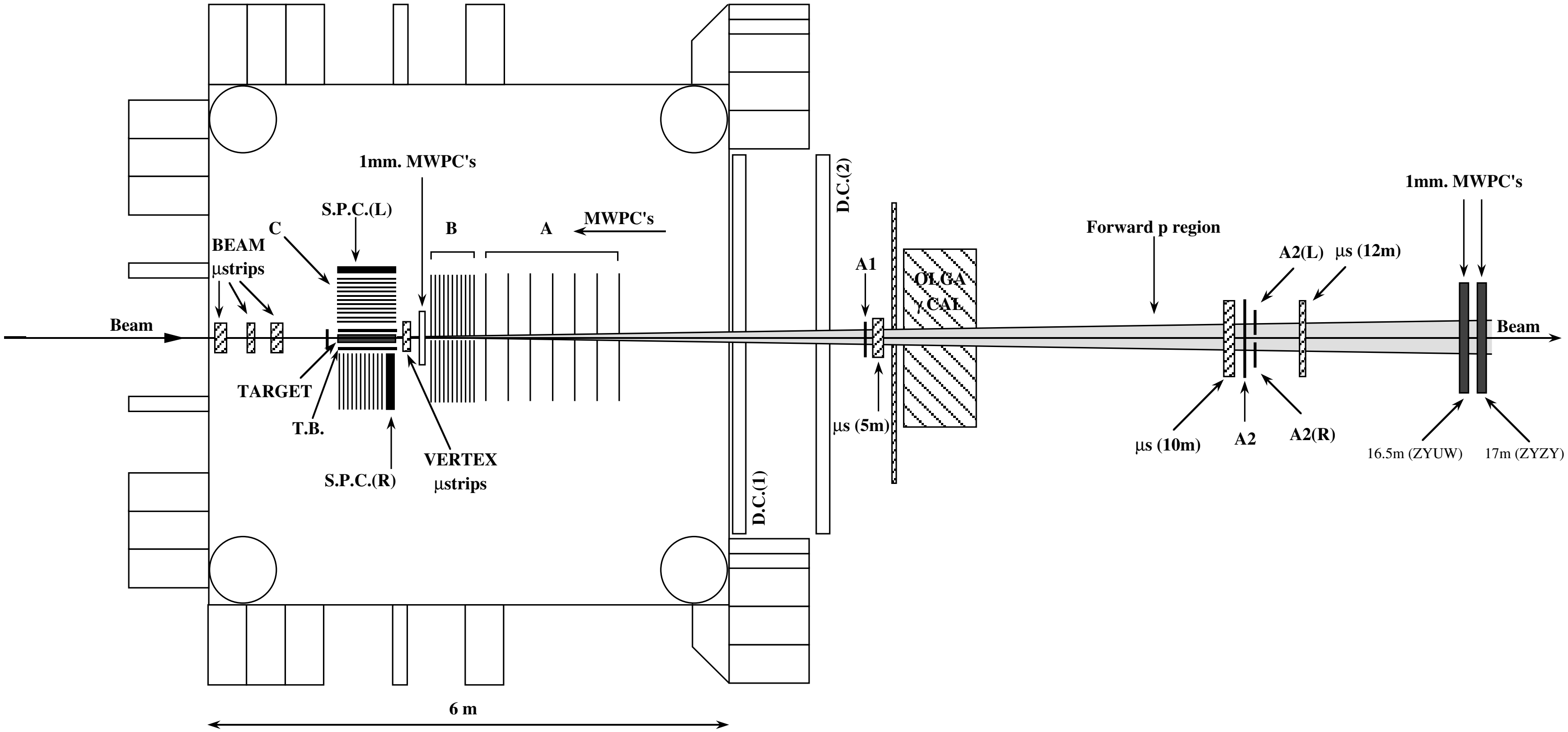

Figure 2.3: Layout of the WA91 experiment.

2.2.1 The Target

The target consists of a 60 cm long cylinder of liquid hydrogen in a mylar and aluminium container. This length of hydrogen constitutes 15% of an interaction length.

2.2.2 The Target Box (TB)

The target box consists of 10 slabs of scintillator which surrounds the target on four sides but which is left open at the upstream and downstream ends of the target to allow beam in and forward particles out. The slabs have a layout and numbering system as shown in figure 2.4. Each slab is 60 cm long. Slabs 3-10 are 1 cm thick, whilst slabs 1 and 2 are 0.5 cm thick. The upstream end of the target box is at -102.2 cm in the Omega coordinate system (where zero is at the centre of the magnet). The main purpose of the TB was to reject events from target diffraction, as part of the WA91 trigger. This will be discussed in greater depth in the section on trigger elements.

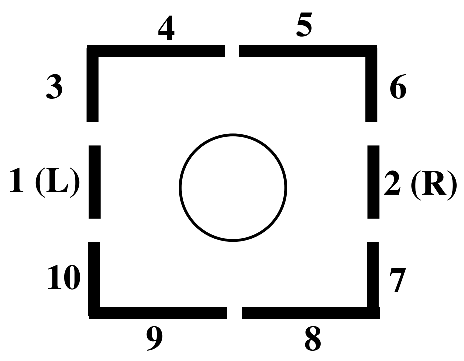

Figure 2.4: Layout of the scintillator slabs of the Target Box (TB), looking downstream.

2.2.3 Multi-Wire Proportional Chambers

A proportional counter basically consists of a container of gas subjected to an electric field. A charged particle traversing this gas can produce a trail of ions and electrons in the gas. These are collected at the chamber electrodes and thus provide an electrical signal indicating the passage of the charged particle. Proportional chambers act as proportional counters when the applied field is large enough to cause the accelerated electrons to produce secondary ionisation, yet small enough so that the output pulse is still proportional to the number of primary ion pairs. The Multi-Wire Proportional Chamber (MWPC) consists essentially of a plane of anode wires between two cathode plates, surrounded by a gaseous mixture, usually isobutane and alcohol [35]. In this way, each of the anode wires acts as an individual proportional chamber.

There are several sets of MWPC's employed in the WA91 experiment for tracking of final state particles.

The A and B chambers are located downstream of the target, whilst the C chambers are mounted on either side of the target. The A chambers consist of 7 modules, each consisting of 3 planes of wires (UYV) where the Y planes are vertical in the Omega system, and the U and V planes are inclined at $\pm 10.14^{o}$ to the vertical. The B and C chambers consist of 8 modules, each module consisting of 2 planes (Y, U or V). The wire spacing in the A, B and C chambers is 2 mm and the gas surrounding the wires is a mixture of isobutane and alcohol.

The central production process as viewed from the lab frame has a distribution of final state particles shown typically in fig 2.5. For an incident beam momentum of 450 GeV/c, the different final state particles have the following approximate momentum ranges:

$$\begin{array}{rrcll} \text{fast track} & 350 & - & 450 & \text{GeV/c} \\ \text{medium track} & 1 & - & 30 & \text{GeV/c} \\ \text{slow track} & 0.1 & - & 1.5 & \text{GeV/c} \end{array}$$

The positions of the A, B and C chambers were optimised in order to detect efficiently the reaction products as depicted in figure 2.3; the C chambers are responsible for detecting the slow proton, whilst the A and B chambers are used to detect particles coming from the decay of the centrally produced system.

In addition to these chambers, there are also three MWPC's of wire spacing 1mm. The first of these is just downstream of the target, immediately behind the VERTEX microstrip detector and just in front of the B chambers. It has four planes of wires (YZUV) and is used to give extra points for the reconstruction of

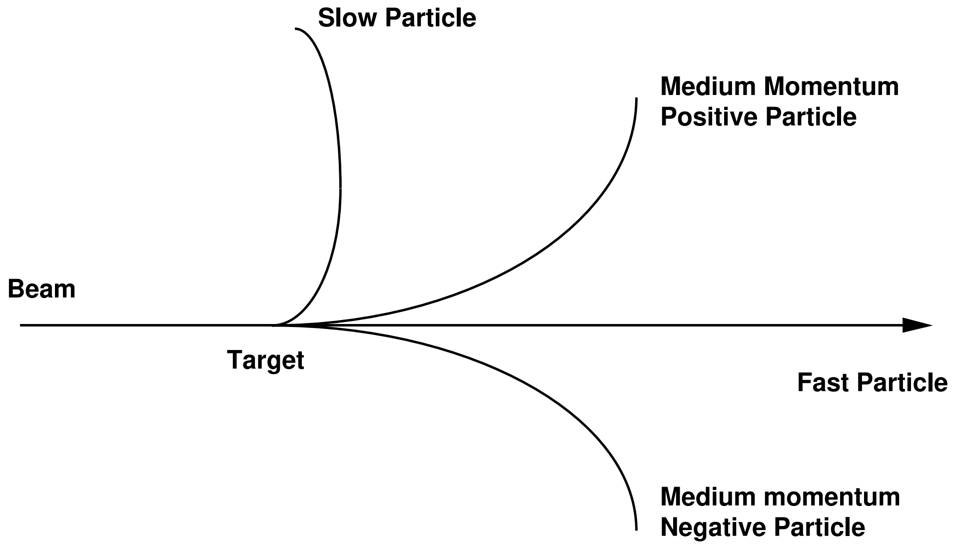

Figure 2.5: Central production as viewed from the lab frame.

tracks coming from the decay of the central system. The other two MWPC's, each of which also have 4 planes of wires (ZYUV and ZYZY) are placed at 16.5m and 17m downstream of the Omega centre. These are used to give extra points for the reconstruction of the fast track.

2.2.4 The Slow Proton Counters (SPC's)

There are two sets of SPC detectors, one on either side of the target, the left and right SPC's (left and right are relative to the direction of the incoming beam).These detectors were placed immediately behind each of the two sets of C chambers. Each SPC consists of 14 slabs of scintillator material supported vertically in an aluminium frame. SPC(R) has a slab width of 7 cm, whilst SPC(L) has a width of 6 cm. The active length of the slabs is 70 cm. They are used in conjunction with the C Chambers for identification of the slow proton. This will be discussed in greater detail in the sections on the C Chambers and the Slow Proton system.

2.2.5 The Drift Chambers

Downstream of the A chambers and outside of the magnetic field are two Drift Chambers, DC1 and DC2, at x positions in the Omega system of 327 cm and 441 cm respectively. Each module consists of 4 planes (YUYV), with each plane having a 2.5 cm spacing between the sense and field wires. These chambers are used in conjunction with the A and B chambers to reconstruct the medium momentum tracks.

2.2.6 Microstrip Detectors

Silicon microstrip detectors are devices that are employed to obtain accurately the coordinates at which a track passed through them. They basically consist of thin strips of silicon having a very small pitch (50μm or smaller), which are held at some biasing voltage, typically around 50V. Because of this, the strips are depleted of charge carriers. In this way, when an ionising particle passes through the silicon, its ionisation leaves a cluster of charge in a small region of a strip, which is then detected and amplified. This gives rise to an accurately determined space position, since the electronics reads out each of the strips or 'channels' separately. Because of their spatial accuracy, they are employed in the WA91 experiment for two purposes:

- Beam reconstruction. There are 5 modules used to define the trajectory of the beam particle. Two planes are housed within each module. All the modules are fixed to a rigid optical bench, which serves as a coordinate reference for the planes. The modules are separated along the length of the optical bench in groups. These separate groupings are labelled BEAM1, BEAM2 and BEAM3. The planes and the positions they define are tabulated in table 2.1.

- Fast track reconstruction. This is done by four sets of microstrips, placed at various distances along the beam direction downstream of the target. They are the VERTEX microstrips, and the 5m, 10m and 12m microstrips (see fig 2.3 for positions relative to other apparatus). The planes they define are tabulated in table 2.1. The VERTEX detector also serves to provide space points for the reconstruction of the medium momentum tracks that pass through the A and B chambers, thus giving improved efficiency for finding V^0's. These

Name	Planes	Pitch	Channels	Dimensions (mm)	X position (mm)
BEAM1	4 (ZYZY)	20μm	512	10.24$\times$10.24	-3998/-3988/-3942/-3931
BEAM2	2 (ZY)	20μm	512	10.24$\times$10.24	-3326/-3315
BEAM3	4 (ZYYZ)	20μm	512	10.24$\times$10.24	-2729/-2718/-2686/-2676
VERTEX	4 (ZYYZ)	25μm	2048	51.2$\times$51.2	-969/-944/-919/-894
5m A1	4 (ZYZY)	25μm	2048	51.2$\times$51.2	5330/5335/5380/5405
10m A2	4 (ZYZY)	25μm	2048	51.2$\times$51.2	10462/10487/10512/10537
12m A2	2 (YY)	50μm	2048	51.2$\times$51.2	12501/12553

Table 2.1: Positions of the microstrips used in the 1992 run.

microstrips also help to track any beam particles which did not interact in the target and carried on through the chambers (the so-called BEAM triggers).

2.2.7 The OLGA Electromagnetic Calorimeter

The OLGA calorimeter is used in order to detect photons coming from the decay of particles that were produced in the central system. As such, OLGA can be used for the investigation of neutral channels eg. $\pi^0\pi^0$, or channels with a neutral component eg. $\pi^+\pi^-\pi^0$ where these neutrals can be reconstructed from the photons detected by the calorimeter. OLGA consists of three modules:

- An array of 18$\times$19 lead glass blocks, each with a surface 14$\times$14cm^2 and a depth of 47 cm, corresponding to 18.5 radiation lengths. The central block was removed for the 1992 run, leaving a hole of side 14 cm about the centre of OLGA to allow the passage of the beam and fast track unimpeded.

- Samplers, which are large lead glass slabs (14$\times$145 cm^2) of depth 10 cm, which corresponds to three radiation lengths. These are arranged in a column of 19 samplers down the left and right halves of the front of OLGA. A photon incident on the sampler will start an electromagnetic shower within it.

- The positional detector made up of scintillator fingers arranged in four half planes. There are two horizontal half planes made up of 180 fingers (length 147 cm, width 1.53 cm, depth 1 cm) and two half planes of vertical fingers, each made up of 180 fingers (length 152cm, width 1.53 cm, depth 1 cm). Signals in the fingers, induced by the shower started in the sampler enables the incident particle position to be accurately established.

OLGA was positioned so that the front face of the samplers was just over 6 m downstream of the Omega centre. In this position in Omega, solid angle and resolution are optimized.

2.3 The WA91 Trigger

2.3.1 Trigger Elements

The aim of the WA91 experiment is to study reactions of the type depicted in figure 2.1. As has been mentioned previously, the important features of a central production reaction of the kind WA91 requires is that one positively charged fast track and one positively charged slow track is produced from the reaction, and that there are other particles generated by the reaction, which are picked up by the forward chambers and/or OLGA. In the light of this, the following trigger elements are required.

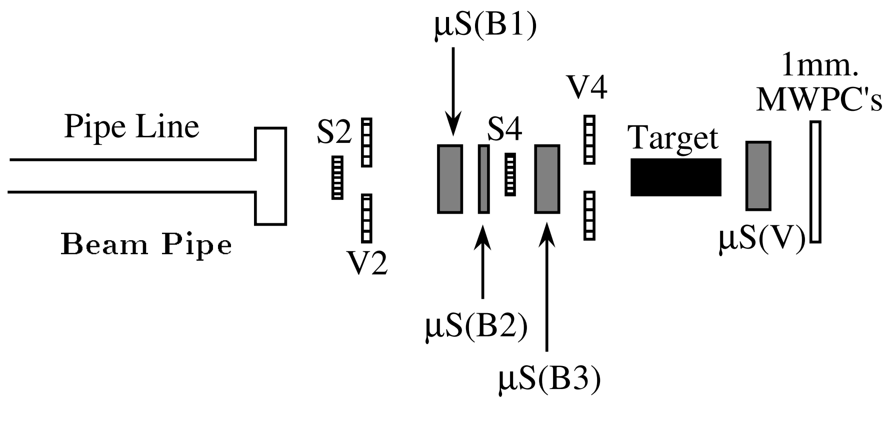

Figure 2.6: Detector Layout in the target region of the WA91 experiment.

- A Clean Beam(CB) signal. The relative positions of the detectors that are used to define CB are shown in figure 2.6. There are four different scintillators that are used to for CB definition, namely S2, S4, V2 and V4. S2 and S4 are square scintillators of side 2.5 cm and 0.8 cm respectively., and both are 5 mm thick. V2 and V4 are also square scintillators, of side 17 cm, and both have holes in the centre of them, of diameter 1.5 cm and 0.8 cm respectively. Both V2 and V4 are 10 mm thick. The requirement for BEAM is that S2 and S4 both have signals, whilst V2 and V4 do not, implying that the beam hits S2 and S4 whilst passing through the holes in V2 and V4. CB requires BEAM, and checks that only one beam particle passes through S2 in a time period of 50 ns. The means by which this is achieved is described below. Figure 2.7 shows the logic that is used to define clean beam. The CB coincidence requires

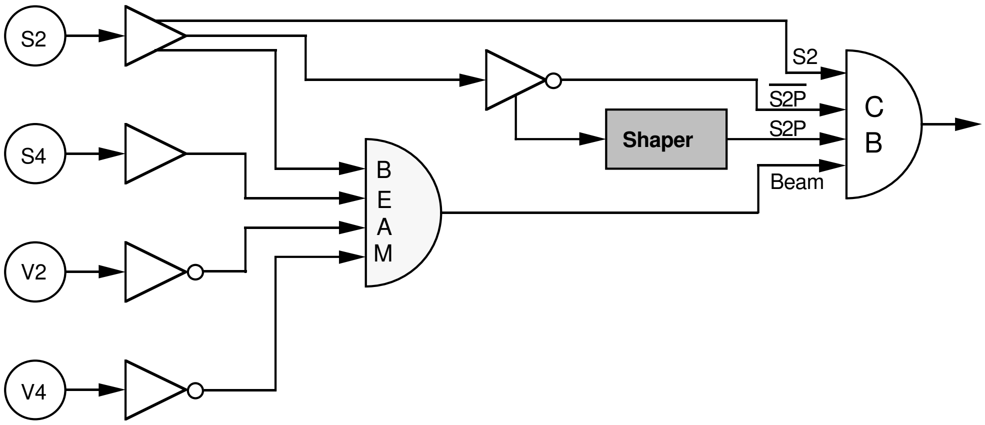

Figure 2.7: Beam logic used to define Clean Beam (CB).

a BEAM signal and also S2, S2P and the inverse of S2P. If a signal arrives at S2, then the signals from the logic are timed to arrive as shown by the solid lines in figure 2.8. Because of the way the inverted signal from S2P is timed, the CB coincidence will be satisfied. If, however, a second particle arrives at S2, a time Δt after the initial particle as shown by the dashed line, then it means that the inverted S2P signal will have a greater duration, preventing the CB coincidence from producing an output, and thus rejecting the event. For a pulse with a width for $\overline{\text{S2P}}$ of T, then this will block particles for a time T after the incident particle on S2.

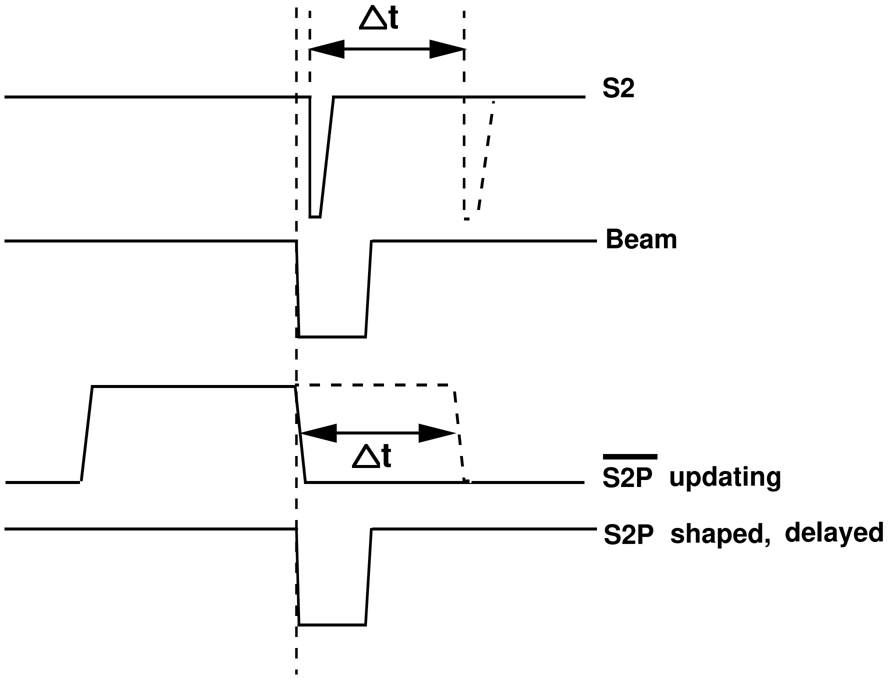

Figure 2.8: Timing of signals to the CB coincidence.

- A fast particle trigger. Triggering on the fast particle is done by demanding a coincidence between two scintillation counters, A1 and A2, placed close to the downstream microstrips (see figure 2.3). These are square slabs of side 2.5 cm and 5 cm respectively. A1 is placed 485.1 cm downstream of the Omega centre, whilst A2 is at 1077.9 cm.

- A slow particle trigger. The slow proton trigger comprises two parts; for a left slow proton trigger, for example, the BOX slab TB1(L) must fire, (see figure 2.4 for the BOX layout) and a coincidence is demanded between this and either one or two of the slabs of SPC(L). Conversely, for a right slow proton trigger, then a coincidence is required between TB2(R) and one of the slabs of SPC(R). There is a reaction that competes with central production, that of target diffraction, as depicted in figure 2.9 which produces several slow particles in the laboratory frame and the trigger is set up to exclude these events in the following manner. It is demanded that no other slabs in the target box fire, only TB1(L) or TB2(R).

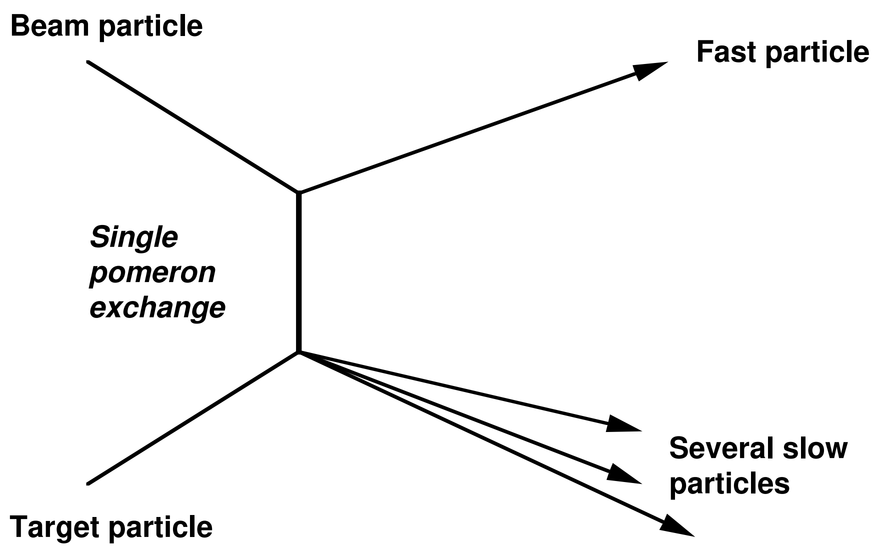

Figure 2.9: The process of target diffraction, a reaction that competes with central production in pp reactions.

Since the SPC requirement is that 2 or less slabs fired, then this also serves to reduce target diffraction, eliminating events where several slow momentum tracks may have gone through only one of the BOX slabs. The trigger coincidence that decides if these conditions have been fulfilled takes place 68 ns after an S2 signal has been received. Selection of the slow proton is mentioned more fully in the slow proton section.

- Neutral particle trigger. OLGA was used to trigger on neutral particles. Photons from a neutral decay will lead to an energy deposition in one or more blocks of the OLGA array. A neutral trigger was defined by having signals from at least one block of OLGA, and a minimum energy deposition of 2 GeV.

2.4 The Slow Proton System

The slow proton system forms an integral part of the WA91 setup, since the slow proton is one of the necessary requirements to select central production events. The layout of the detection system is shown in figure 2.10. There are two sets of slow proton detectors, one on each side of the target, to the left and the right of the target relative to the beam trajectory.

Each slow proton detector consists of three elements. The first of these are the target box elements, TB1(L) and TB2(R), each 0.5 cm thick and 60 cm long. Immediately behind each of these are the C chamber MWPC's which consist of 16 planes of wires. Finally, there are 14 slabs of the Slow Proton Counter (SPC). The SPC's for both the left and right, SPC(L) and SPC(R) are basically the same, both having an active length of 70 cm and thickness 2 cm The slab widths of the two are marginally different; SPC(L) has a slab width of 6 cm whereas SPC(R) has a width of 7 cm. Subsequent sections will describe how signals from these elements were combined to discriminate between slow protons and pions in the slow proton detection system, for particles in the momentum range 0.1-1.5 GeV.

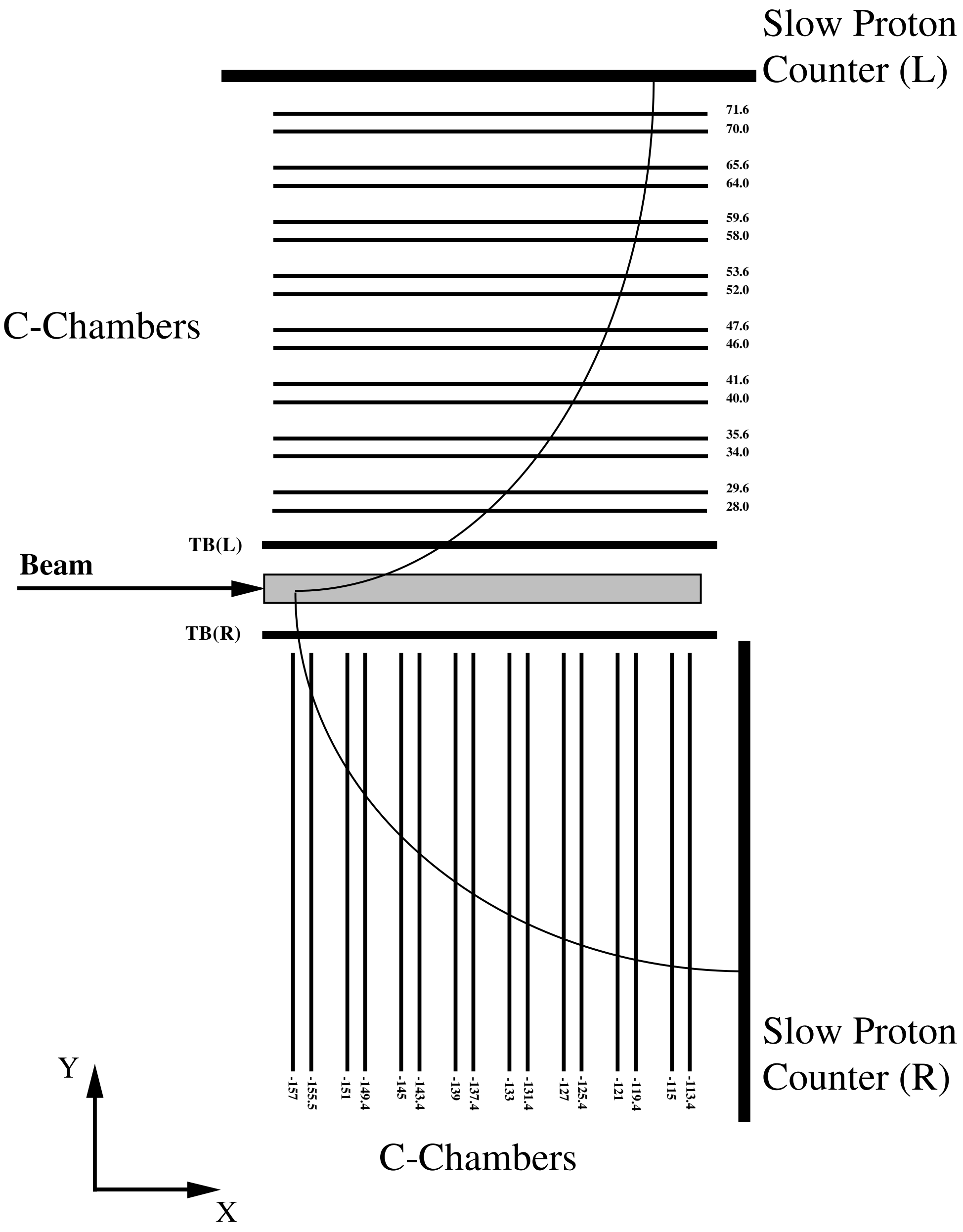

Figure 2.10: Layout of the WA91 slow proton detection system.

2.5 The C Chambers

The C chambers are used in WA91 to reconstruct the path of particles passing through them, in order to establish their momentum. For each of the left and right sets of 16 planes there are 8 Y planes which are vertical in the Omega system, and 4 each of the U and V planes which are inclined at $\pm 10.14^{\circ}$ to the vertical. The sixteen planes are grouped into 8 modules, each module having a Y plane and either a U or a V plane. An exploded view of two C chamber modules is shown in figure 2.11. Each of the planes contains 256 wires of pitch 2 mm.

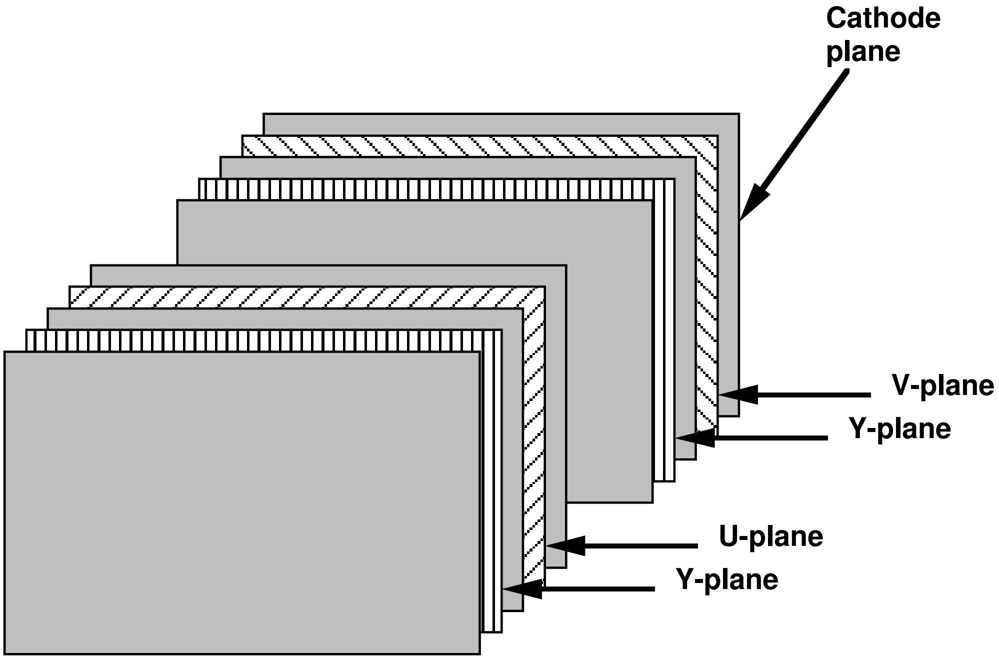

Figure 2.11: Exploded view of two C Chamber modules.

The alignment of the planes of both sets of C chambers is shown in fig. 2.10. Because of the direction of the magnetic field, the path of low momentum positively charged particles on both sides of the the target will be as indicated by the curved lines in figure 2.10. This necessitates placing the C chamber planes of the right hand system at right angles to the planes of the left system, in order to obtain a better acceptance for particles on the right.

In the 1992 run, the C chambers were used to select slow protons by requiring hits on certain planes. For the left set of chambers, C5 and C7 were required to have 1 or 2 wires firing per plane to ensure that the track was a clean one. C5 and C7 were chosen since they were planes in the centre of the detector, and both planes had good efficiency (the numbering system for the left hand C chamber starts with C1 closest to the target). The condition for the right hand system was similar, requiring that 1 or 2 wires fired in C7 and C9 (where C1 is the most upstream plane). These planes were chosen to be the most downstream planes of the right hand system, since this choice maximised acceptance for positive particles.

By using this selection process, the C chambers were used to reconstruct particle tracks, the Y chambers producing the x-y coordinates of the track and the U and V planes giving the z coordinates in the Omega system.

2.6 Momentum-Pulse height Correlation

The momentum of a track was found by using hits in the C chambers to reconstruct the curve of the particle, since it describes a helix. Following the helix fit, the curve is extrapolated to the plane of the SPC slabs. If a slab has fired at this extrapolated position, then the pulse height in the slab is used to produce a pulse height-momentum correlation. The correlation can be well-described by the Bethe-Bloch formula, which models the process of energy loss as a particle traverses a slowing medium.

2.6.1 Bethe-Bloch Energy Loss

When a particle of mass $M \gg m_e$, the mass of an electron, and charge Z_{inc} is incident at a speed βc through a slowing medium it dissipates energy principally through electromagnetic interactions with the electrons of the medium. The mean rate of energy loss per unit length is called the stopping power and is described by the Bethe-Bloch formula [36]:

$$\frac{dE}{dx} = \frac{D\ Z_{med}\ \rho_{med}\ (Z_{inc})^2\{ln(\frac{2m_e\gamma^2\beta^2c^2}{I}) - \beta^2\}}{A_{med}\beta^2}$$

$where$

$$D = 0.307\ MeV cm^2/g$$

$$I = 16(Z_{med})^{0.9}\ eV\ ; \quad \text{I characterises e}^- \text{ binding energy}$$
$$\rho = 1.16\ g/cm^3 \quad \text{for a plastic scintillator}$$

The scintillator material can be parameterized using:

$$A_{med} = 6.7$$
$$Z_{med} = 3.6$$

2.7 Pulse Height-momentum distributions

Figure 2.12 shows a typical pulse height *vs* momentum plot for one of the slabs of SPC(L). This shape is of the Bethe-Bloch form, the maximum of the distribution corresponding to a particle just being stopped by the scintillator material. The

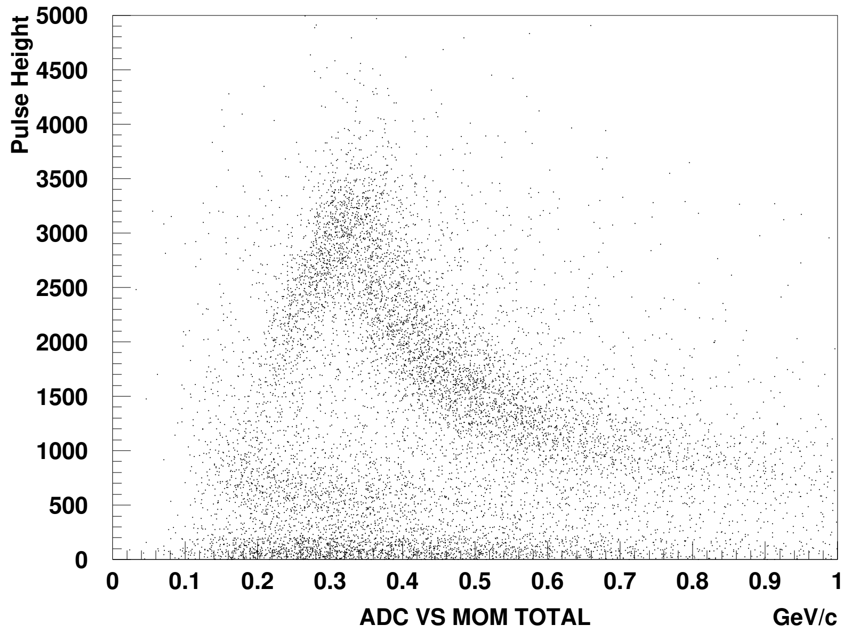

Figure 2.12: Pulse height-momentum correlation for the left slow proton system.

broad band making up most of the distribution is due to slow proton energy loss. The other, less dense region towards the bottom of the plot is due to the presence of slow pions. For a given momentum, protons will deposit greater energy in the scintillators than pions, giving rise to the observed difference in pulse height. This separation is used to eliminate slow pions from the WA91 trigger. Pulse height momentum correlations are produced for each slab of both SPC's and these are used to set the ADC discriminator thresholds to exclude the low signal pions.

2.7.1 Event Classification

In an experiment that seeks to pick out reactions of the type depicted in 2.1, any reactions will be dominated by elastic scattering. An elastic event may generate a slow proton, and the original beam particle will continue on its way without any central system being formed. An elastic event is categorised by having a fast and a slow particle travelling in opposite senses, i.e. one to the left and one to the right, and no medium momentum tracks.

In order to eliminate these events, trigger elements are combined to classify events into one of the following categories:

LL

RR

LR with OLGA

RL with OLGA

BEAM

LR with FASTRO

The first letter of the left (L) and right (R) assignments is determined by which of the slow proton conditions were met; the second R or L assignment depends on which of the two counters A2(L) or A2(R) fired. These two counters are positioned immediately behind A2 and they serve to establish the direction of the fast particle. The first five of the conditions listed above constitute the LEVEL 1 trigger, where this is the fast trigger part of an event (the LL, RR, LR, and RL assignments are made within 125 ns after the S2 signal, the extra OLGA decision is made within 190 ns).

From these assignments, elastic events can be rejected by only considering events with either a fast left particle with a slow left particle, (i.e. LL) or a fast right particle with a slow right particle (RR), since these cannot be elastic. Other allowed events are those where there is for example a slow left and a fast right particle, together with a signal from the OLGA calorimeter (LR with OLGA).

Subsequent to the LEVEL 1 trigger, there is the LEVEL 2 trigger. At this stage, multiplicities from the wire chambers are used in order to do further checks on an event. The LEVEL 2 trigger checks the multiplicity of planes of different chambers. It checks two specific planes in the C chambers and requires that only one or two wires must fire per plane, as mentioned in the slow proton section.

The FASTRO (FAST Read Out) trigger is used in LEVEL 2 to pick out events not taken by the OLGA triggers or the LL or RR triggers, i.e. those events where the slow and fast particles go in different directions and there are no signals from OLGA, but there is a reasonable multiplicity in the A chambers. The FASTRO requirement is that there are two or more hits outside of the beam region in the Y plane of the A3 MWPC. This then picks up channels such as p$(\pi^+\pi^-)$p and p$(\pi^+\pi^-\pi^+\pi^-)$p where there is nothing that will produce γ's. If this trigger was not present, then these events would be rejected as elastic. The reason why FASTRO is fast is that the wires of the A3 chamber are read out in groups of 8 wires at a time, which is faster ($\approx 10\mu$s per chamber) than the normal rate reading each wire separately ($\approx 100\mu$s).

It is at the LEVEL 2 stage, after an event has been classified according to one of the above criteria, that the chamber information, and the information from the microstrips is read out and stored.

The beam flux from the CERN SPS used in the run was 5x10^6 protons per second, over a total burst time of 2.4 seconds. The cycle time was approximately 15 seconds. There were roughly 500 events taken per burst, and the total number of triggers taken during 43 days of data taking in the Autumn of 1992 was 84 million.

Chapter 3

A non-$q\overline{q}$ candidate : the $E/f_1(1420)$ meson

3.1 Introduction

The experimental search for gluonia has been carried out in the type of reactions that were discussed in chapter 1. In particular, several experimental programs have studied $p\overline{p}$ reactions and radiative J/ψ decays, and the WA76 experiment has carried out research based on selection of centrally produced channels. A great deal of effort in meson spectroscopy has focussed on the $K^0_S K^{\pm}\pi^{\mp}$ channel, which is accessible to all these types of experiment. The attention came because of the observation in the mass spectra of the various experiments of a resonance at a mass of around 1.4 GeV, named the E meson. Since this resonance was appearing in experiments where there is believed to be a large possibility of forming gluonia, then it seems natural that it should be thoroughly studied in order to determine its nature.

The E meson was first observed by Baillon et al [37] in 1967 in the annihilation reaction $p\overline{p} \rightarrow K^0_L K^{\pm}\pi^{\mp}\pi^+\pi^-$ at 400 MeV/c incident antiproton beam. Their assignment for the quantum numbers of the E were $I^G(J^{PC}) = 0^+(0^{-+})$. They also determined the mass of the E meson to be 1425 $\pm$ 7 MeV with a width of 80 $\pm$ 10 MeV. It was thought then to decay equally *via* $a_o(980)\pi$ and $\overline{K^*}K$ intermediate states.[1]

[1] All references to the K^* particle in this thesis refer to the $K^*(892)$.

Since this original analysis, several experiments have observed resonances in the 1.42 GeV region. This section presents a review of the current experimental data in the 1.42 GeV mass region, and also discusses the interpretations that have been made in an effort to explain the nature of the resonance which has become known as the $E/f_1(1420)$.

3.2 A history of the $E/f_1(1420)$: the E/ι puzzle

After the initial observation described above, the next observation of the E was made by Dionisi et al in 1980, [38] in the reaction $\pi^- p \rightarrow K^0_S K^\pm \pi^\mp n$ at 3.95 GeV/c. The $K^0_S K^\pm \pi^\mp$ mass spectrum they observed in the E mass region is shown in figure 3.1.

Figure 3.1: The $K^0_S K^\pm \pi^\mp$ mass distribution for the reaction $\pi^- p \rightarrow K^0_S K^\pm \pi^\mp n$ observed by Dionisi et al.

By fitting to the Dalitz plot in the E meson mass window defined by ($1.39 \leq$ M($K^0_S K^\pm \pi^\mp$) ≤ 1.47) they obtained the results

$$\begin{aligned} M &= 1426 \pm 6 \text{ MeV} \\ \Gamma &= 40 \pm 15 \text{ MeV} \end{aligned}$$

and $I^G(J^{PC}) = 0^+(1^{++})$. The E was found to decay predominantly *via* $K^*\overline{K}$ (86%), the rest *via* $a_0(980)$.

In addition to these observations, a resonance in the 1.4 GeV/c^2 mass region was observed by the MARK II collaboration [39] in radiative J/Ψ decay, namely the $J/\Psi \rightarrow \gamma K\overline{K}\pi$ reaction. They found a state of mass 1440^{+10}_{-15} MeV/c^2 and width 50^{+30}_{-20} MeV/c^2. A spin analysis of the Dalitz plot for $K^0_S K^\pm \pi^\mp$ events concluded that the state was $J^{PC} = 0^{-+}$, decaying predominently *via* $a_0(980)\pi$, with a possible small amount of $K^*\overline{K}$ decay.

The Crystal Ball collaboration [40] later confirmed this resonance by considering the $J/\Psi \rightarrow \gamma K^+K^-\pi^0$ reaction. Their partial wave analysis of the $K^+K^-\pi^0$ system produced the result $J^{PC} = 0^{-+}$, with the decay occuring *via* the $a_0(980)\pi$ intermediate step. Their $K^+K^-\pi^0$ mass spectrum is shown in figure 3.2.

Figure 3.2: The $K^+K^-\pi^0$ mass distribution for radiative decay $J/\Psi \rightarrow \gamma K^+K^-\pi^0$. The shaded region has the requirement $M_{K\overline{K}} < 1125$ MeV. (Crystal Ball data).

The resonance parameters they deduced were

$$M = 1440^{+20}_{-15} \text{ MeV}$$
$$\Gamma = 55^{+20}_{-30} \text{ MeV}.$$

They referred to this resonance as the $\iota(1440)$.

In 1984, the WA76 collaboration studied the central production reaction $(\pi^+/p)p \rightarrow (\pi^+/p)(K^0K^\pm\pi^\mp)p$ at 85 GeV/c [41]. In this channel, which is widely believed to be a gluon-rich one, they observed a prominent peak at around 1.4 GeV, as shown in figure 3.3.

Figure 3.3: The mass distribution for the centrally produced $K_L^0K^\pm\pi^\mp$ system at 85 GeV/c (WA76 data).

Their spin analysis of the Dalitz plot produced from $K_L^0K^\pm\pi^\mp$ events concluded that the E was a $J^{PC} = 1^{++}$ object, having a mass and width of :

$$\begin{aligned} M &= 1425 \pm 2 \text{ MeV} \\ \Gamma &= 62 \pm 5 \text{ MeV}. \end{aligned}$$

In addition, their analysis found that the $E/f_1(1420)$ was being produced *via* the $K^*\overline{K}$ intermediate step, there being no evidence for the $a_o(980)\pi$ decay mode. This absence of a $a_o(980)\pi$ mode was in agreement with the lack of observation of the E meson in the centrally produced $\eta\pi\pi$ channel in the same experiment [42]. An object at the E mass was also found by the KEK experiment [43] in the reaction $\pi^-p \rightarrow \eta\pi^+\pi^-n$. The spin of this object was concluded to be 0^-, having a mass of 1420 ± 5 MeV and width $\Gamma = 31 \pm 7$ MeV, decaying *via* $a_o(980)\pi$.

Experimental results from BNL [44] caused further confusion in the assignment of the $E/f_1(1420)$ quantum numbers, where the reaction $\pi^-p \rightarrow K^+K_S\pi^-n$ was studied at 8.0 GeV. The $K^0K^+\pi^-$ mass spectrum observed in this reaction is shown in figure 3.4. The fit to the mass spectrum gave the mass of the $E/f_1(1420)$ as 1421

Figure 3.4: The $K^+K^0_S\pi^-$ mass distribution for the $\pi^-p \rightarrow K^+K^0_S\pi^-n$ BNL data at 8 GeV/c.

$\pm$ 2 MeV and a width of 60 $\pm$ 10 MeV. The Dalitz plot analysis carried out on this data concluded that the $E/f_1(1420)$ was predominently a 0^{-+} state (at least 70 %), with an $a_0(980)$ decay mode.

These apparently conflicting results from different experiments in the 1.4 GeV mass region became known as the E/ι puzzle.

Further studies of the $K^0_SK^{\pm}\pi^{\mp}$ mass spectrum were carried out in an effort to clarify the situation. Further experimental results from central production were obtained from the reaction $pp \rightarrow p(K^0K^{\pm}\pi^{\mp})p$, again from studies by the WA76 collaboration, except at a higher incident beam momentum of 300 GeV/c [45]. Their analysis confirmed the earlier results of the 85 GeV/c data, in that the E was found to be best represented by a $J^{PC} = 1^{++}$ object, having a mass and width of :

$$\begin{aligned} \mathrm{M} &= 1429 \pm 3 \text{ MeV} \\ \Gamma &= 58 \pm 8 \text{ MeV}. \end{aligned}$$

Again, no 0^{-+} wave was required to explain their data. Also, they found no evidence for the $\iota(1440)$ decay $\iota(1440) \rightarrow a_0(980)\pi$. The $K^0_SK^{\pm}\pi^{\mp}$ plot for the 300 GeV/c data is shown in figure 3.5.

Figure 3.5: The mass distribution for the centrally produced $K^0_S K^{\pm}\pi^{\mp}$ system at 300 GeV/c (WA76 data).

An analysis of the reaction $\pi^- p \rightarrow K^+ K^0_S \pi^- n$ at 8 GeV/c carried out at BNL, using a greater data sample than the previous publication of Chung et al was performed [49]. The mass of the resonance at 1.42 GeV was determined to be 1419 $\pm$ 1 MeV with a width of 66 $\pm$ 2 MeV. They found the 1.42 GeV mass region to have a complicated structure. There were found to be three waves contributing to the observed peak in the $K^+ K^0_S \pi^-$ mass spectrum, predominently (50%) the 0^{-+} wave, with contributions from 1^{++} and 1^{+-} waves.

An object compatible with being the E meson was observed by the TPC/2γ Collaboration [50]. in the reaction $e^+e^- \rightarrow e^+e^- R$, where the resonance R is formed by the exchange of two virtual photons. The $K^0_S K^{\pm}\pi^{\mp}$ invariant mass spectrum is shown in figure 3.6 where the signal has a mass of 1426^{+11}_{-7} MeV/c^2.

Tagged events (where one of the photons has a high Q^2) have an $E/f_1(1420)$ signal at the $E/f_1(1420)$ mass, whereas un-tagged events do not. This leads to the conclusion that the resonance is a spin 1 object, based on the result from Yang's theorem [8] that a spin one particle cannot be created from two real γs, but can be produced if one of the γ's has a high Q^2 and is off mass shell. Spin analysis indicated that

Figure 3.6: The $K^0_S K^\pm \pi^\mp$ mass distribution for a) un-tagged and b) tagged data for the $e^+e^- \to e^+e^- R$ reaction.

this state was consistent with being a 1^{++} state. This observation also produced a value for the $\Gamma_{\gamma\gamma^*} = 1.3 \pm 0.5 \pm 0.3$ keV.

This spin one result has been subsequently confirmed by the JADE collaboration [46] in the reaction $e^+e^- \to e^+e^- K^0_S K^\pm \pi^\mp$, where a signal at the E/f_1(1420) mass was observed only in tagged data. The $K^0_S K^\pm \pi^\mp$ plot they obtain for tagged data is shown in figure 3.7. They conclude that the E/f_1(1420) is a spin one object. They also obtained a $\gamma\gamma$ width of $\Gamma_{\gamma\gamma^*} = 2.3^{+1.0+0.8}_{-0.9-0.8}$ keV.

The CELLO collaboration have also carried out analysis of single tagged events from the $\gamma\gamma \to K^0_S K^\pm \pi^\mp$ reaction. They observe a peak having a mass of 1425 $\pm$ 10 MeV and a width of 42 $\pm$ 22 MeV. Their conclusion is that this object is a spin one object, having not been observed in un-tagged events. Their value of $\gamma\gamma$ width was determined to be $\Gamma_{\gamma\gamma^*} = 3.0 \pm 0.9 \pm 0.7$ keV.

3.3 A Solution to the E/ι puzzle

In 1990 the MARK III collaboration [52] investigated the $J/\Psi \to \gamma K^0_S K^\pm \pi^\mp$ reaction. The observed $K^0_S K^\pm \pi^\mp$ spectrum is shown in figure 3.8.

A partial-wave analysis of the $K^0_S K^\pm \pi^\mp$ system in the mass range 1.35-1.6 GeV/c^2 found that the data was best represented by three distinct sub-states :

Figure 3.7: The $K_S^0 K^\pm \pi^\mp$ mass distribution for the $e^+e^- \rightarrow e^+e^- K_S^0 K^\pm \pi^\mp$ reaction (tagged data).

Figure 3.8: The $K_S^0 K^\pm \pi^\mp$ mass spectrum for the reaction $J/\Psi \rightarrow \gamma K_S^0 K^\pm \pi^\mp$.

Amplitude	Decay mode	Mass (MeV/c^2)	Width (MeV/c^2)
1^{++}	K^*K	1443^{+7+3}_{-6-2}	68^{+29+8}_{-18-9}
0^{-+}	$a_0(980)\pi$	1416^{+8+7}_{-8-5}	54^{+37+13}_{-21-24}
0^{-+}	K^*K	1490^{+14+3}_{-8-16}	91^{+67+15}_{-31-38}

Table 3.1: masses and widths for the MARK III collaboration partial-wave analysis of the $K^0_S K^{\pm}\pi^{\mp}$ system.

- $\eta(1440)$ with $J^{PC} = 0^{-+}$ decaying *via* $a_0(980)\pi$,
- $\eta(1490)$ with $J^{PC} = 0^{-+}$ decaying *via* K^*K,
- $f_1(1420)$ with $J^{PC} = 1^{++}$ decaying *via* K^*K.

The fitted partial waves are shown in figure 3.9 for 1^{++}S K^*K, 0^{-+}P K^*K and 0^{-+}S $a_0(980)\pi$ waves, and the masses and widths obtained from the three fits are listed in table 3.1. The mass of the 1^{++} state is higher than the mass obtained from other experiments for the $E/f_1(1420)$, but is reasonably consistent.

Figure 3.9: The fitted partial waves in the $K^0_S K^{\pm}\pi^{\mp}$ system for the reaction $J/\Psi \rightarrow \gamma K^0_S K^{\pm}\pi^{\mp}$ for a) 1^{++}S K^*K wave b) 0^{-+}P K^*K wave and c) 0^{-+}S $a_0(980)\pi$ wave. Plot d) shows the summed 0^{-+} waves, and f) is a histogram of the data.

In central production, the 0^{-+} wave is suppressed relative to the 1^{++} wave. This can be demonstrated by considering the $\eta\pi\pi$ channel for central production, where there is a greater contribution from 1^{++} wave (in the form of the $f_1(1285)$) than there is for the 0^{-+} η' [53]. This is the opposite of what is observed in the case of the $J/\Psi \rightarrow \gamma\eta\pi\pi$ reaction where there is much more η' than $f_1(1285)$ (see, for example [54]).

So, it now appears that the E/ι problem stemed from the fact that different experiments picked out different resonances, but all in the same mass region, which was the cause of the initial confusion of quantum number assignment.

3.4 Current results

In 1992 the WA76 experiment performed a re-analysis of their combined 85 and 300 GeV data [61]. The $K^0_S K^{\pm}\pi^{\mp}$ mass distribution for the total data set is shown in figure 3.10.

Figure 3.10: The total $K^0_S K^{\pm}\pi^{\mp}$ mass spectrum data for the summed data from the WA76 central production experiment.

Their analysis of the Dalitz plot tested different wave hypotheses and found the K^*K 1^{++} wave again dominated the mass region of the $E/f_1(1420)$. This was in support of all the previous central production results.

To summarise the current state of knowledge in the 1400 to 1500 MeV range,

State	Reaction	Mass (MeV)	Width (MeV)	Decay *via*
$\eta(1440)$	Hadron production	1420 $\pm$ 20	60 $\pm$ 30	$a_0(980)\pi$
	$J/\Psi \to \gamma K\overline{K}\pi$	1416 $\pm$ 10	54^{+39}_{-32}	$a_0(980)\pi$
	$J/\Psi \to \gamma\eta\pi\pi$	1400 $\pm$ 6	45 $\pm$ 13	$a_0(980)\pi$
$E/f_1(1420)$	Central production	1430 $\pm$ 4	58 $\pm$ 10	K^*K
	$J/\Psi \to \gamma K\overline{K}\pi$	1443 $\pm$ 7	68^{+30}_{-20}	K^*K
$\eta(1490)$	$J/\Psi \to \gamma K\overline{K}\pi$	1490^{+14}_{-18}	91^{+69}_{-49}	K^*K

Table 3.2: Resonances in the 1400 to 1500 MeV range as determined from their $K\overline{K}\pi$ and $\eta\pi\pi$ decays, for the different reactions discussed in the text.

table 3.2 contains the average values for the masses and widths of such states, and also the different experimental production methods. The values for hadron production come from the PDG, and the central production values come from the WA76 experiment [45],[61]. The radiative J/Ψ decay values come from the MARK III experiment [52], [48].

3.5 Nonet assignment for the $E/f_1(1420)$

The $E/f_1(1420)$ has been observed in central production experiments, in $p\overline{p}$ annihilation, in two photon formation experiments and in J/Ψ decays. It is generally agreed that the $E/f_1(1420)$ decays almost exclusively to K^*K and has the quantum number assignment $J^{PC} = 1^{++}$. The $q\overline{q}$ model predicts that there should be a nonet containing two $^3P_1$ states with a mass below $\approx$ 1600 MeV. However, there are several problems encountered if one attempts to assign the $E/f_1(1420)$ state to the 1^{++} nonet, namely :

- Two states exist already that are good candidates for being the 1^{++} members of the $^3P_1$ nonet, the $f_1(1510)$ and the $f_1(1285)$. The $f_1(1510)$ in particular is a better candidate than the $E/f_1(1420)$ for the predominantly $s\overline{s}$ state in the nonet, having been observed in the reaction $K^-p \to (K^0_S K^\pm\pi^\mp)\Lambda$ [55] where it would be expected that $s\overline{s}$ states would be formed.

- The absence of any decay mode other than $K\overline{K}\pi$. Specifically, there has been no observation of the decay $E/f_1(1420) \to \gamma\phi$ [56]. Since the ϕ is an almost pure $s\bar{s}$ state, then $\gamma\phi$ decay would seem to be a good channel in which to find the $E/f_1(1420)$. Its non-observation again casts doubt upon the $E/f_1(1420)$ being the mostly $s\bar{s}$ member of the 1^{++} nonet.

- The two photon partial width for the $E/f_1(1420)$ has been determined to be ($\Gamma_{\gamma\gamma^*} = 1.3 \pm 0.5 \pm 0.3$ keV, larger than that predicted for the $^3P_1$ mainly $s\bar{s}$ state ($\Gamma_{\gamma\gamma^*} = 0.2$ keV [57]).

Since the evidence suggests that the $E/f_1(1420)$ is not a member of the 1^{++} nonet, then the natural conclusion is that it must have an exotic nature.

3.6 The nature of the $E/f_1(1420)$

Assigning the $E/f_1(1420)$ as a glueball candidate runs into problems, since the two photon width is larger than would be expected for a purely gluonic object (since gluons don't easily couple to photons). The interpretation from this is that the $E/f_1(1420)$ has considerable u and d quark content. Also, the 1^{++} state is not one of the allowed J^{PC} values for a glueball, as determined from bag model calculations.

There are two other non-$q\bar{q}$ interpretations for the $E/f_1(1420)$ that can been put forward: it could be a four quark state or a hybrid. Recent predictions for the latter of these two options indicate that the lowest mass hybrid state has a mass at around 1900 MeV, and this appears to make a hybrid assignation dificult.

Possible interpretations of the $E/f_1(1420)$ as a molecule have been made, and several models to represent this $K^*\overline{K}$ molecule put forth. For recent discussions on $K^*\overline{K}$ status see for example [16], [17] Longacre [58] envisages a π in a P-wave in orbit about an S-wave $K\overline{K}$ system. It is suggested that this state is bound by colour singlet particle exchange. An alternative picture is presented by Weinstein and Isgur [59] who present the idea that the $E/f_1(1420)$ is a $K^*\overline{K}$ molecule bound by colour forces.

3.7 Conclusions

The mass region between 1400-1500 MeV/c^2 is starting to be understood, after several years of apparently conflicting experimental results. There now appears to be at least two, and most likely three, states having masses around 1.42 GeV, the $E/f_1(1420)$ the $\eta(1440)$ and $\eta(1490)$

For the $E/f_1(1420)$, it is generally agreed that it decays predominently *via* $K^*\overline{K}$ and that it has quantum numbers $J^{PC} = 1^{++}$. It does not easily fit into the $^3P_1$ nonet, the one that would be considered the most likely, and experiments seem to indicate that it has a predominently light quark nature, not the mainly $s\overline{s}$ nature that would be needed for the $^3P_1$ nonet.

Clearly, the $E/f_1(1420)$ is a resonance of considerable interest, since it would appear to be of a non-$q\overline{q}$ nature. Further studies in order to better establish its properties would help to shed light on this matter.

Chapter 4

Development of V^0 recovery code for WA91

4.1 Introduction

When the WA91 event reconstruction program, TRIDENT, is implemented, the primary vertex is reconstructed by using the beam in conjunction with the slow proton track. The x coordinate is produced by intersecting the reconstructed beam track with the reconstructed slow proton. The beam track is then re-traced to this x position giving the y and z coordinates of the primary vertex. Tracks from the A and B chambers are also used to determine the vertex position. Subsequently, the fast track and any other tracks that appear to originate from vertices near the primary vertex are traced to it. However, this tagging of tracks has the effect that tracks coming from the decay of a V^0 near the primary vertex may be incorrectly assigned as coming from the primary vertex, and the V^0 will be lost. This effect is illustrated in figure 4.1, which shows the separation between the primary vertex and the V^0 vertex for V^0's found by TRIDENT. It can be seen that there are very few V^0 vertices at a distance of less than 20 cm from the primary vertex, the majority being found at distances greater than 40 cm. In order to rescue those V^0's that are lost in the region near the primary vertex, a V^0 recovery program was developed to be applied to events subsequent to the running of TRIDENT. This chapter describes how the V^0 recovery program works, the cuts used in its implementation, and how it was used in order to obtain K^0's for use in specific channels.

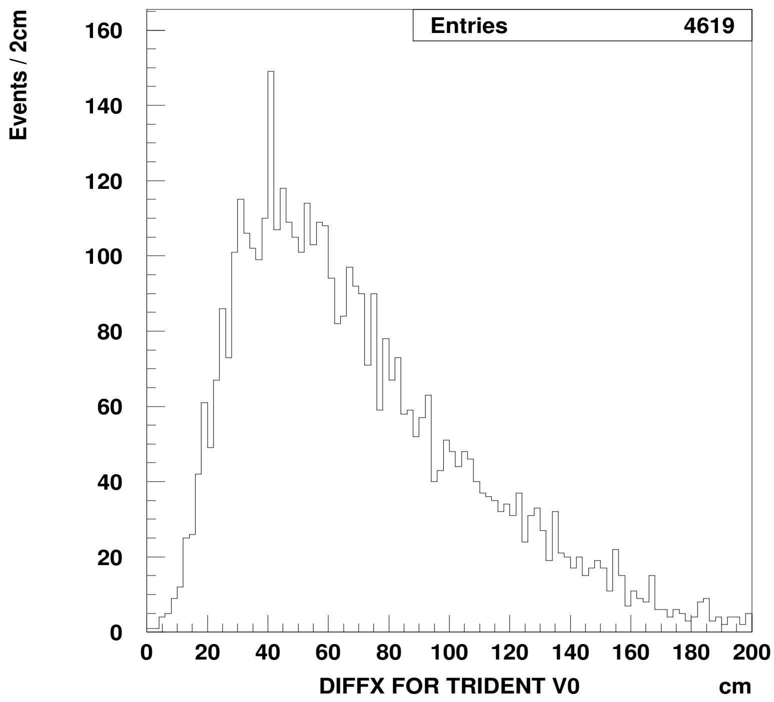

Figure 4.1: Separation of the V^0 vertex from the primary vertex for TRIDENT events.

4.2 Initial Selection of Good V^0's

The V^0 program considers all combinations of positive and negative tracks that have not been previously assigned as coming from a V^0 by TRIDENT, and loops over pairs assuming they constitute a V^0. In order to select a good V^0 candidate, certain criteria must be satisfied by the pair of tracks being considered. The first, obvious, criterion is that the two tracks comprising the V^0 must meet; that is to say they must have, at some coordinates, a distance of separation small enough for it to be likely that they originate from the same point. This distance of closest approach is referred to as *FARMAX* in the V^0 program (as shown in fig 4.2). For good V^0's the original requirement for pairs of tracks was:

$$FARMAX \quad < \quad 0.2 \text{ cm}.$$

For a good V^0 candidate this point of closest approach must be downstream of the primary vertex. Any vertices produced by the V^0 program upstream of the primary vertex are rejected. Further, in order to reduce a lot of spurious vertices, a minimum separation is required between the primary and secondary vertex, *DIFFX* (see fig 4.2). This cut is needed, due to the uncertainty in vertex position. The

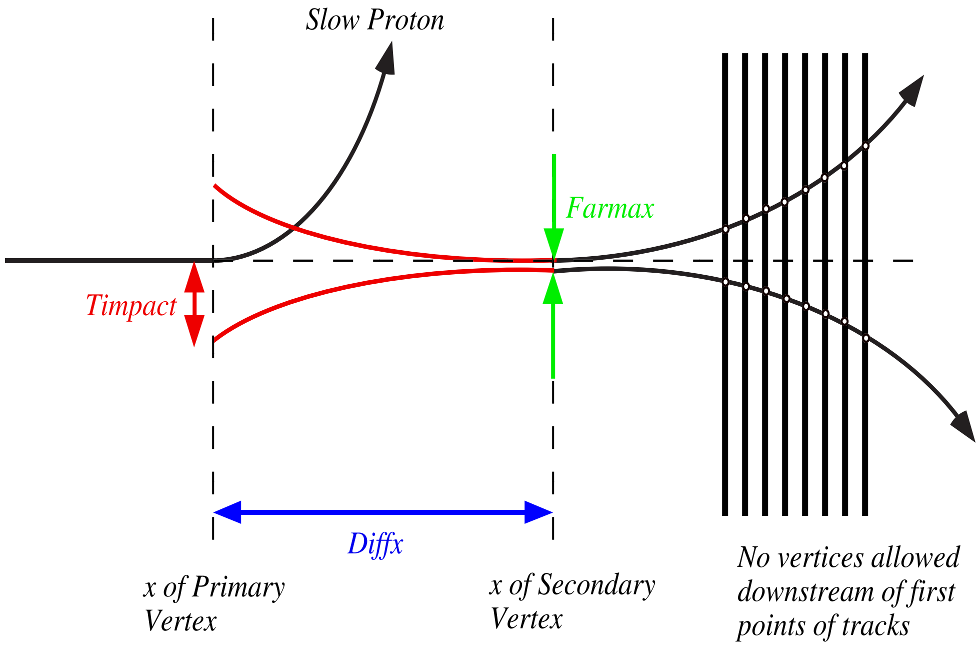

Figure 4.2: Cuts used in the selection of V^0's.

value chosen initially was

$$DIFFX \quad > \quad 2 \text{ cm}.$$

Another important means of selection of V^0's is to use the impact parameter at the primary vertex, $TIMPACT$ (fig 4.2). The impact parameter is worked out for each of the tracks being considered, and if both of the tracks have an impact parameter too small, then the pair are rejected. The impact parameter cut initially applied was

$$TIMPACT \quad > \quad 0.05 \text{ cm}.$$

Other checks were also used to eliminate a lot of background events. No vertices are allowed upstream of the target i.e. we require

$$X_{VERTEX} \quad > \quad -180 \text{ cm}.$$

A low mass cut is made on the mass of V^0 candidates by insisting that

$$M_{V^0} \quad > \quad 0.35 \text{ GeV/c}^2.$$

This cut is required in order to eliminate γ conversions in the detectors. These form 'good' V^0's but have low mass. In addition, vertices with V^0 momentum greater than 100 GeV/c are not considered, in order to eliminate high momentum tracks from the production of a Δ^{++}. Also, no vertices are allowed downstream of the first measured points of the pair of tracks being considered.

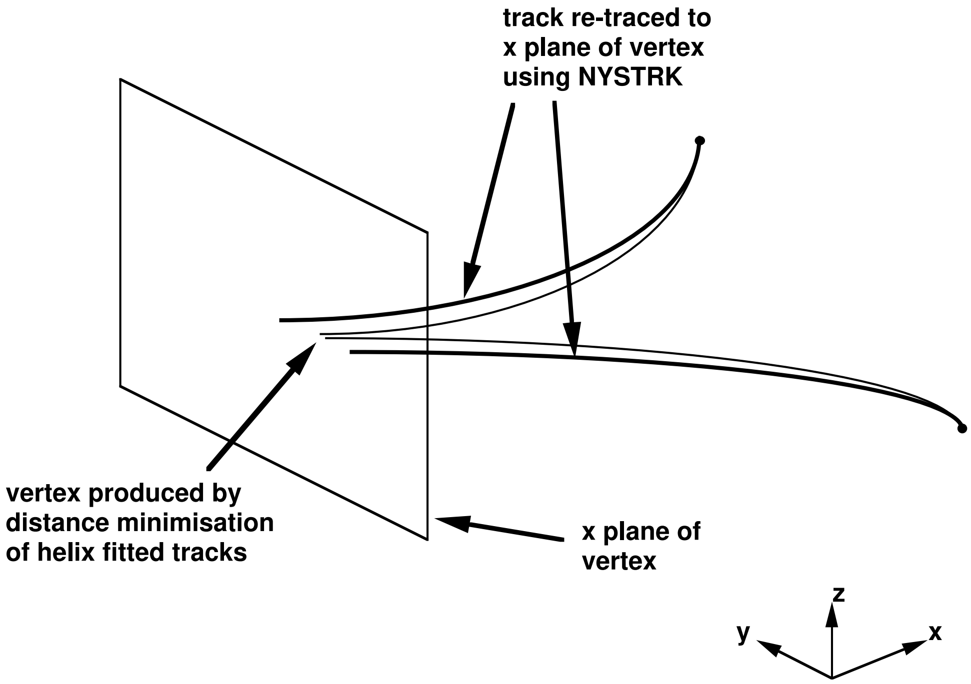

Figure 4.3: Illustration of how the V^0 program re-parameterises helix tracks.

4.3 Determination of accurate vertex position

The code basically has two stages, or iterations. In the first iteration, the direction cosines at the first measured points of all tracks being considered are used to parameterize helices, approximating the field in the Omega magnet to be constant. The code then uses a tracking routine which, given direction cosines and charge of a track, traces this track to any desired end plane in steps, using local field values at each point. Using this routine, the impact parameters at the x plane of the primary vertex can be established for pairs of tracks, and it is at this point that the $TIMPACT$ cut is implemented.

For pairs of tracks that have satisfied the *TIMPACT* cut, the program finds the point at which the distance between the two parameterized helices is at a minimum. The coordinates of this point are stored (see fig.4.3). Now, this position for the intersection point is inaccurate, since the approximation of constant field in the Omega magnet when parameterising the helices is inadequate. Because of the inaccuracy, vertex positions of up to 5 cm upstream of the primary vertex are accepted at this stage.

The inaccuracy of the helix minimisation necessitates the use of a second iteration. Both tracks of the V^0 candidate are now traced from their first points to 2 cm downstream of the x position of the helix minimisation previously established (as illustrated in fig.4.3) in steps of 1 cm, using the routine to take into account the changing field in Omega. Hence, this gives more accurate values for the track parameters in the region of the crude vertex position. Using the direction cosines of both of the tracks at this plane, the two tracks are re-parameterised as helices, and a second iteration ensues, giving a new and more accurate position for the secondary vertex. This vertex is then subject to all the cuts mentioned in section 4.2. If a vertex satisfies all of these criteria, and it is not made up of tracks where TRIDENT has found a V^0, then the vertex is considered to be a good V^0 candidate.

4.4 Optimisation of Signal to Background

Figure 4.4 shows the mass plot obtained for V^0 candidates satisfying the cuts of section 4.2, assuming both of the tracks making up the V^0 to be pions. A peak in the K^0 region (497.7 MeV/c^2) can clearly be seen, demonstrating that the V^0 program is picking out extra V^0's that were missed by TRIDENT. However, there is still a significant number of background events since the cuts described in section 4.2 were designed to eliminate a lot of background, and yet still be loose enough not to lose too many good events. Because of the low signal to background ratio (approx 1 : 1), a study was conducted into how to improve the existing cuts, and also to introduce new ones to optimise the signal to background ratio.

The method employed to optimise a particular cut was as follows. The cut was varied in steps, and mass plots were obtained for both events that passed the cuts

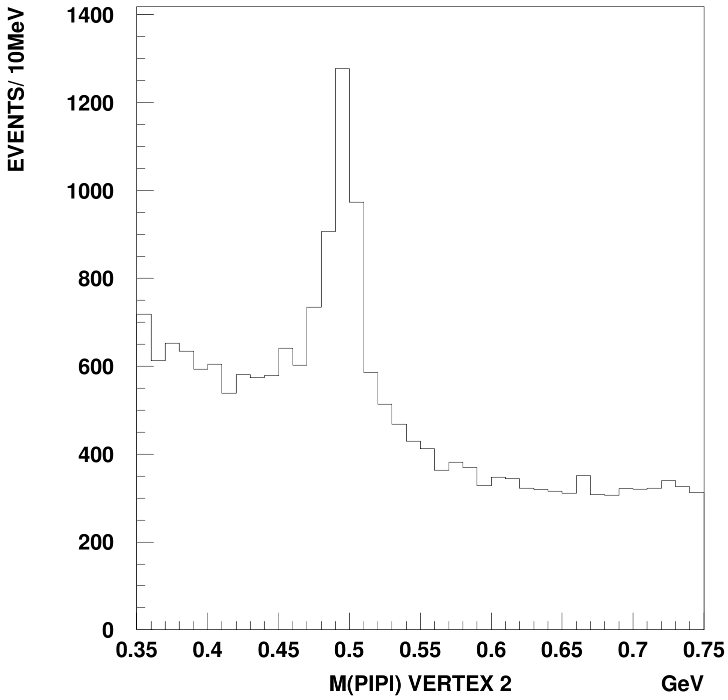

Figure 4.4: Mass plot for V^0 candidates from the V^0 program using the cuts described in section 4.2.

DIFFX (cm)	3	4	5	6	7	8
total	2234	1991	1804	1673	1551	1432
Background	915	780	610	545	472	390
No. of K^0's	1319	1211	1194	1128	1079	1042
Signal/ Bgnd	1.4	1.6	1.9	2.1	2.3	2.8

Table 4.1: Ratio of signal to background for the $\pi\pi$ mass spectrum for steadily increasing values of *DIFFX*.

and for those that failed. In this way, the events that a particular cut was rejecting could be examined, to establish whether good events were being discarded. At each stage, the signal to background ratio was calculated in the mass range

$$0.475 < \text{Mass } (\pi^+\pi^-) < 0.52 \text{ GeV/c}^2.$$

An example of how the signal to background ratio changed with different values of *DIFFX* is shown in table 4.1 where the signal to background ratio has been tabulated for increasing separation between primary and secondary vertices. In this way, the best value for *DIFFX* where the signal to background was good, and there was not too great a loss of events was established as being

$$DIFFX \quad > \quad 4 \text{ cm.}$$

As well as tightening up existing cuts, further cuts were implemented at this stage. An *ANGLE* cut was introduced. The angle between the momentum vector of the V^0 and the line of flight of the V^0 should be very small i.e. the V^0 should point back to the primary vertex. The distribution of this angle is shown in figure 4.5 (for no other cuts implemented). Table 4.2 gives representative figures for the different signal to background ratios obtained on varying the *ANGLE* cut. The optimum value for *ANGLE* was determined to be 3 degrees. Any vertices with an angle greater than this were rejected. In a similar manner, the optimum value for *FARMAX* was found to be

$$FARMAX \quad < \quad 0.175 \text{ cm.}$$

A tighter cut was also put on the maximum momentum of the V^0. No vertices were accepted where the V^0 momentum was greater than 25 GeV/c. The impact

ANGLE (deg)	4	3	2	1
total	2178	1991	1815	1345
Background	935	780	615	450
No. of K^0's	1243	1211	1200	895
Signal/ Bgnd	1.3	1.6	1.9	2.0

Table 4.2: Ratio of signal to background for the $\pi\pi$ mass spectrum for steadily increasing values of $ANGLE$.

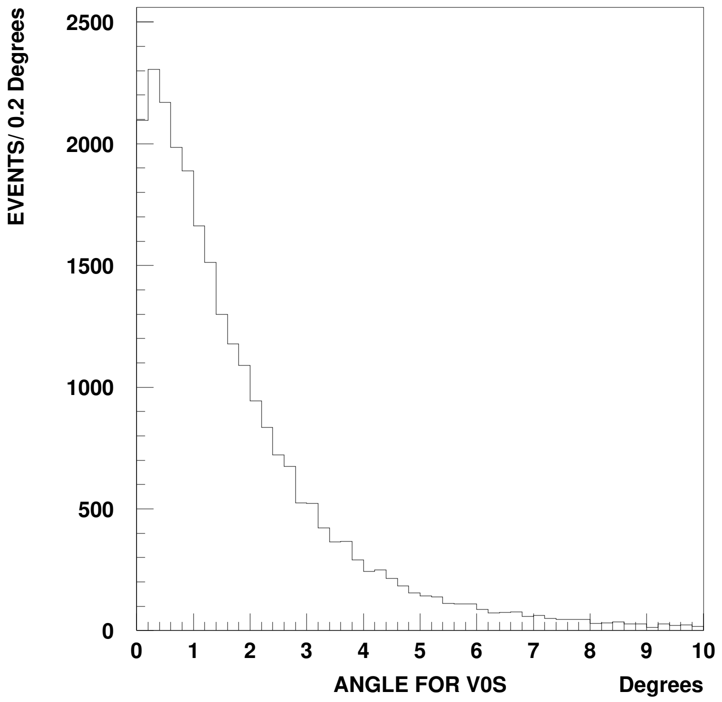

Figure 4.5: Angle between the V^0 and line of flight for V^0 candidates.

parameter was left at its previous value. The $\pi^+\pi^-$ mass spectrum with all of these cuts implemented is shown in figure 4.6. There is clearly some improvement, and the ratio of signal to background is now around $2:1$. One final cut was implemented

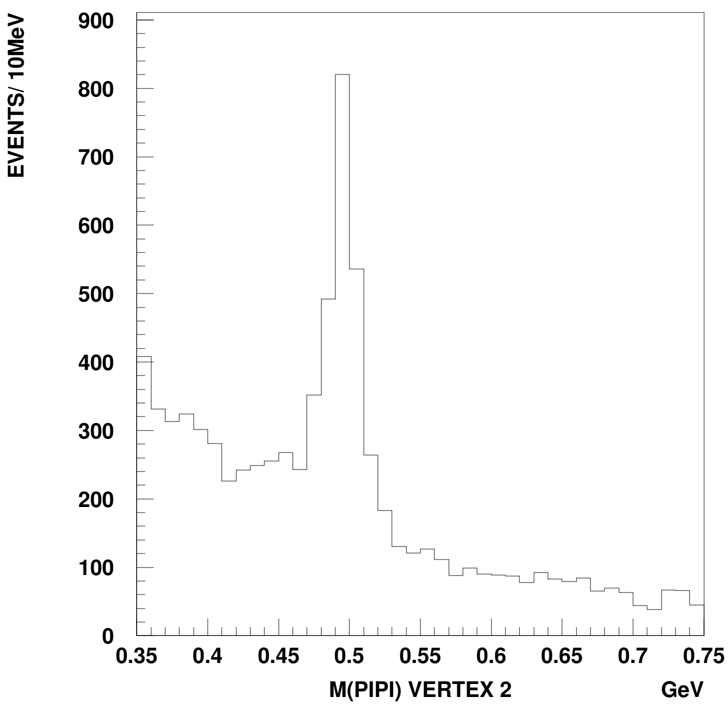

Figure 4.6: The $\pi^+\pi^-$mass spectrum for V^0 program events with tight cuts implemented.

at this point. An Armenteros-Podolanski plot [60] was made for V^0 candidates, where the q_T of the decay products of a V^0 (relative to the V^0) is plotted against the Armenteros alpha, α, defined by

$$\alpha = \frac{q_{L+} \; - \; q_{L-}}{q_{L+} \; + \; q_{L-}}$$

where q_L is the longitudinal momentum of the positive or negative decay particle. For a V^0 decaying into two equal mass particles, the plot will describe an ellipse centered on $\alpha = 0$. This can be seen in figure 4.7. In order to cut out a lot of spurious vertices, a low q_T cut was used. A lot of tracks at the low q_T end of the Armenteros plot may be due to electron conversions in the wire chambers and vertex detector. In order to eliminate these and low q_T background, a cut of

$$q_T \;\; > \;\; 0.06 \text{ GeV/c}$$

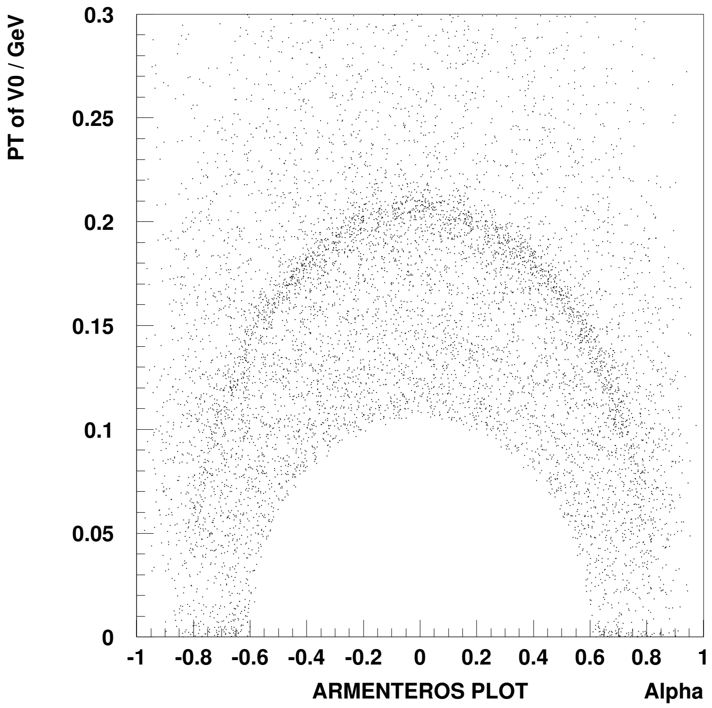

Figure 4.7: Armenteros-Podolanski plot for V^0's from the V^0 program.

was required for good vertices. Also, vertices lying outside the kinematic region of the K^0 by having too high q_T were eliminated by requiring that

$$q_T \ < \ 0.22 \text{ GeV/c}$$

for good V^0's. The $\pi^+\pi^-$mass spectrum obtained after insisting all the cuts previously described were passed is shown in figure 4.8. The signal to background has been significantly improved from that of the original loose cuts, the signal to background ratio now being approx. 2.5:1. In the K^0 mass region defined by

$$0.475 < \text{Mass } (\pi^+\pi^-) < 0.52 \text{ GeV/c}^2.$$

there are 2182 events.

4.5 Comparison with TRIDENT V^0's

Figure 4.9 shows the $\pi^+\pi^-$ mass spectrum for V^0's found by the TRIDENT program. The background is very much reduced in comparison to the data from the V^0 rescue program. In the K^0 mass region defined by

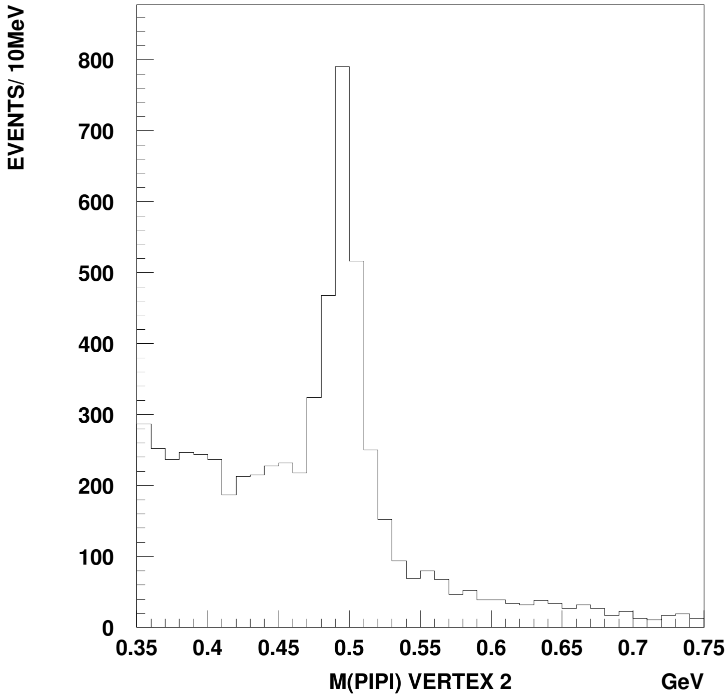

Figure 4.8: The $\pi^+\pi^-$mass spectrum after implementing all V^0 cuts.

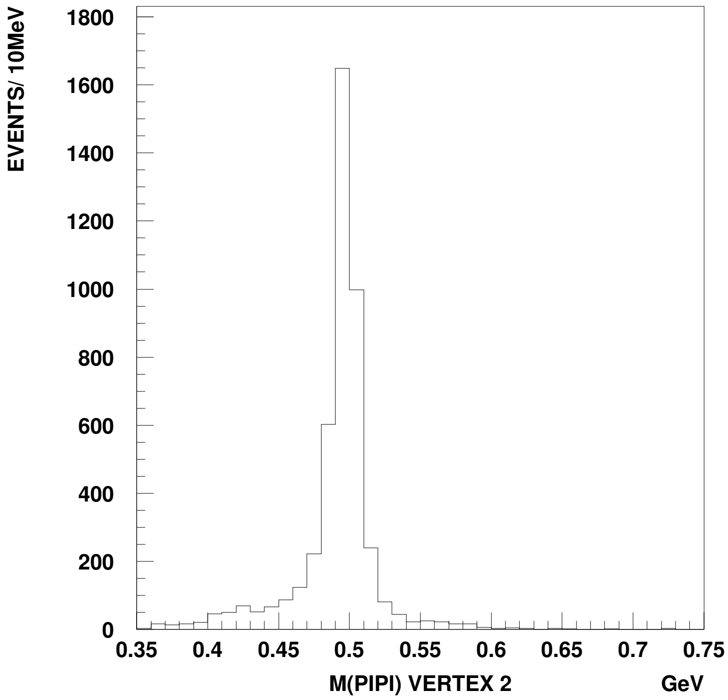

Figure 4.9: Mass plot for V^0 candidates from TRIDENT.

$$0.475 < \text{Mass } (\pi^+\pi^-) < 0.52 \text{ GeV/c}^2.$$

there are 3610 entries.

It is interesting at this stage to compare the distribution of *DIFFX*, the separation between primary and secondary vertices, for V^0's from the V^0 program and those from TRIDENT. Figure 4.10 shows the distributions for the two different sources of V^0's. The TRIDENT V^0's are shown hatched. It is apparent that the V^0 program is performing the task it was designed to do, since the vast majority of the vertices it finds are close to the primary vertex, in the first 20 cm downstream of it. There are very few TRIDENT vertices in the first 20 cm from the primary vertex, since vertices found by TRIDENT in this region would be likely to be tagged to the primary vertex. The x position of vertices found by the V^0 program and those found

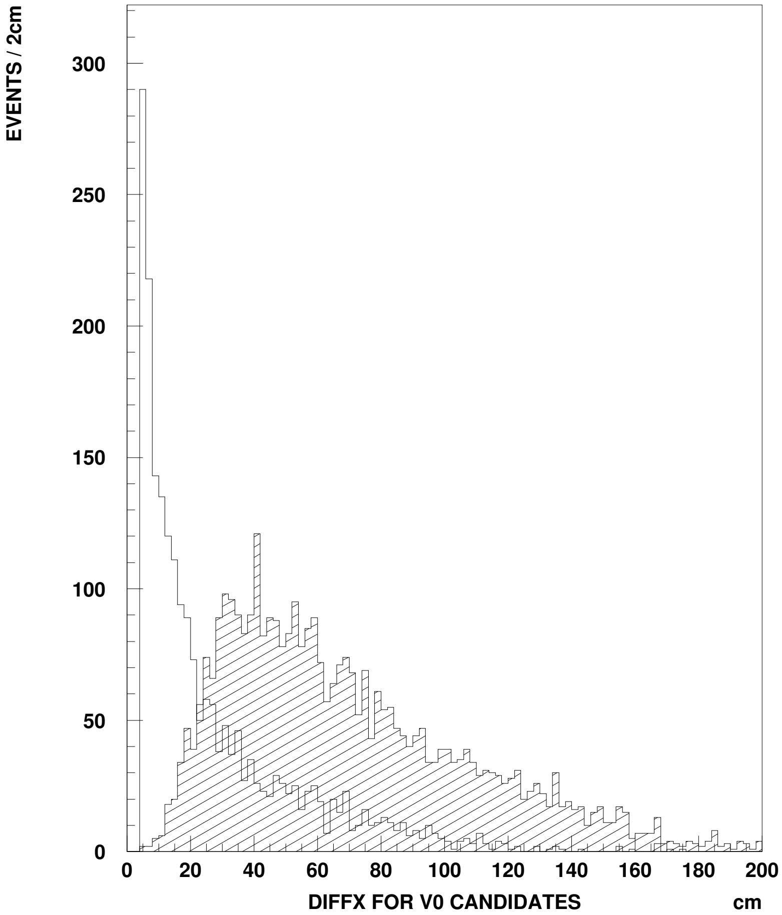

Figure 4.10: DIFFX distributions for TRIDENT V^0's (hatched) and V^0's from the V^0 program.

by TRIDENT (hatched) are shown in figure 4.11. The majority of vertices from the V^0 program are found within the target region (-180 to -120 cm), whereas the great majority of TRIDENT V^0's are outside it. A fit has been performed on the K^0 peak

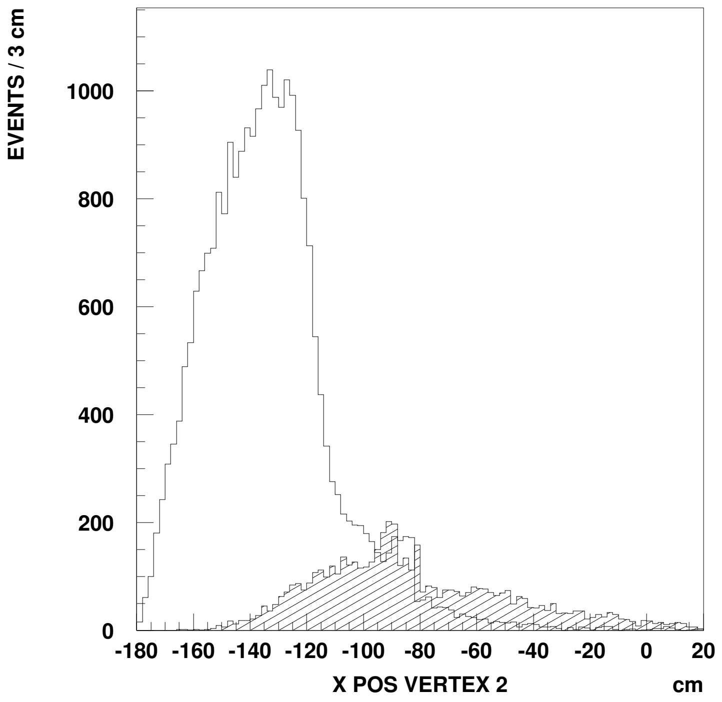

Figure 4.11: Distribution of vertex position for TRIDENT V^0's (hatched) and V^0's from the V^0 program.

for the TRIDENT data. It was found that a single Gaussian distribution could not describe the data well, but that two Gaussians were the minimum required to fit the data (with mass fixed at the K^0 mass) with the two having widths of

$$\begin{aligned}\sigma_1 &= 5 \text{ MeV} \\ \sigma_2 &= 12 \text{ MeV}.\end{aligned}$$

The fit is shown in figure 4.12.

A fit has also been performed for the K^0 peak for events from the V^0 program. A two Gaussian fit to the data gives the plot shown in figure 4.13. The two Gaussians have the following widths:

$$\begin{aligned}\sigma_1 &= 5 \text{ MeV} \\ \sigma_2 &= 15 \text{ MeV}.\end{aligned}$$

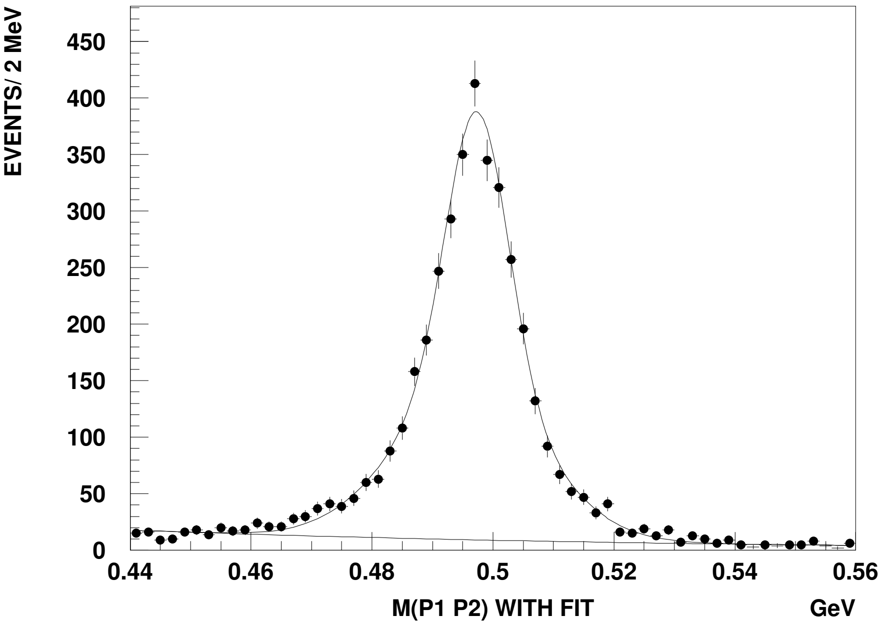

Figure 4.12: A two Gaussian fit to the TRIDENT $\pi^+\pi^-$mass spectrum.

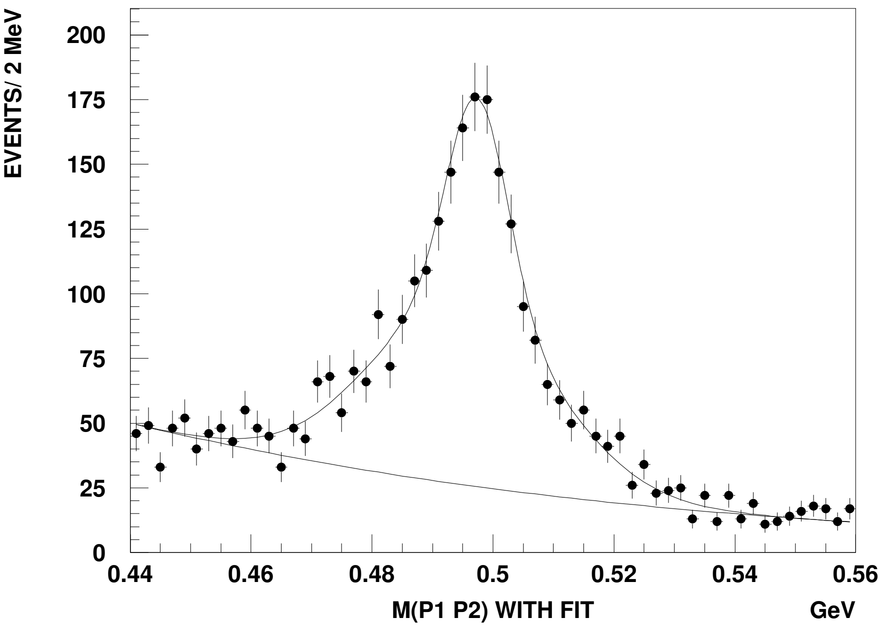

Figure 4.13: A two Gaussian fit to the V^0 program $\pi^+\pi^-$mass spectrum.

Cut	Value
Mass	$0.475 < \text{Mass}(\pi^+\pi^-) < 0.52$ GeV/c^2
Momentum	$p_{V^0} < 25$ GeV/c
Separation from primary vertex	DIFFX > 4 cm
Impact Parameter	TIMPACT > 0.05 cm
Angle	ANGLE < 3°
Vertex position	$X_{\text{VERTEX}} >$ -180 cm
Separation of V^0 tracks	FARMAX < 0.175 cm
Armenteros q_T	$0.06 < q_T < 0.22$ GeV/c

Table 4.3: Summary of the cuts used in obtaining V^0's for the V^0 recovery code.

Since there is more than one contribution to the resolution of tracks, then the observed distribution derives from the overlap of several Gaussians. Two Gaussians are the minimum required to describe the $\pi^+\pi^-$mass spectrum reasonably.

4.6 Conclusions

The V^0 program has been demonstrated to work, since it produces V^0's that were mis-assigned by TRIDENT. The background has been studied and V^0 cuts investigated in order to obtain an optimised signal to background ratio. The cuts used, and the final values of cuts are summarised in table 4.3.

The V^0 program is found to reconstruct most V^0's in the first 20 cm downstream of the primary vertex.

The efficiency of the V^0 recovery code for finding vertices was determined by generating vertices smeared to take into account the experimental resolution of WA91, and was found to be 67.9 %. The second iteration was demonstrated by this method to be an improvement on the naive approach using parameterised helices (for further details of this see Chapter 7).

When the events from the V^0 recovery code are are combined with the K^0's from TRIDENT, they yield the plot of figure 4.14.

The total K^0 peak has been fitted with two Gaussians, and the plot obtained is

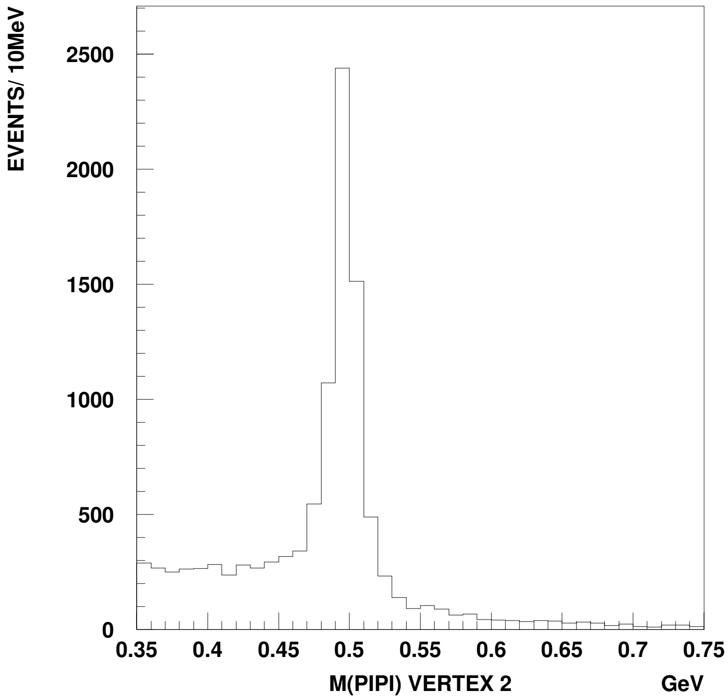

Figure 4.14: The $\pi^+\pi^-$mass spectrum for V^0's from both TRIDENT and the V^0 recovery program.

shown in figure 4.15

$$\sigma_1 = 14.3 \text{ MeV}$$
$$\sigma_2 = 5.0 \text{ MeV}.$$

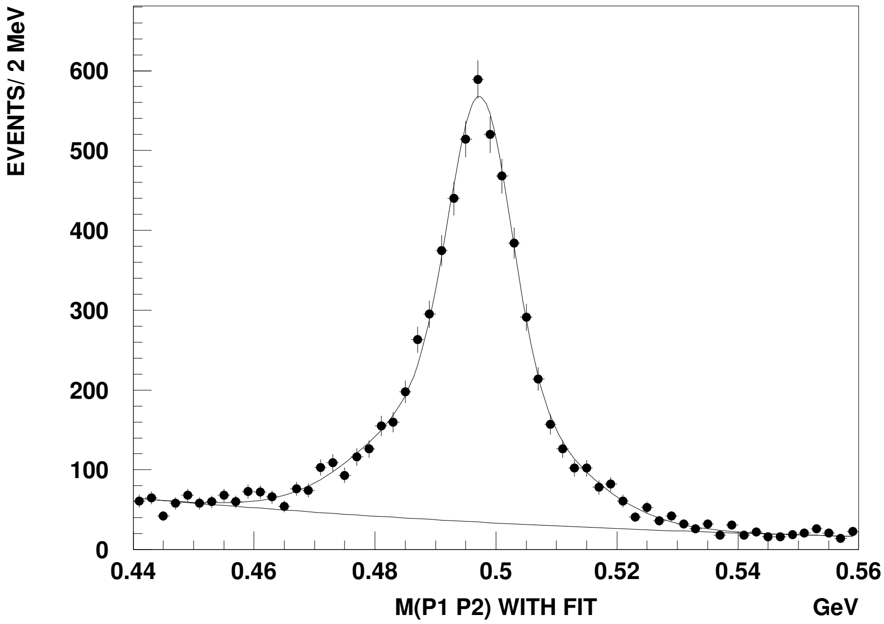

Figure 4.15: A two Gaussian fit to the total $\pi^+\pi^-$mass spectrum.

This total $\pi\pi$ mass spectrum represents the total number of K^0 events available for analysis of K^0 channels from the data taken in the experimental run in Autumn 1992. The total number of events in the K^0 mass region is 5792.

In conclusion, the V^0 program has been implemented successfully and produces 2182 K^0 events, this representing 38 % of K^0 events available for analysis.

Chapter 5

The $K^0_S K^\pm \pi^\mp$channel in WA91

5.1 Introduction

The $K^0_S K^\pm \pi^\mp$ mass spectrum is of considerable interest in meson spectroscopy, having been studied for many years. Several states of possible non-$q\overline{q}$ nature have been observed. There exists however a lot of uncertainty as to the number of states actually present, and the quantum number assignment for the observed states has often been ambiguous. The mass region around 1.4 GeV in particular has caused a lot of controversy over the issue of quantum numbers of states in the region, leading to the E/ι puzzle as described in chapter 3. It now appears that there are in fact three resonances in this region, the $f_1(1420)$, the $\eta(1440)$ and the $\eta(1490)$. The assignment of these mesons within the quark model is controversial, there being other candidates which seem better suited to the conventional $q\overline{q}$ assignment. The WA76 experiment has observed the $f_1(1420)$ in the centrally produced $K^0_S K^\pm \pi^\mp$ channel at 85 and 300 GeV/c [41],[45], and spin analysis of both sets of the data yielded the result $I^G(J^{PC}) = 0^+(1^{++})$. Re-analysis of the data using the combined data also found agreement with this result [61]. This section describes the means by which the WA91 central $K^0_S K^\pm \pi^\mp$ system at 450 GeV/c was selected, and how the masses and widths of the $f_1(1420)$ and the $f_1(1285)$ were determined.

5.2 Selection of the $K^0_S K^\pm \pi^\mp$channel.

The reaction

$$pp \rightarrow p_f(K^0_S K^\pm \pi^\mp)\ p_s$$

has been selected from WA91 events where there are four outgoing tracks together with a V^0 assigned for the event by imposing the following cuts on the missing momentum of an event:

$$\begin{aligned}
|\text{missing p}_x| &< 20.0 \text{ GeV/c} \\
|\text{missing p}_y| &< 0.16 \text{ GeV/c} \\
|\text{missing p}_z| &< 0.12 \text{ GeV/c}
\end{aligned}$$

A cut was made on the $\pi^+\pi^-$ mass for the reconstructed V^0, in order to select a K^0. The V^0 was required to have a mass in the K^0 mass window defined by

$$0.475 < \text{Mass } (\pi^+\pi^-) < 0.52 \text{ GeV/c}^2.$$

The reaction

$$pp \rightarrow p_f(K^0_S K^\pm \pi^\mp)\ p_s$$

was then selected from events where there is momentum balance and a K^0 by using energy conservation. The Δ function defined by:

$$\begin{aligned}
\Delta &= MM^2(p_f p_s) - M^2(K^0_S K^\pm \pi^\mp) \\
&= (E_{Beam} + E_{Target} - E_{Slow} - E_{Fast})^2 \\
&- (P_{Beam} + P_{Target} - P_{Slow} - P_{Fast})^2 \\
&- (E_{K^0} + E_+ + E_-)^2 \\
&+ (P_{K^0} + P_+ + P_-)^2
\end{aligned}$$

was used to select good events by requiring

$$|\Delta| < 1.6 \text{ (GeV/c}^2)^2.$$

The Δ function for uncut $K^0_S K^\pm \pi^\mp$ events is shown in figure 5.1. This cut was performed for both of the possible combinations of charged tracks, i.e. assuming a $\pi^+ K^-$ hypothesis and a $\pi^- K^+$ one, since there is an ambiguity as to the identity of the positive and negative track in $K^0_S K^\pm \pi^\mp$ events. Events where there was only one combination satisfying the Δ cut were assigned as being unambiguous. In cases where both combinations satisfied the cut, these were labelled as ambiguous.

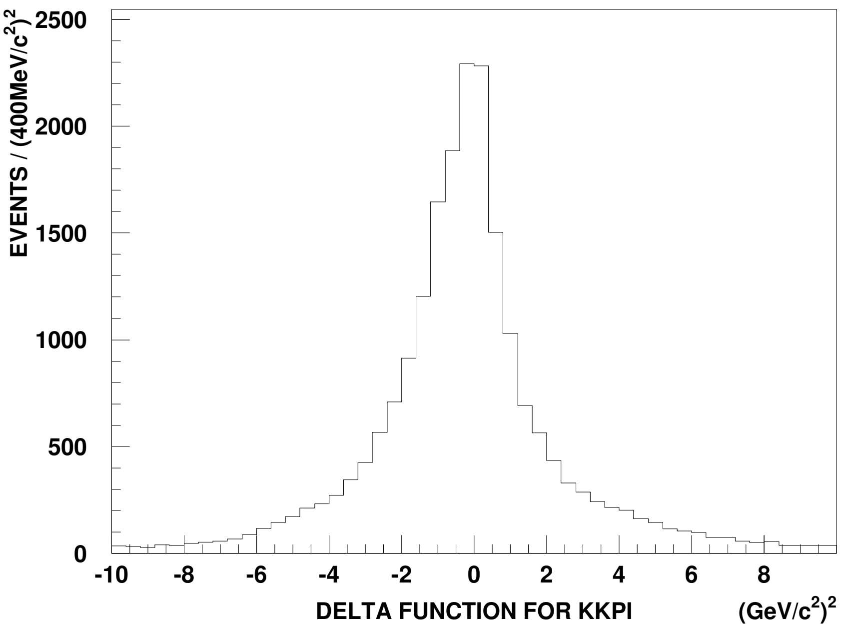

Figure 5.1: The Δ function for $K^0_S K^\pm \pi^\mp$ events from which good events were obtained using the cut described in the text.

In order to reduce the number of ambiguous events, the Ehrlich mass [62] was calculated for the V^0 and one of the charged tracks, assuming the other one to be a pion. Ehrlich mass is defined by

$$M_\pm^2 \;=\; \frac{(B^2 - (2P_{V^0}P_\pm)^2)}{4(P_{V^0}^2 + P_\pm^2 + B)}$$

where

$$B \;=\; (E_{Target} + E_{Beam} - E_{Fast} - E_{Slow} - E_\mp)^2 - (P_{V^0}^2 + P_\pm^2).$$

(See appendix A for details) The Ehrlich mass squared was calculated for both charged particle hypotheses for all events, and the plot obtained is shown in figure 5.2. Events where the particle identification has been made correctly will produce a peak at the kaon mass squared i.e. 0.244 (GeV/c^2)^2. Events previously flagged as ambiguous were now re-examined on the basis of the Ehrlich mass. Events where both hypotheses had Ehrlich mass squared of greater than the K^0 mass squared retained their ambiguous assignment. These were used in the subsequent analysis where both of the combinations were considered. For events where one or both combinations had Ehrlich mass less than the K^0 mass, the combination having the value of Ehrlich mass squared closest to the K^0 mass squared was considered to be the best combination and the flag of the event was re-assigned as unambiguous. Further, any events where both combinations of the Ehrlich mass squared fell below 0.1 $(\mathrm{GeV/c^2})^2$ were rejected, on the assumption that the event was a 4π event, in which two π's had been incorrectly identified as coming from a K^0 decay.

The Feynman x distribution for the $K^0_S K^\pm \pi^\mp$ system is shown in fig 5.3 showing a central $K^0_S K^\pm \pi^\mp$ system well separated from the fast and slow particles.

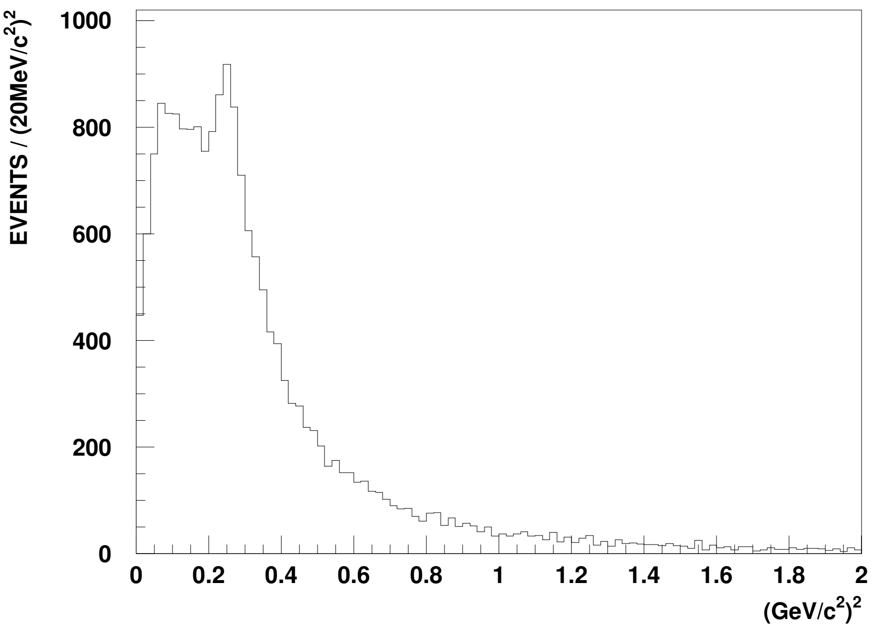

Figure 5.2: The Ehrlich mass squared for $K^0_S K^\pm \pi^\mp$ events.

Figure 5.4 shows the correlation between p_x for the kaon and the pion for the unambiguous assignments a) and for ambiguous assignments b). As can be seen in a), those events where the particles are correctly assigned have well separated momentum distributions, whereas if an ambiguity exists, then the values overlap greatly: particles have similar momenta, making the two possible assignments more difficult to distinguish.

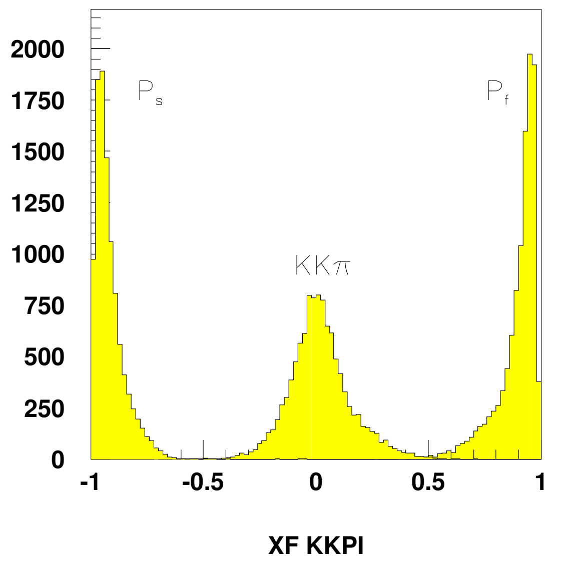

Figure 5.3: The Feynman x distribution for the centrally produced $K_S^0 K^{\pm}\pi^{\mp}$ system.

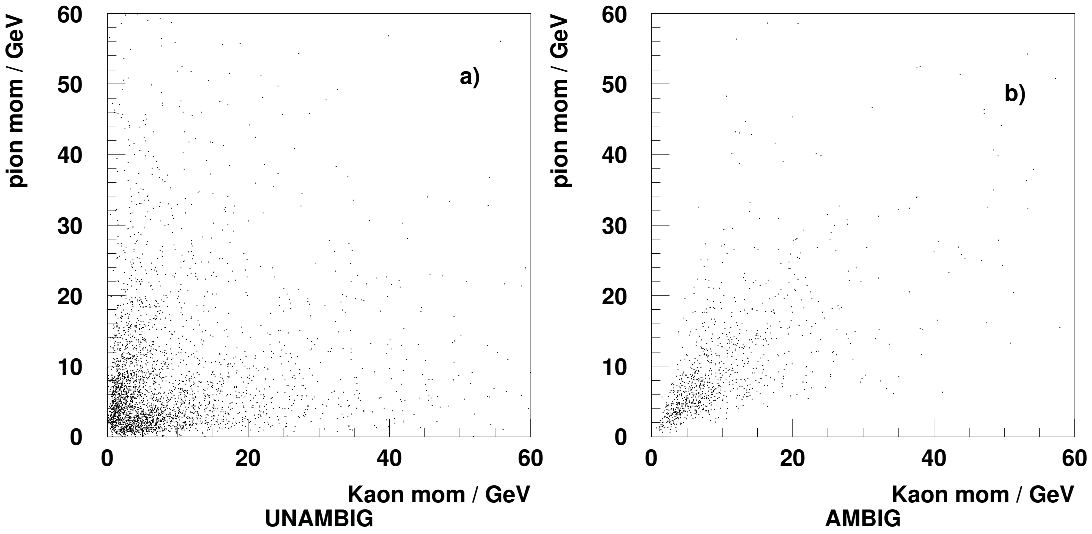

Figure 5.4: The p_x distribution for the kaon against pion for a) unambiguous events and b) for ambiguous events in the $K_S^0 K^{\pm}\pi^{\mp}$ spectrum.

5.3 The $K^0_S K^\pm \pi^\mp$ mass spectrum.

Using the criteria described above, a total of 3347 unambiguous events and 1086 ambiguous $K^0_S K^\pm \pi^\mp$ events were found. The ambiguous events were plotted twice. The $K^0_S K^\pm \pi^\mp$ mass spectrum is shown in figure 5.5 in the mass range

$$1.1 \ < \ \text{Mass}(K^0_S K^\pm \pi^\mp\ ) < 2.1 \ \text{GeV/c}^2$$

where 5.5 a) shows the spectrum for events where the K^0 was found using the V^0 recovery program, whilst 5.5 b) is for events where the K^0 was found by TRIDENT. Prominent $f_1(1285)$ and $f_1(1420)$ signals can be seen in both plots.

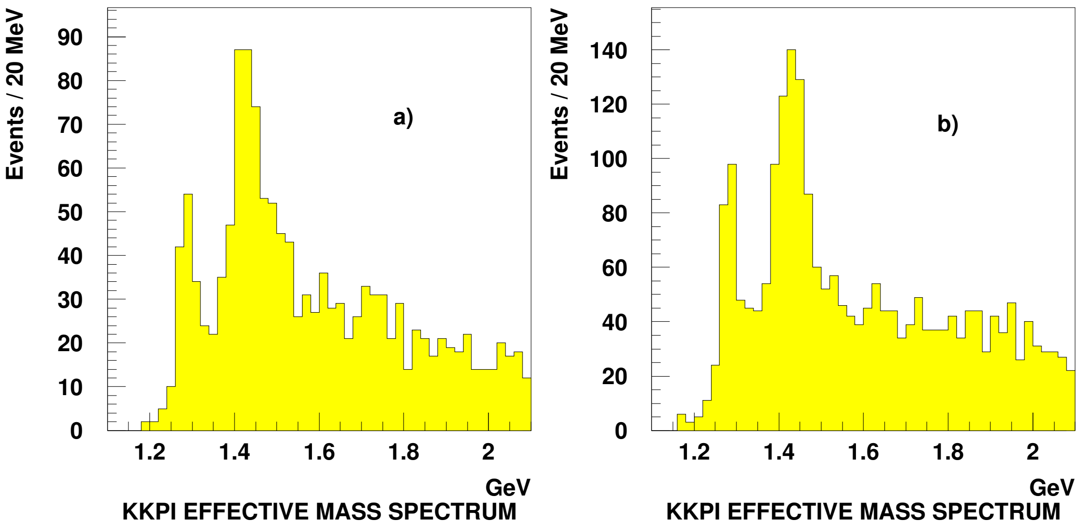

Figure 5.5: The $K^0_S K^\pm \pi^\mp$ mass spectrum for a) events where the K^0 has been found by the V^0 recovery code, and b) where the K^0 has been found by TRIDENT.

A fit to the combined $K^0_S K^\pm \pi^\mp$ mass spectrum in the mass region 1.1 < Mass($K^0_S K^\pm \pi^\mp$) < 2.1 GeV/c^2 (4049 entries) has been performed using a relativistic Breit-Wigner convoluted with a Gaussian to describe each of the two resonances. The fit is shown in figure 5.6 The equation used to produce the background fit was of the form

$$\text{Bckgnd}(m) \ = \ a(m - m_{th})^b exp(-cm - dm^2)$$

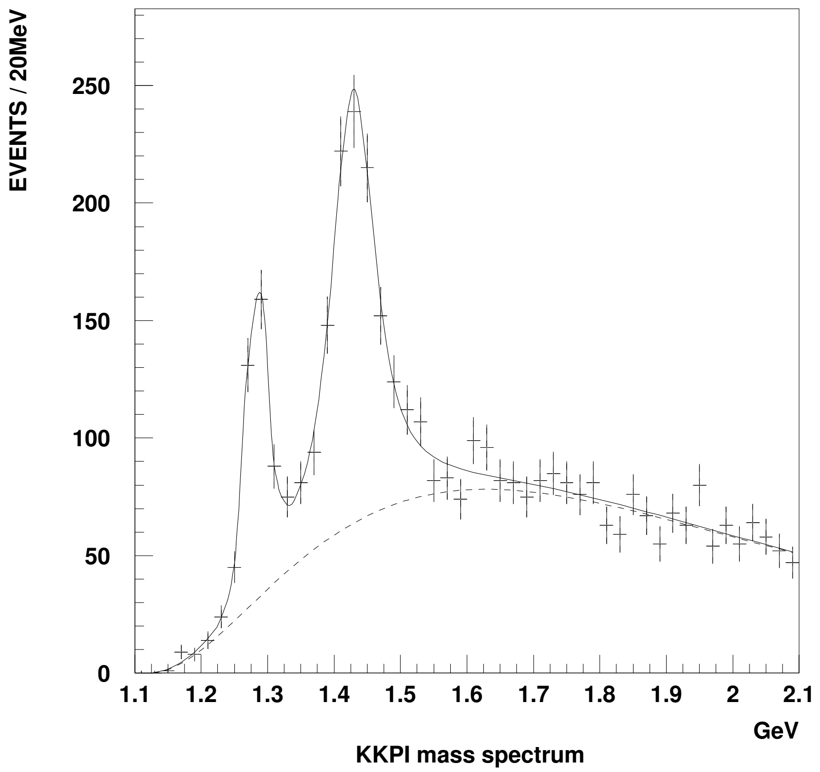

Figure 5.6: The combined $K_S^0 K^{\pm}\pi^{\mp}$ mass spectrum with fit as described in the text.

where m_{th} is the threshold mass for the $K_S^0 K^\pm \pi^\mp$ system. The Breit-Wigner Gaussian convolution formula used to describe the two resonances was of the form

$$\text{bwcon}(m) = \int_{m'_{low}}^{m'_{high}} Gauss(m'-m) BW(m', m_{meson}) dm'$$

where bwcon(m) is the calculated contribution for each value m, summing over m', the full mass range of the meson, $Gauss(m'-m)$ is a Gaussian centred at $m'-m$ from the peak of the meson, and BW is the value of the relativistic Breit-Wigner at m'. The widths of the Gaussians for each of the two convoluted functions was established by the use of a Monte-Carlo simulation of the decay of an X^0 system to $K_S^0 K^\pm \pi^\mp$. The $\pi^+\pi^-$ mass spectrum generated was calibrated to the $\pi^+\pi^-$ spectrum from data, and the smearing required on the two π tracks was applied to the other two tracks of the event, in order to obtain $K_S^0 K^\pm \pi^\mp$ smeared events. The Gaussian widths in the $f_1(1285)$ and $f_1(1420)$ mass windows were then established by plotting the difference between generated events and the same events after smearing, giving the resolution. The widths used in the fit were:

$$f_1(1285) \ : \sigma = 10 \text{ MeV/c}^2$$
$$f_1(1420) \ : \sigma = 13 \text{ MeV/c}^2$$

The parameters obtained from the fit for the two resonances were

$$\begin{aligned} \text{M}_{f(1285)} &= 1281 \pm 2 \text{ MeV/c}^2 \\ \Gamma_{f(1285)} &= 19 \pm 5 \text{ MeV/c}^2 \\ \text{M}_{f(1420)} &= 1426 \pm 2 \text{ MeV/c}^2 \\ \Gamma_{f(1420)} &= 61 \pm 7 \text{ MeV/c}^2 \end{aligned}$$

which are in good agreement with the Particle Data Group values for the two mesons [36]:

$$\begin{aligned} \text{M}_{f(1285)} &= 1282 \pm 5 \text{ MeV/c}^2 \\ \Gamma_{f(1285)} &= 24 \pm 3 \text{ MeV/c}^2 \\ \text{M}_{f(1420)} &= 1426.8 \pm 2.3 \text{ MeV/c}^2 \\ \Gamma_{f(1420)} &= 52 \pm 4 \text{ MeV/c}^2. \end{aligned}$$

The $f_1(1420)$ PDG values are mean values derived from $p\overline{p}$ annihilation, and J/Ψ decay as well as central production.

5.4 Geometrical Acceptance for the $K_S^0K^{\pm}\pi^{\mp}$ channel

To study the acceptance, $K_S^0K^{\pm}\pi^{\mp}$ events were produced from real 2π events by mixing these events so that there were four outgoing tracks. It was then required that one pair of π's in each event had an effective mass compatible with being a K^0 i.e. that

$$0.45 < \text{Mass } (\pi^+\pi^-) < 0.55 \text{ GeV/c}^2.$$

Pairs of tracks satisfying this criterion were combined to form a K^0 which was then allowed to decay exponentially. The other two charged tracks in the event were then re-assigned as being a π and a K, and in this way $K_S^0K^{\pm}\pi^{\mp}$ events were produced.

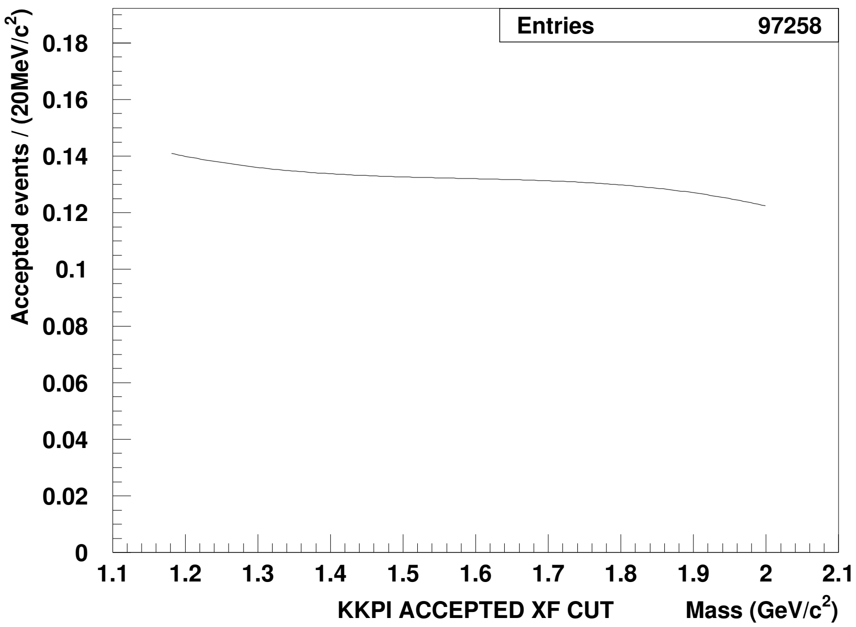

Figure 5.7: Acceptance as a function of effective mass for $K_S^0K^{\pm}\pi^{\mp}$ events.

Each of these events was rotated around the x-axis (ϕ), and assigned different vertex positions in the target, producing ten different values of ϕ and vertex position for each event. Each track of the event was then tested to see if it would be accepted by the WA91 detector system. The fractional acceptance for $K_S^0K^{\pm}\pi^{\mp}$ events as a function of effective mass was calculated in this way, and found to decrease smoothly with effective mass as shown in figure 5.7.

Chapter 6

Spin Parity Analysis of the $K_S^0 K^\pm \pi^\mp$channel in WA91

6.1 Introduction

When a particle decays, the distribution in space of the decay products depend upon the spin of the original particle. In the simplest case, that of a spin zero object, it will decay isotropically in its centre of mass. For non-zero spin, an angular dependence enters into the decay. Because of this, by measuring the distribution of the decay products of an object, it should be possible to ascertain the spin of the original object. So, for a clear resonance signal with a uniform background, it should in principle be possible to reproduce the spin of the resonance unambiguously. This picture is made somewhat more complicated when trying to separate events out from background, however. Difficulties arise when trying to separate the resonance from a background which may not be isotropic, or may even have originated from a resonance broader than the one under investigation. The production method may also have affected the distribution of decay products. The way that this situation is usually resolved is to perform a partial wave analysis, summing over the possible quantum spin states of both final and initial state particles, in order to produce an expression for the angular distribution. This method becomes unworkable in the case of the $K_S^0 K^\pm \pi^\mp$ channel of the WA91 experiment, however, since we have a double exchange process followed by a three body decay.

Because of this, the only practical method available is one in which only the decay of the resonance is considered, and which does not take into account how the resonance was generated. The method that was considered in the $K_S^0 K^\pm \pi^\mp$ channel spin analysis was the Standard Isobar Model, using Zemach Tensors to describe the spin of the decaying particle. An outline of this method is described below.

6.2 Dalitz Plot analysis using Zemach Formalism

6.2.1 Degrees of freedom

Consider a particle X that decays into three particles a, b and c in the centre of mass of X. Now, each of the particles has four degrees of freedom (three components of momentum and energy). However, since we know for a specific decay the identity of each of the decay products, and that each must satisfy $E^2 - p^2 = m^2$, then this eliminates three of the degrees of freedom. Because we are in the centre of mass frame, we also know that total momentum is zero, and that the total energy of the system is equal to the mass of X. This eliminates a further four degrees of freedom, leaving five degrees to describe the decay. These can be chosen to be the three Euler angles defining the decay plane of the $K_S^0 K^\pm \pi^\mp$ event (all are in the same plane since the total momentum is zero), and two other variables related to the energy/momentum of the $K_S^0 K^\pm \pi^\mp$ system. For these two other variables we choose the mass squared of pairs of particles, for reasons described subsequently.

We integrate over the decay plane orientation (i.e. the decay plane is not considered in the analysis) since this means that we do not have to take into account how the resonance was produced. This now leaves only two degrees of freedom, the effective mass squared of pairs of particles. A plot of the effective mass squared of one pair of particles against the other for a three body decay constitutes a Dalitz Plot. This plot will now contain all the information we can know for a particular event, and for the spin of X. The drawback in using this method is that in an effort to simplify the analysis situation we have now lost information about the production mechanism for X.

6.2.2 The Standard Isobar Model

The Standard Isobar Model is one which describes a three-body decay to pseudoscalars a, b and c by parameterizing it in terms of sequential two-body decays. Consider the sequence as depicted in figure 6.1 where a state X decays to particle c and an intermediate resonance Y, which subsequently decays. The Zemach tensor method uses observed quantities of the final state particles to describe the decay, in terms of traceless, symmetric tensors of order J, where J is the spin of the initial resonance X.

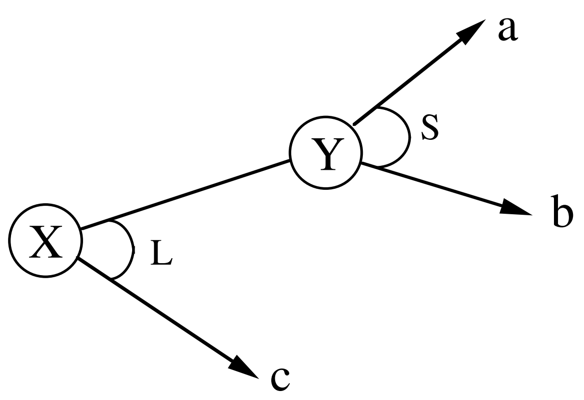

Figure 6.1: The Isobar model for representing a three body final state *via* an intermediate resonance, Y.

If the intermediate resonance Y has spin S, then we can represent this using the momentum vectors of a and b. Let $\mathbf{p}_a^*$ be the 4-vector describing the particle a, and $\mathbf{p}_b^*$ be the 4-vector that describes b in the rest frame of Y. The matrix elements describing the tensor Y for various spin values can now be constructed from these.

For S = 0, then the tensor is chosen to be a constant, in this case 1. For S = 1, then a vector is required. The vector $\mathbf{t}$ is chosen, where $\mathbf{t}$ is the relative momentum of the two particles associated with the intermediate resonance Y, in the rest frame of Y, i.e.

$$\mathbf{t} = \mathbf{p}_a^* - \mathbf{p}_b^*$$

For the Zemach method, this vector has to be expressed in terms of the corresponding

S	Tensor
0	1
1	$\mathbf{t}$
2	$\frac{1}{2}(\mathbf{t}^i\mathbf{t}^j+\mathbf{t}^j\mathbf{t}^i)$-$\frac{1}{3}\delta^{ij}(\mathbf{t}.\mathbf{t})$

Table 6.1: Tensors describing the intermediate resonance Y, of spin S.

momenta in the overall rest frame, that of the initial resonance X:

$$\mathbf{t} = \mathbf{p}_a - \mathbf{p}_b - (\frac{m_a^2 - m_b^2}{m_{ab}^2})(\mathbf{p}_a + \mathbf{p}_b).$$

For an S = 2 object, the spin has to be represented by a second order tensor, constructed from the vector $\mathbf{t}$, which is $\frac{1}{2}(\mathbf{t}^i\mathbf{t}^j+\mathbf{t}^j\mathbf{t}^i)$-$\frac{1}{3}\delta^{ij}(\mathbf{t}.\mathbf{t})$, where i and j represent the cartesian components of the vector $\mathbf{t}$. The tensors describing the spin of Y, for spin values up to 2 are shown in table 6.1. The angular momentum L, between the intermediate state Y and the third particle, c, may be expressed in a similar manner, except that in this case $\mathbf{t}$ is replaced by $\mathbf{p}_c$, the momentum vector of c in the rest frame of X.

Now, the initial state X of spin-parity J^P can be constructed by combining L and S for each possibility. The overall parity of the state is produced by combining the intrinsic parities of the three decay particles a,b and c with the contributions due to the spin of intermediate state Y, S, and the angular momentum between Y and c, L. Since particles a, b and c are pseudoscalars and have negative intrinsic parity, then the overall parity is given by

$$\mathrm{P} = (-1)^L(-1)^S(-1)(-1)(-1) = (-1)^{L+S+1}.$$

Examples of the construction of several of the J^P states are listed below:

- In the case where L=0 and S=0 , then the resulting state from combining these two has to be $J^P = 0^-$. This can be represented by the scalar quantity 1.

- For a state where S=0 and L=1, then the state is $J^P = 1^+$, a vector. This state is represented by combining the L=1 vector, $\mathbf{p}_c$ with a scalar, making the overall representation $\mathbf{p}_c$.

J^P	L	S	Tensor
0^-	0	0	scalar
0^-	1	1	$\mathbf{t}.\mathbf{p}_c$
1^-	1	1	$\mathbf{t}\times\mathbf{p}_c$
1^+	0	1	$\mathbf{t}$
1^+	1	0	$\mathbf{p}_c$
2^-	1	1	$\frac{1}{2}(\mathbf{t}^i\mathbf{p}_c^j+\mathbf{t}^j\mathbf{p}_c^i)$-$\frac{1}{3}\delta^{ij}(\mathbf{t}.\mathbf{p}_c)$.

Table 6.2: Tensor constructions describing the state X, for different J^P values.

- For a state where S=0 and L=2, then the state is $J^P = 2^-$. The tensor to represent this state by is formed by combining the L=2 tensor, $\frac{1}{2}(\mathbf{p}^i\mathbf{p}^j+\mathbf{p}^j\mathbf{p}^i)$ -$\frac{1}{3}\delta^{ij}(\mathbf{p}_c.\mathbf{p}_c)$, with the scalar representing S=0, making the overall representation $\frac{1}{2}(\mathbf{p}^i\mathbf{p}^j+\mathbf{p}^j\mathbf{p}^i)$ -$\frac{1}{3}\delta^{ij}(\mathbf{p}_c.\mathbf{p}_c)$.

  For the case where S=1 and L=1, then there are three possible states that can be formed, 0^-, 1^- and 2^-.

  - 0^- is a scalar state and as such has to be represented by a combining the S=1 representation ($\mathbf{t}$) with the L=1 representation ($\mathbf{p}_c$) in such a way as to produce a scalar. This is done by taking the dot product between the two vectors i.e. the state is represented by $\mathbf{t}.\mathbf{p}_c$
  - 1^- is a vector and as such is produced by combining the two vectors $\mathbf{t}$ and $\mathbf{p}_c$ to form another vector. Hence, the state is represented by $\mathbf{t}\times\mathbf{p}_c$.
  - 2^- is a tensor state and is produced from combining $\mathbf{t}$ and $\mathbf{p}_c$ to form a tensor of the same form as the S=2 tensor in table 6.1. The state is thus represented by $\frac{1}{2}(\mathbf{t}^i\mathbf{p}_c^j+\mathbf{t}^j\mathbf{p}_c^i)$ -$\frac{1}{3}\delta^{ij}(\mathbf{t}.\mathbf{p}_c)$.

Table 6.2 lists the J^P tensor constructions for various values of J^P.

6.3 Matrix elements used in $K_S^0K^\pm\pi^\mp$ spin analysis

In the Isobar model, the intermediate resonance Y must be represented by a function to describe it. In this analysis a Breit-Wigner is used to describe the intermediate state.

In the case of the $K^0_S K^\pm \pi^\mp$ channel, there are two possible intermediate states, the K^* or the $a_0(980)$ (which was previously named the δ), since the two possible reactions are :

$$K^* \, \overline{K} \rightarrow K^0_S K^\pm \pi^\mp$$
$$\pi \; a_0(980) \rightarrow K^0_S K^\pm \pi^\mp \; .$$

6.3.1 Representation of the K^* intermediate resonance.

The mass dependence of the K^* was represented using a relativistic Breit Wigner of the form

$$BW(K^*) \;=\; \frac{\sqrt{m\Gamma(q)/q}}{m_0^2 - m^2 - i m_0 \Gamma(q)}$$

where

$$\begin{aligned}
\Gamma(q) &= \Gamma_0 (q/q_0)^{2L+1} (2q_0^2/(q_0^2 + q^2) \\
q_0 &= \frac{\sqrt{\Lambda(m_0^2, m_\pi^2, m_K^2)}}{2m_0^2} \\
q &= \frac{\sqrt{\Lambda(m^2, m_\pi^2, m_K^2)}}{2m^2} \\
\Lambda(a,b,c) &= a^2 + b^2 + c^2 - 2ab - 2ac - 2bc \\
m_0 &= m(K^*) \;=\; 0.8921 \text{ GeV/c}^2 \\
m &= m(K\pi) \\
\Gamma_0 &= \Gamma(K^*) \;=\; 0.0513 \text{ GeV/c}^2.
\end{aligned}$$

6.3.2 Representation of the $a_0(980)$ intermediate resonance.

This is a more complicated situation than the K^*, since the $a_0(980)$ has two possible decay modes, one to $\eta\pi$ and the other to $K\overline{K}$. In view of this, it has to be represented by a coupled channel Breit Wigner. The Flatté formalism [66] was used where:

$$\begin{aligned}
BW(a_0(980)) &= 0 \quad \text{below } K\overline{K} \text{ threshold} \\
BW(a_0(980)) &= \frac{m_0 \sqrt{\Gamma(\eta\pi)\Gamma(K\overline{K})}}{m_0^2 - m^2 - i m_0 (\Gamma(\eta\pi) + \Gamma(K\overline{K})} \quad \text{above threshold.} \\
\text{where } m_0 &= m(a_0(980)) \\
\text{and } m &= m(K\overline{K})
\end{aligned}$$

Now, $\Gamma(K\overline{K}) = g_K q_K$ and $\Gamma(\eta\pi) = g_\eta q_\eta$ where g_K and g_η may be regarded as the coupling constants squared for the coupling of the resonance to $K\overline{K}$ and $\eta\pi$ respectively. The quantities q_K and q_η are the decay momentum values of the mass m into a $K\overline{K}$ or $\eta\pi$ system respectively. By considering a two body decay in the centre of mass of the $a_0(980)$ it can be shown that

$$q_\eta = \frac{\sqrt{(m^2 - (m_\eta + m_\pi)^2)(m^2 - (m_\eta - m_\pi)^2)}}{2m}.$$

In the case of the $K\overline{K}$ system then $m_K = m_{\overline{K}}$ and the expression for q_K in this case becomes

$$q_K = \sqrt{(m^2/4 - m_K^2)}.$$

The prediction of $g_K/g_\eta = 3/2$ has been used [67].

In order to produce a matrix element to represent the spin-parity of the initial state X, the Breit-Wigner representation for the particular intermediate resonance, the $a_0(980)$ or the K^*, must be combined with the tensor term for that spin-parity.

In instances where the intermediate resonance can be present in more than one possible charged state, then the total amplitude is constructed by summing over all the possible amplitudes, together with the appropriate Clebsch-Gordan coefficient of Isospin. The $K_S^0 K^\pm \pi^\mp$ final state from $K^*\ \overline{K}$ decay can be produced *via* either a neutral or a charged K^*, and so the Clebsch Gordan coefficient is given by:

$$\frac{1}{\sqrt{2}}(|K^{*0}\rangle|K^0\rangle \ + \ |K^{*\pm}\rangle|K^\mp\rangle) \ = \ \frac{1}{\sqrt{6}}(|K^*\rangle|\overline{K}\rangle)$$

Also, since the K^* can also occur as $\overline{K}^*$ then this must be taken into account in the final matrix element which becomes

$$\mathcal{M} \ = \ \frac{1}{\sqrt{6}}(BW_1.\mathcal{M}_1 \ + G.BW_2.\mathcal{M}_2)$$

where G is related to the C parity of the of the parent particle by [2]:

$$\mathrm{C} \ = \ (-1)^I \mathrm{G}$$

(see Appendix B for further details).

Now, since the $a_0(980)$ has $J^P = 0^+$, then in table 6.2 only the waves where S = 0 can be described by the $a_0(980)$. In the same way, since the K^* has $J^P = 1^-$ then only the S = 1 waves can be represented by the K^*.

J^P	L	Decay Mode	Amplitude
0^-	S	$a_0(980)\pi$	coupled channel(a_0)
0^-	P	K^*K	BW(K^*_{ab})$\mathbf{t}_c.\mathbf{p}_c$ +G.BW(K^*_{ac})$\mathbf{t}_b.\mathbf{p}_b$
1^-	P	K^*K	BW(K^*_{ab})$\mathbf{t}_c\times\mathbf{p}_c$ +G.BW(K^*_{ac})$\mathbf{t}_b\times\mathbf{p}_b$
1^+	S	K^*K	BW(K^*_{ab})$\mathbf{t}_c$ +G.BW(K^*_{ac})$\mathbf{t}_b$
1^+	P	$a_0(980)\pi$	coupled channel(a_0)$\mathbf{p}_a$
1^+	D	K^*K	BW(K^*_{ab})[$\mathbf{p}_c(\mathbf{t}_c.\mathbf{p}_c)$ -$\frac{1}{3}(\mathbf{p}_c.\mathbf{p}_c)\mathbf{t}_c$]
			+G.BW(K^*_{ab})[$\mathbf{p}_b(\mathbf{t}_b.\mathbf{p}_b)$ -$\frac{1}{3}(\mathbf{p}_b.\mathbf{p}_b)\mathbf{t}_b$]

Table 6.3: The matrix elements used in the $K^0_S K^\pm \pi^\mp$ analysis to describe waves of different spin-parity.

For example, consider the $J^P L = 0^- P$ state. This must be described by a K^*K decay. Since the overall spin is zero, then the tensors describing the intermediate state Y and the third particle must be combined is such a way as to produce a scalar, so the dot product is taken between **t** and **p**. Then the final matrix element is the sum of the two possible terms for the K^* and $\overline{K}^*$, with the appropriate Clebsch Gordan coefficient.

The matrix elements representing the different spin parity waves used in the spin analysis of the $K^0_S K^\pm \pi^\mp$ channel are shown in table 6.3.

6.4 The Dalitz Plot

In a Dalitz plot, we have summarised all the information we can know about the decay of the resonance X to a three body system. In the simplest case of a three body decay, then three body phase space implies that if we plot the energies of any two of the final state particle (say E_1 and E_2) against each other, then the density of events per unit area (i.e. per unit of $dE_1 dE_2$) should be uniform i.e.

$$d^2\rho = const.dE_1 dE_2.$$

However, if the integral over the three Euler angles (θ, ϕ, ϕ_z) defining the decay plane orientation

$$\int d\theta d\phi d\phi_z |\mathcal{M}|^2$$

(where $\mathcal{M}$ is the matrix element for the decay) has any dependence upon the energies or momenta of the decay particles, then a uniform distribution will not be produced in the E_1 vs E_2 plane:

$$d^2\rho = const.dE_1 dE_2 \int d\theta d\phi d\phi_z |\mathcal{M}|^2.$$

This means that the the density at any point in the Dalitz plot is a measure of the square of the decay matrix element. Any departure from a uniform distribution is indicative of a dependence of the matrix element upon the energies or momenta of the decaying particle. Since the Zemach formalism gives us a way of representing the matrix elements in terms of different spin parity states and intermediate resonances, then we can use Zemach tensors to determine the combination that provides the best description of the observed Dalitz plot distribution. We are essentially fitting the Dalitz plot.

In a Dalitz plot, a choice can be made of what combinations of particles are plotted against each other in order to best perform the spin analysis. There are four reactions that can occur to generate the final $K^0_S K^\pm \pi^\mp$ state as below:

$$\begin{aligned}
K^{*+}K^- &\rightarrow (\pi^+ K^0)K^- \\
K^{*0}\overline{K}^0 &\rightarrow (\pi^- K^+)\overline{K}^0 \\
K^{*-}K^+ &\rightarrow (\pi^- \overline{K}^0)K^+ \\
\overline{K}^{*0}K^0 &\rightarrow (\pi^+ K^-)K^0.
\end{aligned}$$

There are two possible combinations of particles that can be plotted against each other. Firstly, we could consider together both $K^*\overline{K}$ and $\overline{K}^*K$ combinations, and plot these against each other. Alternatively, we can consider the $K^*_{charged}K$ and $K^*_{neutral}K$ reactions together, where in this case the $K^0\pi^\pm$ and $K^\pm\pi^\mp$ mass squared values could be plotted against each other. Now, K^*_{ch} and K^*_{ne} production can be expected to be different for background events, incoherent K^*K production showing up as an asymmetry between the K^*_{ch} and K^*_{ne} Dalitz projections, whereas Dalitz plot populations for all $K\pi$ mass combinations should be symmetrical for G-parity eigenstates. In the light of this, the combinations chosen to be plotted against each other were the $K^0\pi^\pm$ and $K^\pm\pi^\mp$ combinations, since this procedure should increase the difference between background and resonant events (see appendix B for further details).

J^{PG}	L	Decay Mode
0^{-+}	S	$a_0(980)\pi$
0^{-+}	P	K^*K
1^{++}	P	$a_0(980)\pi$
1^{++}	S	K^*K
1^{++}	D	K^*K
1^{-+}	P	K^*K
1^{+-}	S	K^*K
2^{-+}	D	$a_0(980)\pi$
2^{-+}	P	K^*K
2^{++}	D	K^*K

Table 6.4: The total set of waves used in the Dalitz plot analysis.

The matrix elements used for the fit to the Dalitz plot projections were produced by the use of FOWL [63] which uses a Monte-Carlo routine to generate phase space distributions for three body events with a given centre of mass energy. It produces the four-momenta for $K^0_S K^{\pm}\pi^{\mp}$ events, together with a weight dependent upon the position in phase space. These values are then used as input to the code which uses the Zemach formalism to generate the phase space distributions for various combinations of J^{PG}. The full set of waves generated are shown in table 6.4. The integral of each wave over the total range of phase space was calculated, over the range 1.2 GeV/c^2 to 1.76 GeV/c^2 in steps of 0.01 GeV/c^2. The waves were then weighted by the FOWL weight. The waves were normalized to each other according to the relation

$$\mathrm{Norm}(wave) = \frac{\sum \mathrm{WT(FOWL)}|\mathcal{M}(wave)|^2}{\sum \mathrm{WT(FOWL)}}.$$

Waves having the same spin parity assignment can interfere in a Dalitz plot. When a fit is performed, the negative log likelihood is calculated for a particular normalised wave for each event, and the sum of the Log likelihoods for a particular wave is calculated (see Appendix C for details of the Log Likelihood Method). This is minimised for each wave using MINUIT [64] to produce the percentage of each wave required to best describe the data. This method is considered superior to a χ^2

analysis since the likelihood method calculates the probability on an event by event basis. In order to implement a χ^2 measurement, the Dalitz plot has to be considered in bins. The choice of bin size affects the χ^2 value that will be determined for each wave.

6.5 Spin analysis of the $f_1(1285)$ meson

The $f_1(1285)$ region was selected from $K^0_S K^\pm \pi^\mp$ events by requiring that

$$1.25 < \text{Mass}\ (K^0_S K^\pm \pi^\mp\ ) < 1.32\ \text{GeV/c}^2.$$

The Dalitz plot for this mass region is shown in figure 6.2, where there are 407 events. This mass region is the easiest to fit since it is below the $K^*\ \overline{K}$ threshold

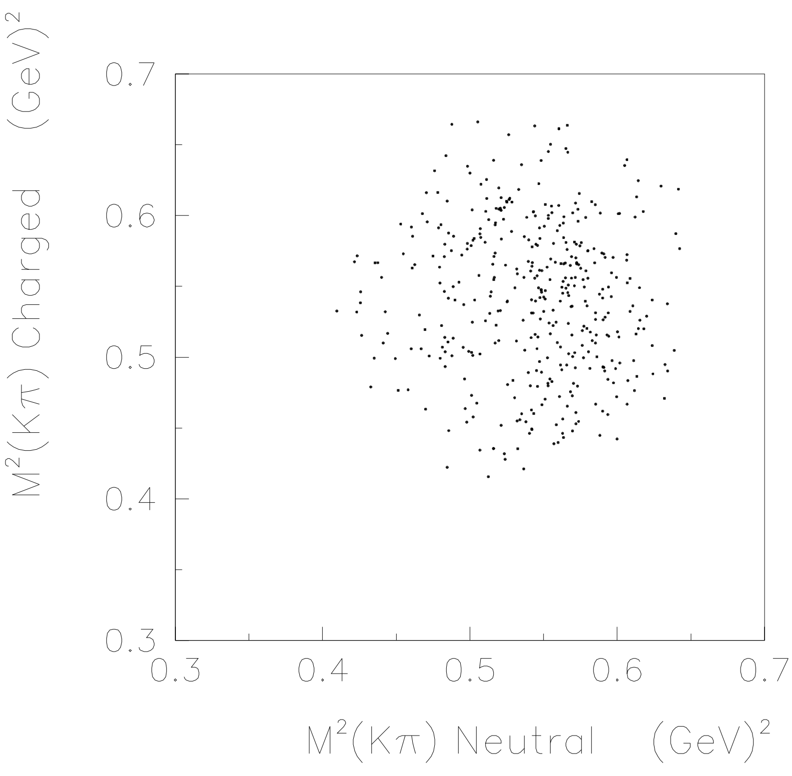

Figure 6.2: Dalitz plot for the $K^0_S K^\pm \pi^\mp$ mass spectrum in the region 1.25-1.32 GeV/c^2.

(around 1380 MeV) and so the only intermediate resonance required is the $a_0(980)$. Hence, the only waves that were possible in the $f_1(1285)$ mass range were:

0^{-+}S

1^{++}P

2^{-+}D

The Monte Carlo Dalitz plots for the three available waves that the $f_1(1285)$ can decay to are shown in figure 6.3.

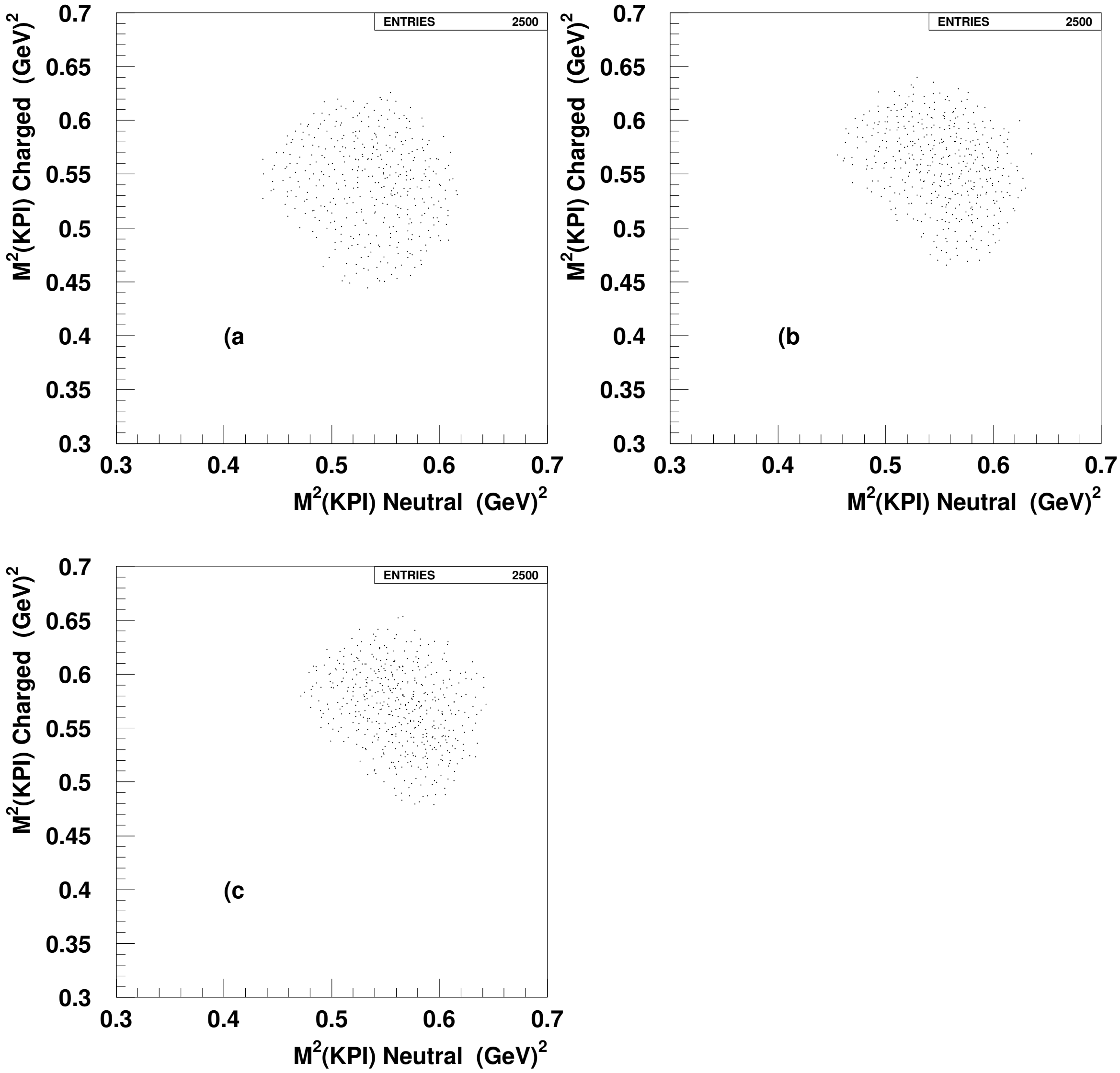

Figure 6.3: The a) 0^{-+}S b) 1^{++}P and c) 2^{-+}D Monte Carlo Dalitz plots for the 1.25 - 1.32 GeV/c^2 mass region.

These waves were fitted to the Dalitz plot projections individually, and the negative log likelihood values obtained for these three waves is shown in table 6.5. The χ^2 per degree of freedom for each of the wave fits was also calculated for comparison

J^{PG}	ln(lik)	χ^2/ndf	% wave
0^{-+}S	97.7	2.83	96.6
1^{++}P	114.6	2.26	84.4
2^{-+}D	106.1	3.09	66.5

Table 6.5: The results of individual wave fits to the $f_1(1285)$ region.

from the Dalitz plot by splitting the Dalitz plot into 100 bins and comparing the number of events in each bin with the number expected for each wave hypothesis. These are also tabulated to complement the log likelihood values. The 1^{++}P wave was the most probable single wave having 84.4 ± 6.3 %. The $f_1(1285)$ region was also fitted using the 0^{-+} and the 2^{-+} waves in conjunction with the 1^{++} wave, but this produced no significant improvement in the log likelihood value. The Dalitz projections for the $f_1(1285)$ are shown in fig 6.4 and the fitted curves are for 84.4% 1^{++}P wave, with 15.6% background.

6.6 Spin analysis of the $f_1(1420)$ meson

The $f_1(1420)$ region of the $K^0_S K^\pm \pi^\mp$ spectrum used in the spin analysis was defined to be

$$1.33 < \text{Mass } (K^0_S K^\pm \pi^\mp) < 1.69 \text{ GeV/c}^2.$$

The Dalitz plot for the $f_1(1420)$ mass region is shown in figure 6.5 where there are 1098 entries. Bands at the K^* mass can be seen. The use of side band subtraction to try to reduce background in the Dalitz plot has been investigated, and ruled out. Since the shape of the Dalitz plot changes with mass, then the distribution for masses on either side of the $f_1(1420)$ mass would have a different shape, and subtraction would not produce any meaningful reduction in background.

Monte Carlo Dalitz plots for the mass region defined by the $f_1(1420)$ are shown in fig 6.6 for the 1^{++}S, 1^{++}D, 1^{-+}P and 1^{+-}S waves, which all decay *via* the $K^*\overline{K}$ intermediate step. The Monte Carlo distributions for the other waves considered in the analysis are shown in figure 6.7.

The $f_1(1420)$ mass region was fitted in nine bins of width 40 MeV. The data was first fitted with single waves of J^{PG} values as shown in table 6.4. In the case of the

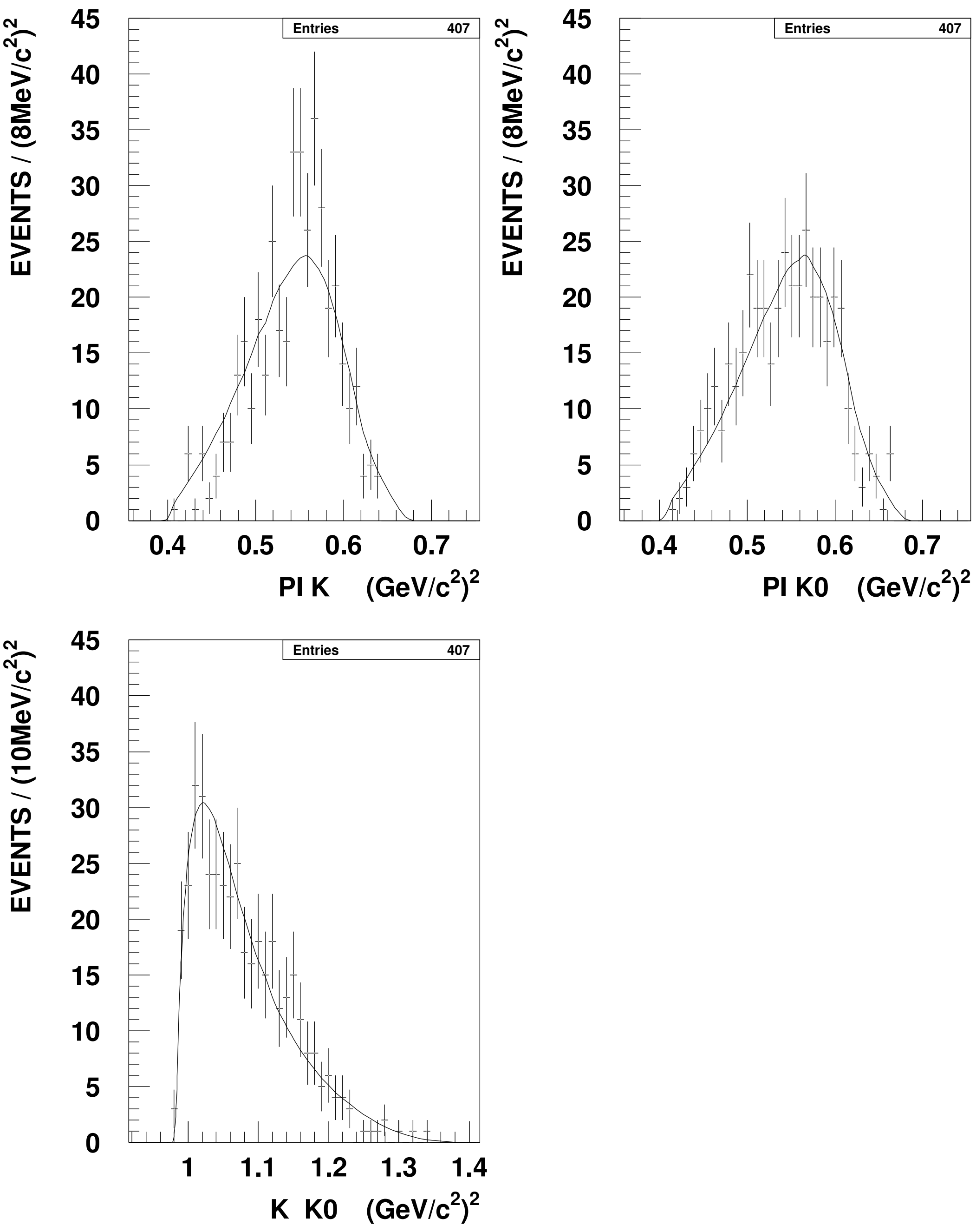

Figure 6.4: Dalitz plot projections for the $f_1(1285)$ mass region of the $K_S^0 K^\pm \pi^\mp$ spectrum, with fit as described in the text.

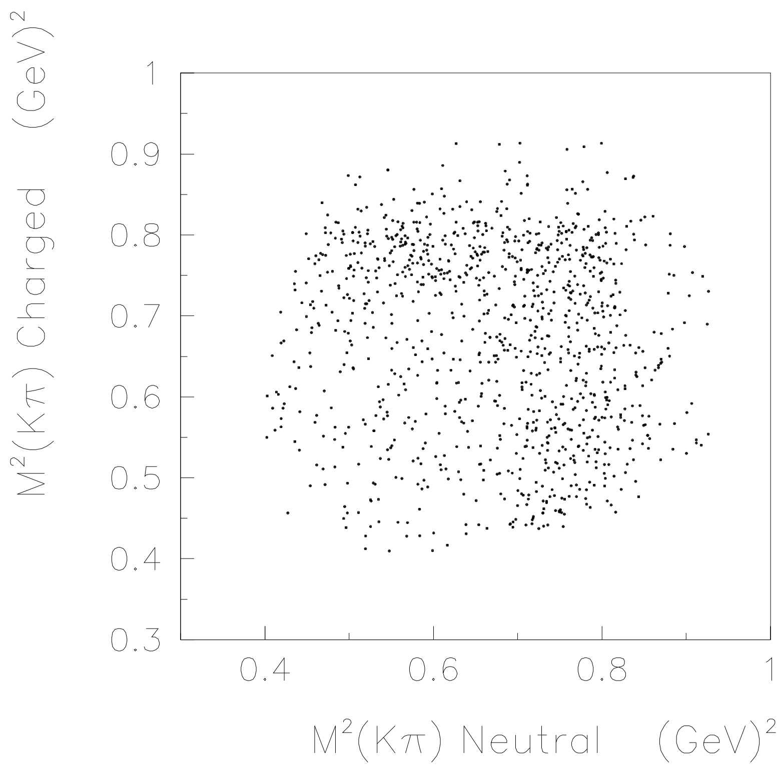

Figure 6.5: Dalitz plot for the $K^0_S K^{\pm}\pi^{\mp}$ mass spectrum in the region 1.37-1.49 GeV/c^2.

$f_1(1420)$, the decay can take place *via* $a_0(980)$ or $K^*\overline{K}$ decay and so the full set of waves may be considered in the analysis. The results of individual wave fits are presented in table 6.6, together with the calculated χ^2 and log likelihood for each wave.

The log likelihood distribution and the fit obtained to the data for the 1^{++}S wave are shown in figure 6.8

Clearly, the 1^{++}S wave is the one that best describes the $f_1(1420)$, with 61.1 $\pm$ 4.1 % wave. However, there may be possible contributions from other waves in conjunction with it. Hence, a two wave spin analysis was carried out, using the 1^{++}S wave together with one other wave, for all other waves available. In addition, two wave analyses were carried out for each of the waves with one other for all available combinations. There was only one combination of two waves that produced any significant increase in the log likelihood in the $f_1(1420)$ region, the 0^{-+}P combined with the 1^{++}S waves. There appears to be no contribution from the 0^{-+}S wave. The wave fit and log likelihood distribution for the $f_1(1420)$ mass region for the 1^{++} 0^{-+}P combination is shown in figure 6.9.

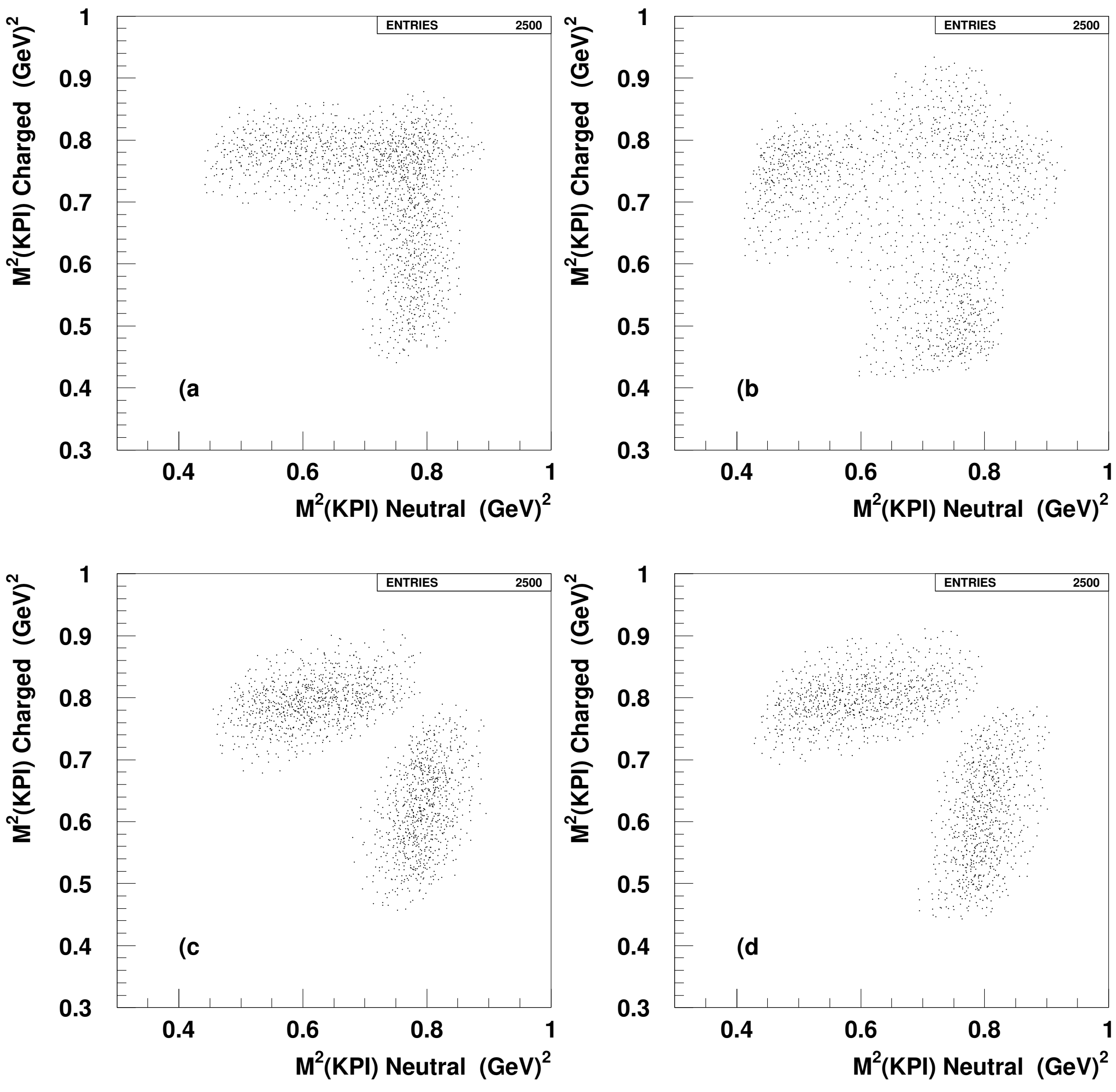

Figure 6.6: The a) 1^{++}S b) 1^{++}D c) 1^{-+}P and d)1^{+-}S Dalitz plots for the $f_1(1420)$ mass region.

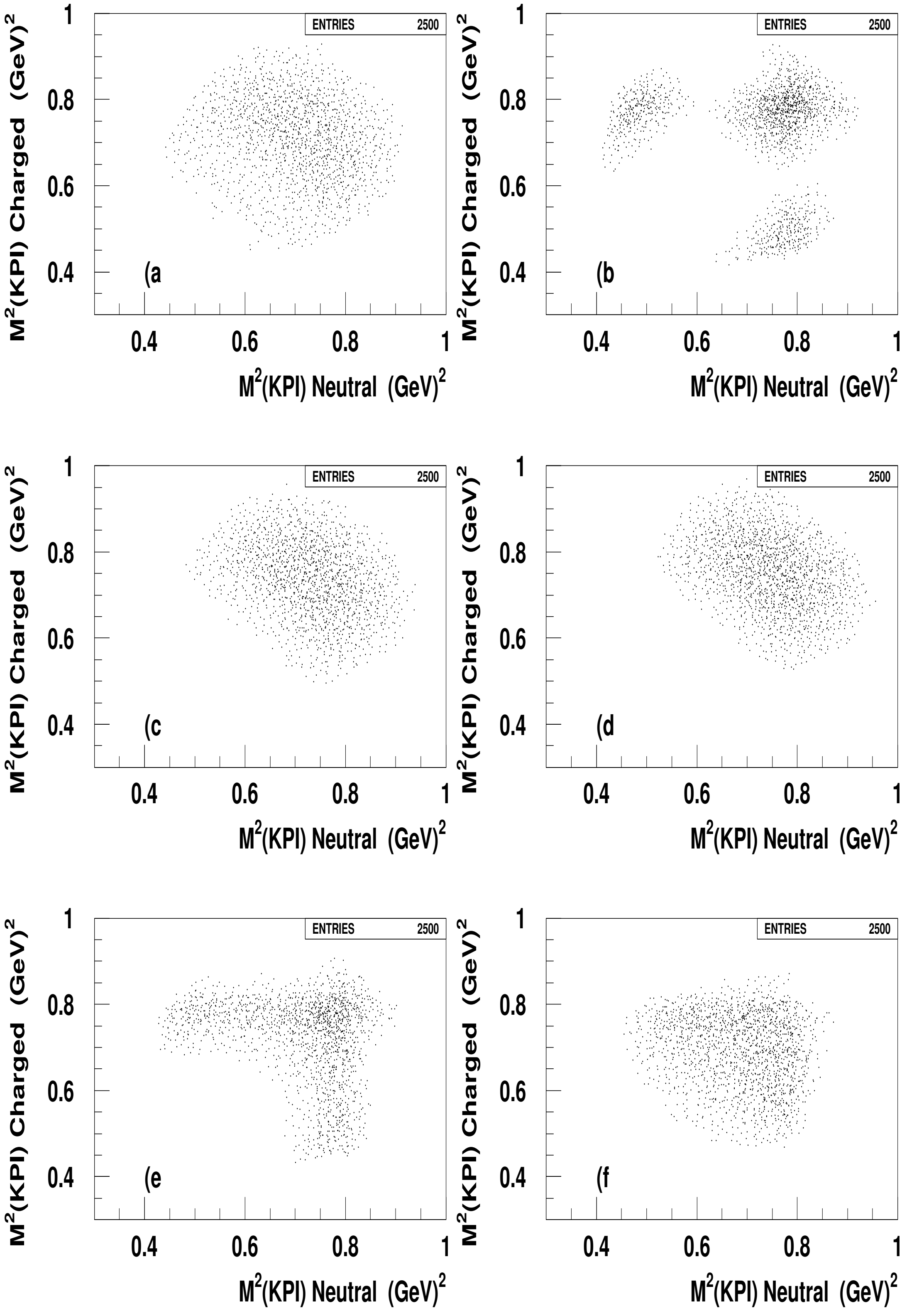

Figure 6.7: Monte Carlo Dalitz plots for a) 0^{-+}S, b) 0^{-+}P, c) 1^{++}P, d) 2^{-+}D, e) 2^{-+}P and f) 2^{++}D waves considered in the $f_1(1420)$ spin analysis.

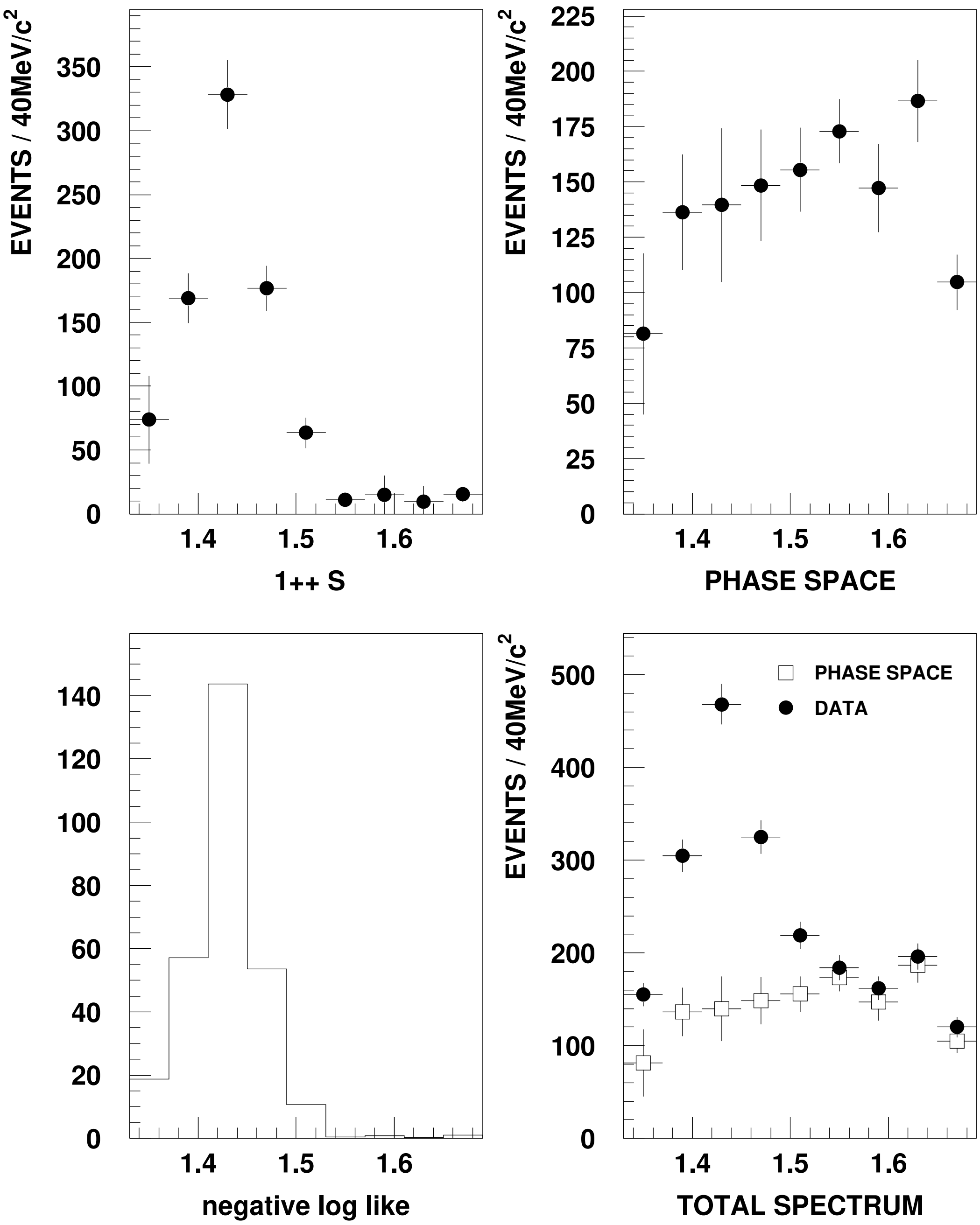

Figure 6.8: Log likelihood and wave fit to the $f_1(1420)$ mass region of the $K_S^0 K^{\pm}\pi^{\mp}$ spectrum for the 1^{++}S wave.

J^{PG}	Ln(likelihood) first 5 bins	Σ ln(lik)	χ^2/ndf	% wave
0^{-+}S	13.5, 45.5, 80.6, 11.7, 0.0	151.3	4.93	59.4
0^{-+}P	4.8, 17.3, 104.9, 31.6, 2.7	161.3	5.84	34.3
1^{++}P	12.6 ,40.8, 77.4, 10.5, 0.0	141.3	5.67	40.7
1^{++}S	18.8, 57.1, 143.6, 53.5, 10.7	283.7	1.63	61.6
1^{++}D	2.8, 13.3, 80.0, 18.4, 0.8	115.3	5.89	50.9
1^{-+}P	8.8, 32.1, 34.5, 17.1, 5.4	97.7	4.32	32.4
1^{+-}S	12.9, 42.1, 66.2, 23.8, 7.	152.8	4.11	44.5
2^{-+}D	11.1, 34.7, 72.1, 9.2, 0.0	127.1	6.77	31.8
2^{-+}P	8.6, 42.3, 136.7, 54.8, 10.6	253.0	2.70	67.3
2^{++}D	0.0, 0.7, 5.4, 16.4, 5.7	28.2	6.57	21.2

Table 6.6: The results of individual wave fits to the $f_1(1420)$ region.

J^{PG}	Ln(likelihood) first 5 bins	Σ ln(lik)	χ^2/ndf	% wave 1^{++}S, other
1^{++}S 0^{-+}P	18.8, 57.1, 146.3, 53.5, 10.7	286.4	1.76	58.4 $\pm$ 4.3, 3.5 $\pm$ 2.0
1^{++}S 0^{-+}S	18.8, 57.1, 143.6, 53.5, 10.7	283.7	1.78	61.4 $\pm$ 4.4, 0.5 $\pm$ 0.3

Table 6.7: The two wave fits to the $f_1(1420)$ region for the 1^{++}S 0^{-+}P and 1^{++}S 0^{-+}S combinations, the former showing a significant increase in log likelihood from single 1^{++} wave.

The statistics for the two wave fits for the 1^{++}S wave and both of the allowed 0^{-+} waves is shown in table 6.7. The contributions made to the overall $f_1(1420)$ signal can be gauged by considering the plots of figure 6.10, where the fits for the 1^{++}S wave a) and the summed 0^{-+} waves b) are shown together with the superimposed $f_1(1420)$ fit of the $K^0_S K^{\pm}\pi^{\mp}$ mass spectrum. As can be seen, the 1^{++}S data follows closely the fitted Breit-Wigner representation of the $f_1(1420)$, whereas the 0^{-+} waves have a very small contribution.

The significance of a change in log likelihood can be gauged by the following relation [65]:

$$\sigma = \sqrt{2.\Delta\mathcal{L}}$$

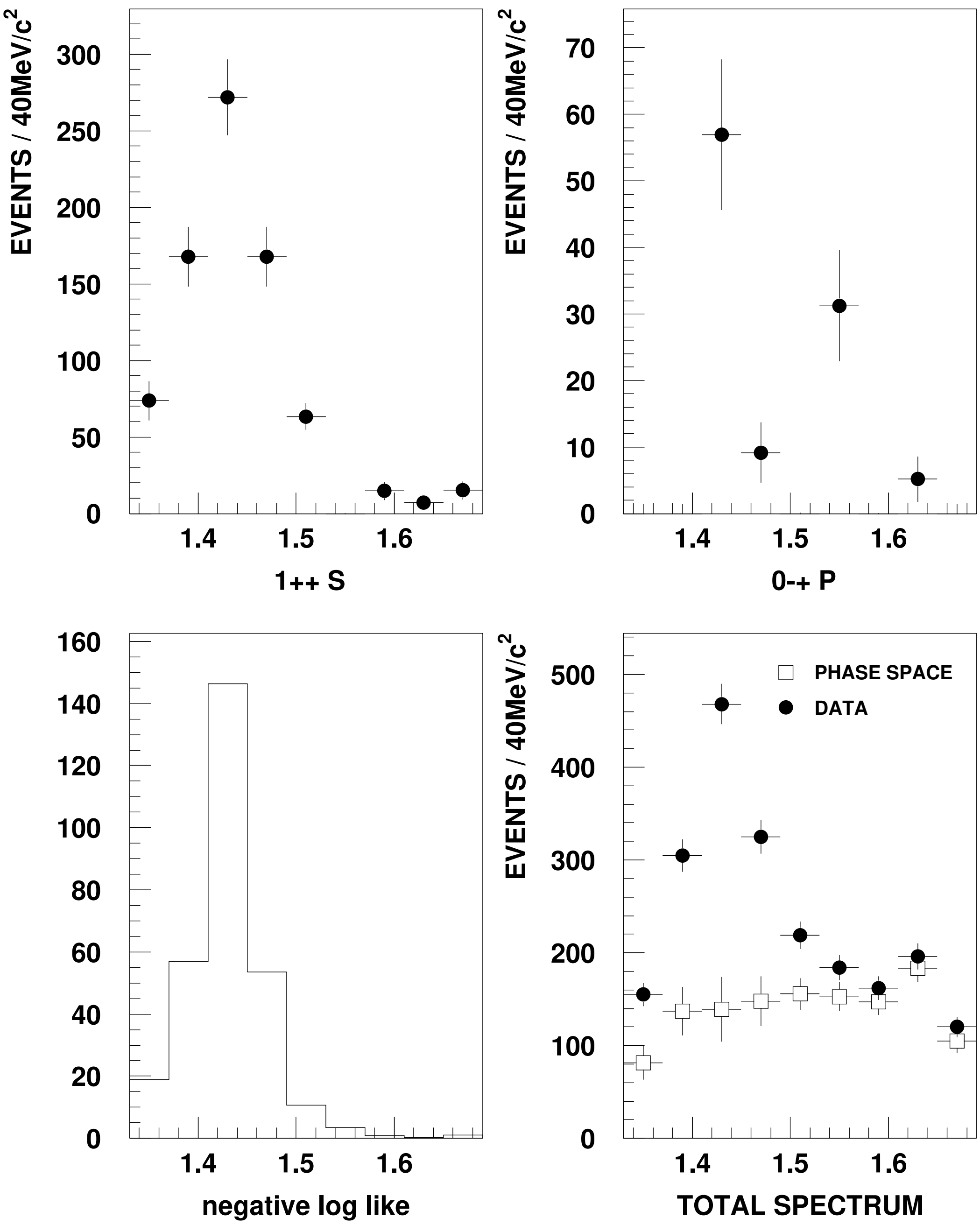

Figure 6.9: Log likelihood and wave fit to the $f_1(1420)$ mass region for the 1^{++}S and 0^{-+}P waves.

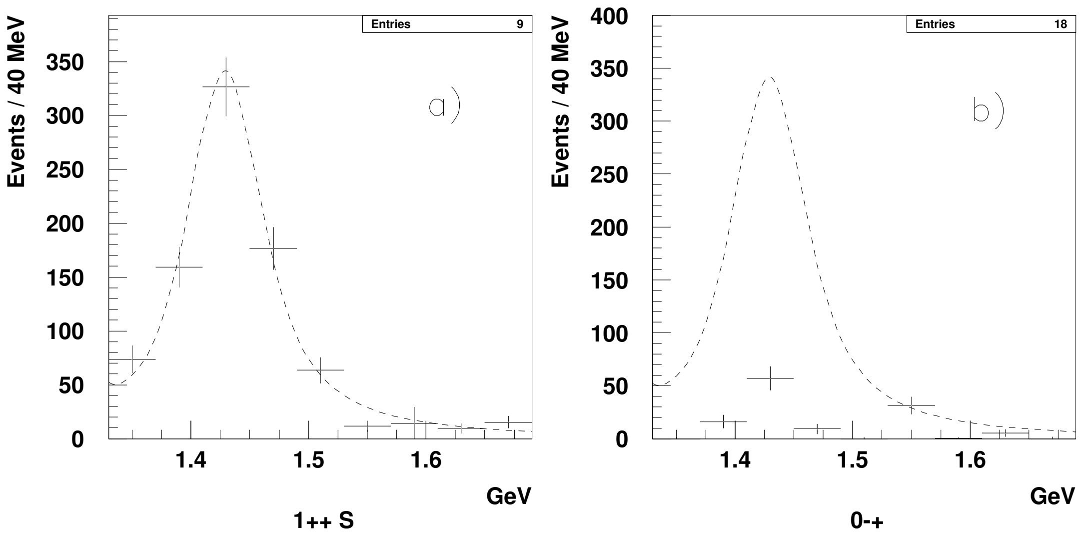

Figure 6.10: The a) 1^{++}S wave and b) 0^{-+} wave data from a two wave fit to the $f_1(1420)$ mass region. The superimposed curve in each plot is the fit to the $f_1(1420)$ region of the $K_S^0K^{\pm}\pi^{\mp}$ mass spectrum as described in chapter 5.

where $\Delta\mathcal{L}$ is the difference in log likelihood between two different hypotheses. For the two wave combination under consideration, this gives :

$$\sigma_{0^{-+}P} = 2.32$$

This means that the 0^{-+}P state is just at the significance level. As has been mentioned in chapter 3, the observation of a 0^{-+} state in the $f_1(1420)$ mass region has been documented by several experiments. It was considered that the presence of this wave deserved further consideration. This wave was included in the Dalitz plot analysis discussed subsequently.

6.7 Contributions to the Dalitz projections

6.7.1 Mis-assignment of particle identity

If one considers the Ehrlich mass plot for the $K_S^0K^{\pm}\pi^{\mp}$ channel in chapter 5, then it is apparent that there is a considerable ambiguity in particle assignment for the $K^{\pm}$ and the $\pi^{\mp}$ tracks, since there is no clearly defined peak in the distribution at the kaon mass squared. Because of this ambiguity, anomalies may appear in the Dalitz plot and its projections for the $K^0_S K^\pm \pi^\mp$ channel.

The proportion of ambiguous events can be determined by considering the numbers of various flags that fall within the $f_1(1420)$ mass region i.e. in the region defined by:

$$1.37 < \text{Mass}\ (K^0_S K^\pm \pi^\mp) < 1.49\ \text{GeV/c}^2.$$

These proportions were found to be:

- Number of unambiguous events in $f_1(1420)$ region = 635
- Number of ambiguous events plotted twice in $f_1(1420)$ region = 123
- Number of ambiguous events plotted once in $f_1(1420)$ region = 218

So the proportion of ambiguous events is around the 13% level, requiring that these ambiguity effect should be taken into account when attempting to perform a fit to the Dalitz projections for the $f_1(1420)$.

6.7.2 Contribution from the 0^{-+} wave

As well as taking into account the mis-assigned events, the 0^{-+} wave must also be considered in any Dalitz plot analysis since it appears to be significant (the two wave fit indicates that it represents around 3.5% of the Dalitz plot). The effect that this wave has on the Dalitz plot must be ascertained.

6.8 Evaluation of relative contributions

In order to determine the percentage contribution of each of the above factors, Monte Carlo Dalitz plots were produced for the 1^{++}S and 0^{-+} waves, and for the background. The Dalitz projections for these distributions are shown in figure 6.11 and figure 6.12.

Further, in order to take account of the mis-assignment of events, 'flipped' events were produced where the $K^\pm$ and the $\pi^\mp$ of generated events had their direction cosines swapped, effectively reproducing a mis-assignment. The Dalitz plot projections obtained for the flipped events are shown in figure 6.13.

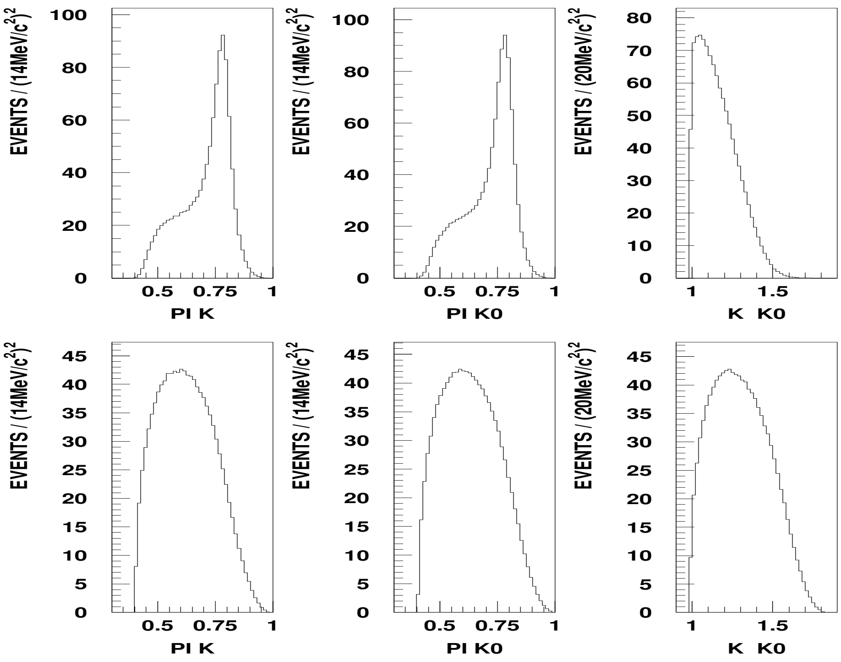

Figure 6.11: Dalitz plot projections for the $f_1(1420)$ mass region of the $K_S^0 K^{\pm}\pi^{\mp}$ spectrum, for the 1^{++}S wave. The bottom three plots are the background for the three projections.

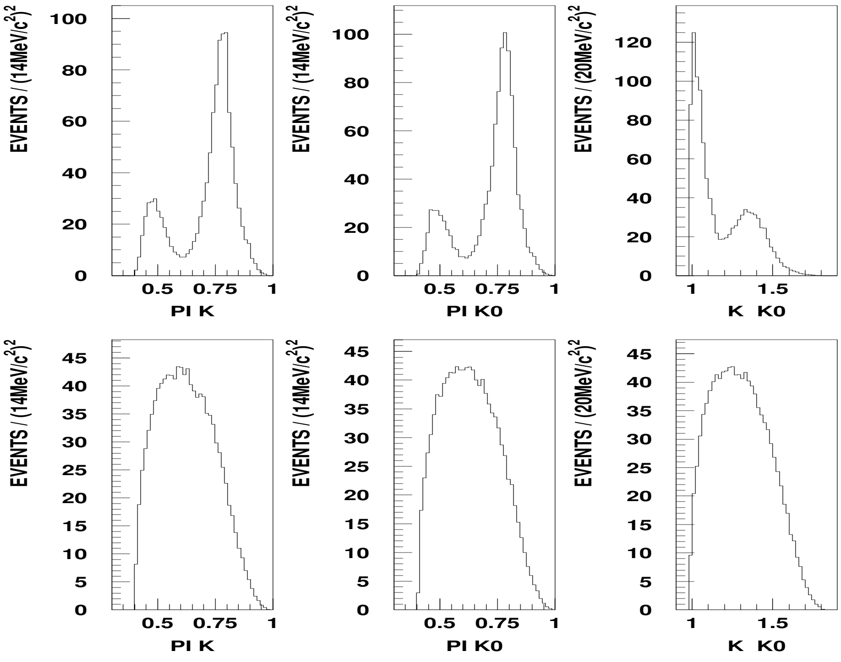

Figure 6.12: Dalitz plot projections for the $f_1(1420)$ mass region of the $K_S^0 K^{\pm}\pi^{\mp}$ spectrum, for the 0^{-+}P wave.

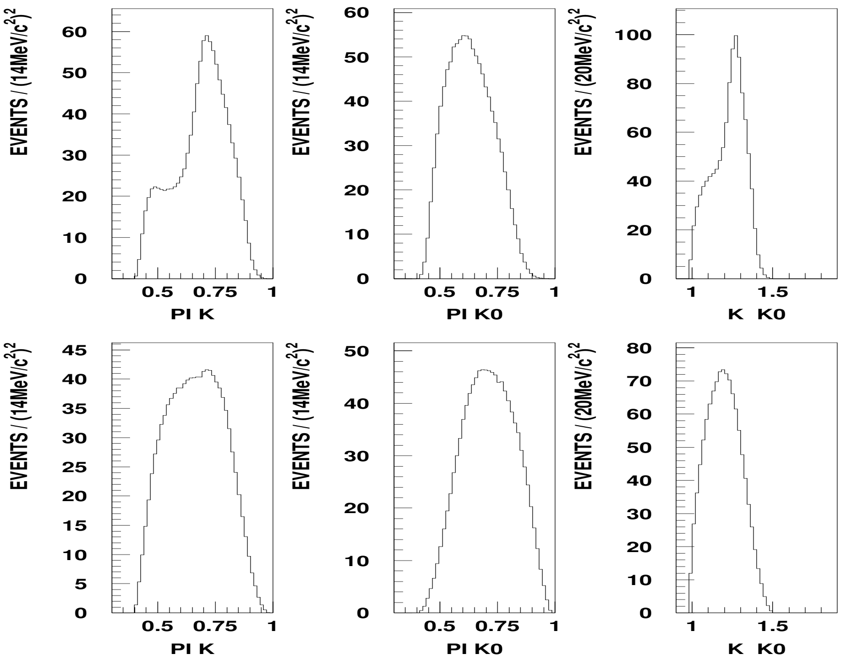

Figure 6.13: Dalitz plot projections for the $f_1(1420)$ mass region of the $K_S^0 K^\pm \pi^\mp$ spectrum, for 'flipped' events, as described in text.

These contributions were combined in the following way:

$$f = \alpha(1^{++}S) \ + \ \beta(flipped\, 1^{++}S) \ + \ \gamma(bckgnd) \ + \ \delta(flipped\, bckgnd) \ + \ \epsilon(0^{-+}P).$$

Combinations of all these possible contributions to the Dalitz plot were combined by varying the proportion factors subject to the following constraints:

- Proportion of wave and flipped wave events = 61%
- Proportion of background and flipped background events = 39%
- Proportion of flipped events (background and wave) = 13%

For every iteration, the χ^2/ndf was evaluated for the three projections ($\pi K_{charged}$, $\pi K_{neutral}$ and KK^0) by calculating the difference between the data in the projection and f. In this manner, the optimum combination was found to be

- Proportion of 1^{++}S wave events, $\alpha = 53$ %
- Proportion of flipped 1^{++}S events, $\beta = 9$ %

- Proportion of background events, $\gamma = 34$ %
- Proportion of flipped background events, $\delta = 4$ %
- Proportion of 0^{-+} wave events, $\epsilon = 0$ %

with a χ^2 per degree of freedom of 1.32. For every iteration, the addition of the 0^{-+}P wave produced no significant decrease in χ^2. The conclusion that can be drawn, therefore, is that the $f_1(1420)$ can be well described using only the $J^{PG} = 1^{++}$S wave projections and its momentum mis-assigned projections. The fit to the Dalitz plot projections in the $f_1(1420)$ mass window for the best combination of wave and flipped wave is shown in figure 6.14

6.9 Comparison between $K^0_S K^{\pm}\pi^{\mp}$ centrally produced events at 85, 300 and 450 GeV/c

The relative proportions of $f_1(1420)$ and $f_1(1285)$ were evaluated for the WA91 data at 450 GeV/c. This was then compared to the previous central production data from WA76.

To allow a meaningful comparison to be made between the two sets of WA76 data and the WA91 data taken at 450 GeV/c, a cut was made on the Feynman x region of the central $K^0_S K^{\pm}\pi^{\mp}$ system, in order to select a region of good acceptance for the three experiments. The cut used was $|x_F| \leq 0.15$. The number of events present in both meson mass windows for each data set was determined from fits to the $K^0_S K^{\pm}\pi^{\mp}$ mass spectrum in the x_F region selected. The ratio (R) of the number of events in the $f_1(1285)$ to the $f_1(1420)$ for the three experiments are listed in table 6.8. The data obtained at 450 GeV/c is consistent with the data at 300 GeV/c. The $\sqrt{s}$ value for 450 GeV/c incident protons is 29.1 and for 300 GeV/c it is 23.8 whereas for 85 GeV/c the figure is much smaller, at 12.7. This explains why the WA91 data is consistent with the WA76 300 GeV/c data, yet different from the 85 GeV/c data. The change in the ratio of $f_1(1285)$ to $f_1(1420)$ with increasing momentum suggests that the energy dependence of $f_1(1285)$ production is different to that of the $f_1(1420)$.

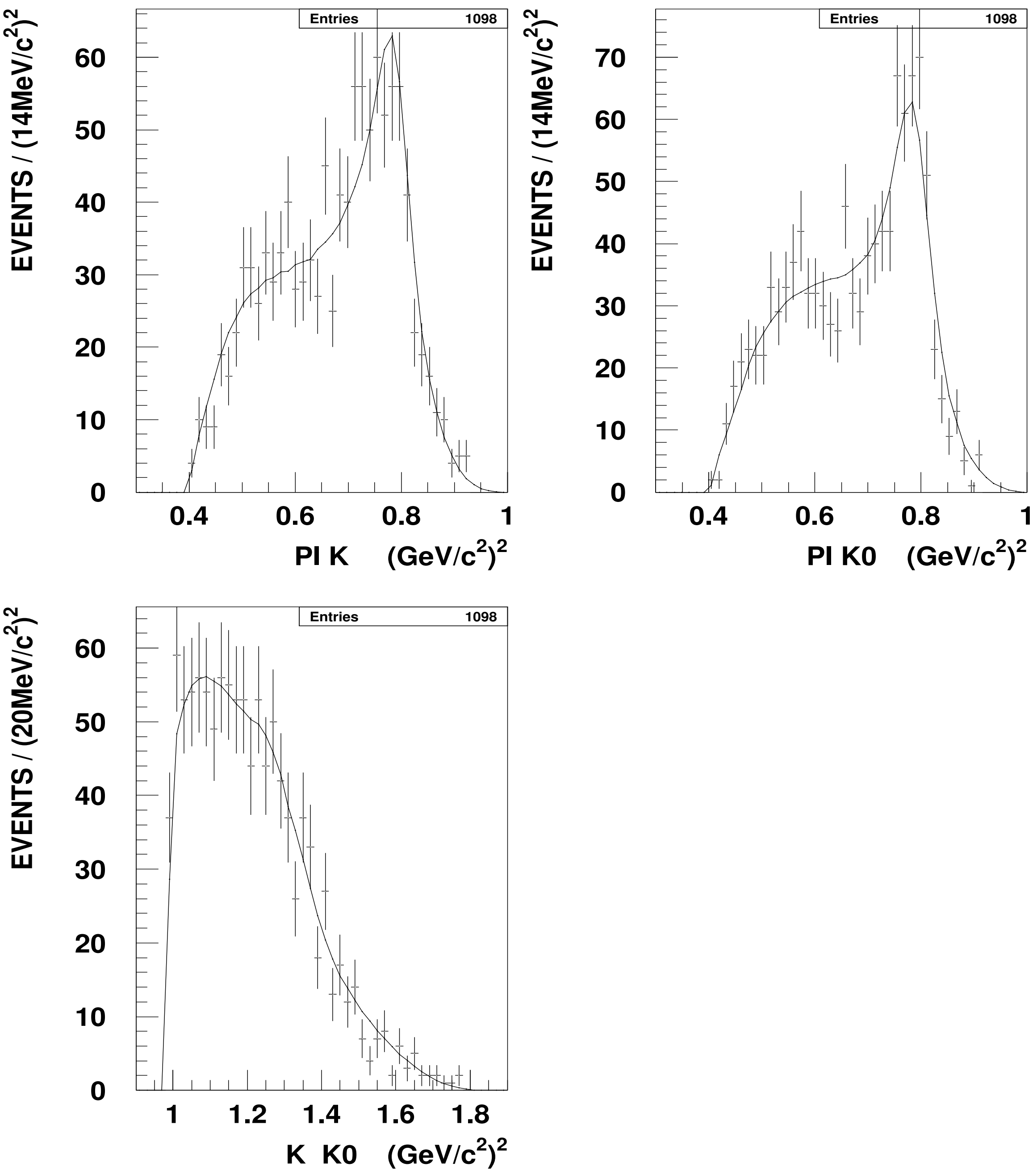

Figure 6.14: Dalitz plot projections for the $f_1(1420)$ mass region of the $K_S^0 K^{\pm}\pi^{\mp}$ spectrum, with fit as described in the text.

Incident momentum GeV/c	Ratio
85	0.58 ± 0.07
300	0.34 ± 0.03
450	0.34 ± 0.05

Table 6.8: Ratio of $f_1(1285)$ to $f_1(1420)$ for the 85, 300 and 450 GeV/c centrally produced $K^0_S K^\pm \pi^\mp$ system.

6.10 Discussion of results

The Zemach method of analysis used to study the $K^0_S K^\pm \pi^\mp$ channel has the same type of formalism as that used by the earlier WA76 experiment. It is worthwhile at this point to mention different experiments that have argued for a different spin parity assignment than that presented by previous WA76 results, where the WA76 results were consistent with the spin values presented in this thesis. In particular, the Brookhaven AGS-771 experiment studied the reaction $\pi^- p \rightarrow (K^\pm \pi^\mp K^0_L)n$ [68]. They argued that the data could be interpreted by combining 0^{-+} $a_0(980)$, 0^{-+} $K^*\overline{K}$ and 1^{+-} $K^*\overline{K}$ waves, leaving a smooth 1^{++} $K^*\overline{K}$ contribution. Their conclusions were that the E meson had the quantum numbers $J^{PC} = 0^{-+}$, decaying mostly *via* $a_0(980)\pi$. The authors have, however, never shown an enhancement in the threshold of the $K\overline{K}$ Dalitz projection, which is characteristic of the $a_0(980)$. Also, they did not demonstrate the solution that incoherent $K^*_{charged}$ together with 1^{++} wave did not fit their data.

An additional difference from the earlier WA76 spin analysis came from authors who had performed a spin analysis on the Dalitz plot projections of previously published WA76 data [69]. They argued that the state that was being observed by the experiment was in fact a $J^{PC} = 1^{+-}$ one, and that the data could be interpreted best as a combination of $J^{PC} = 1^{+-}$ and 0^{-+} waves. However, the comparisons they made were performed at a fixed mass of the $K^0_S K^\pm \pi^\mp$ system, and this meant that the Breit-Wigner shape of the resonance was not taken into account. In addition, when fitting waves to the Dalitz plot projections, then any two dimensional correlations are not taken into account. The WA76 experiment carried out a spin analysis of the $K^0_S K^\pm \pi^\mp$ spectrum for the combined 85 and 300 GeV/c data sample

[61], where this alternative explanation was ruled out.

6.11 Conclusions

In the WA91 $K^0_S K^\pm \pi^\mp$ channel, clear $f_1(1285)$ and $f_1(1420)$ signals have been observed. Their masses and widths have been evaluated and found to be :

$$
\begin{aligned}
M_{f(1285)} &= 1281 \pm 2 \text{ MeV/c}^2 \\
\Gamma_{f(1285)} &= 19 \pm 5 \text{ MeV/c}^2 \\
M_{f(1420)} &= 1426 \pm 2 \text{ MeV/c}^2 \\
\Gamma_{f(1420)} &= 61 \pm 7 \text{ MeV/c}^2
\end{aligned}
$$

The ratio of $f_1(1285)$ to $f_1(1420)$ at 450 GeV/c is found to be consistent with that for $K^0_S K^\pm \pi^\mp$ events produced at 300 GeV/c, yet different from 85 GeV/c data, implying a different energy dependence for the two mesons.

A spin parity analysis of the $K^0_S K^\pm \pi^\mp$ channel using the Zemach tensor formalism demonstrates that both the $f_1(1285)$ and the $f_1(1420)$ have quantum numbers $J^{PG} = 1^{++}$. The $f_1(1285)$ is found to decay *via* the $a_0(980)\pi$ decay mode whereas the $f_1(1420)$ decays *via* the $K^*\overline{K}$ intermediate state only. The $f_1(1420)$ decay is described well by 1^{++} wave, and no 0^{-+} wave is required. Since the $f_1(1420)$ is also observed in the $K^0_S K^0_S \pi^0$ central production channel [61], this determines the C parity of the $f_1(1420)$ to be positive. From the relation C = $(-1)^I$G, the isospin is determined to be zero. Hence the quantum numbers of the $f_1(1420)$ are found to be $I^G(J^{PC}) = 0^+(1^{++})$.

Chapter 7

Branching ratio calculation for the $f_1(1285)$ in the $K^0_S K^\pm \pi^\mp$ and $\pi^+\pi^-\pi^+\pi^-$ channels

7.1 Introduction

The $f_1(1285)$ is identified as being the $^3P_1$ member of the $J^{PC} = 1^{++}$ nonet, having $I^G = 0^+$. Its predominant decay mode is $f_1(1285) \rightarrow \eta\pi\pi$. It has been observed in the WA91 experiment in the $\eta\pi\pi$, 4π and $K^0_S K^\pm \pi^\mp$ channels. This chapter details how the branching ratio

$$\frac{f_1(1285) \rightarrow K\overline{K}\pi}{f_1(1285) \rightarrow 4\pi}$$

was determined from the $\pi^+\pi^-\pi^+\pi^-$ and $K^0_S K^\pm \pi^\mp$ channels in WA91.

7.2 Selection of the $\pi^+\pi^-\pi^+\pi^-$ channel in WA91

The reaction

$$pp \rightarrow p_f(\pi^+\pi^-\pi^+\pi^-)\ p_s$$

has been selected from WA91 events where there are six outgoing tracks by imposing the following cuts on the components of missing momentum:

$$|\text{missing p}_x| \ < \ 14.0 \text{ GeV/c}$$

$$|\text{missing p}_y| \; < \; 0.12 \text{ GeV/c}$$
$$|\text{missing p}_z| \; < \; 0.08 \text{ GeV/c}$$

The delta function, Δ, defined as:

$$\Delta \;=\; MM^2(p_f p_s) \;-\; M^2(\pi^+\pi^-\pi^+\pi^-)$$

was calculated for each event and used to select good $\pi^+\pi^-\pi^+\pi^-$ events by requiring

$$|\Delta| \; < 3.0 \text{ (GeV/c}^2)^2.$$

Events containing a fast Δ^{++} are removed by imposing the following condition:

$$m(p_f\pi^+) \; > 1.5 \text{ GeV/c}^2.$$

The mass spectrum obtained for the $\pi^+\pi^-\pi^+\pi^-$ channel is shown in fig 7.1. There

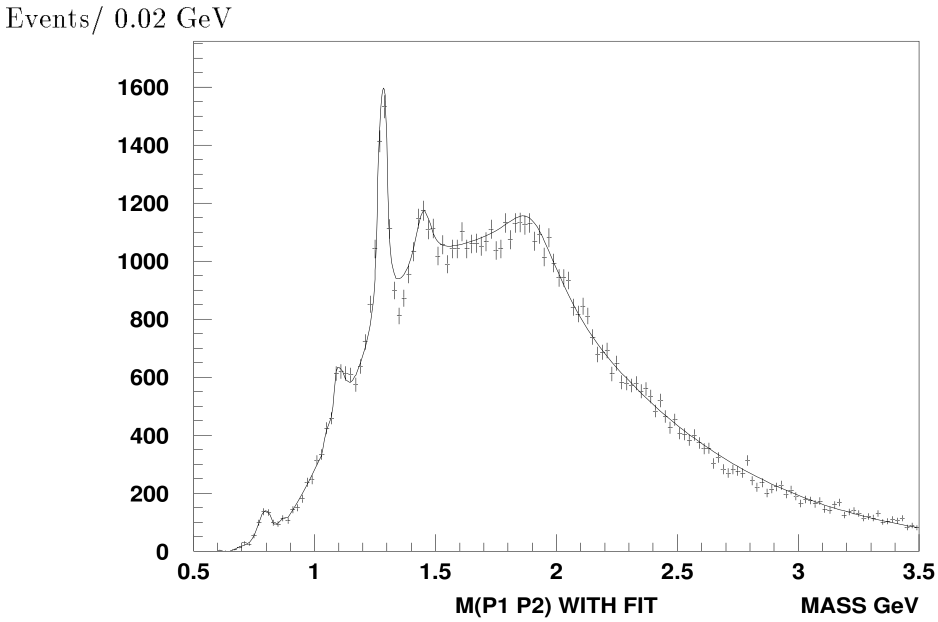

Figure 7.1: The $\pi^+\pi^-\pi^+\pi^-$ mass spectrum.

is a prominent peak at 1.28 GeV due to the presence of the $f_1(1285)$, and there are also enhancements at 1.45 and 1.9 GeV, the X(1450) and the X(1900). In addition, there are reflections from the $\eta\pi^+\pi^-$ decay of the η' and $f_1(1285)$ giving small enhancements in the spectrum in the 0.8 and 1.1 GeV regions, due to a slow π^0 from an η decay falling within the missing momenta cuts described above. The fit in fig. 7.1 used Breit-Wigners to describe the $f_1(1285)$, X(1450) and X(1900) and a background of the form $bckgnd(m) \ = \ a(m - m_{th})^b exp(-cm - dm^2)$ where m is the $\pi^+\pi^-\pi^+\pi^-$ mass and m_{th} is the $\pi^+\pi^-\pi^+\pi^-$ threshold mass. For the $f_1(1285)$, the fit produces the following values:

$$
\begin{aligned}
M_{f(1285)} &= 1280 \ \pm \ 2 \text{ MeV/c}^2 \\
\Gamma_{f(1285)} &= 40 \ \pm \ 6 \text{ MeV/c}^2.
\end{aligned}
$$

7.3 Correction factors due to unseen decay modes

In the $K\overline{K}\pi$ channel, assuming that the decay of the central system is via $a_0(980)$, then the possible decay modes are:

$$
\begin{gathered}
K^0\overline{K}^0\pi^0 \\
K^0K^\pm\pi^\mp \\
K^+K^-\pi^0.
\end{gathered}
$$

Taking into account the Clebsch Gordan coefficients for the three possibilities, the observed $K^0K^\pm\pi^\mp$ decays represent 2/3 of the total number of decays. In addition, $K^0_SK^\pm\pi^\mp$ is half of all $K^0K^\pm\pi^\mp$ decays. The reaction $K^0_S \rightarrow \pi^+\pi^-$ accounts for 68.6 % of all K^0_S decays.

Because of all these unseen decays, the number of observed events in the $K^0_SK^\pm\pi^\mp$ channel must be multiplied by a factor, $f_{K\overline{K}\pi}$, where

$$
f_{K\overline{K}\pi} = \frac{3}{2} \cdot 2 \cdot \frac{1}{0.686} \ = \ 4.37 \ \ .
$$

In the case of the $\pi^+\pi^-\pi^+\pi^-$ channel, if we assume that the $f_1(1285)$ decays *via* $\rho\pi\pi$, there are again three possible decay modes:

$$
\begin{gathered}
\rho^0\pi^+\pi^- \\
\rho^+\pi^-\pi^0 \\
\rho^-\pi^+\pi^0.
\end{gathered}
$$

In this case, all are equally likely, and so the correction factor to take into account unseen decays, $f_{\rho\pi\pi}$, is

$$
f_{\rho\pi\pi} = 3
$$

7.4 Selection of a compatible x_F region

In order to correctly determine the branching ratio for the two channels, events in the $f_1(1285)$ region for both channels must come from a compatible region of the Feynman x (x_F) distribution. The x_F distribution for the centrally produced $K^0_S K^\pm \pi^\mp$ and $\rho\pi\pi$ systems are shown in figure 7.2 and 7.3 respectively.

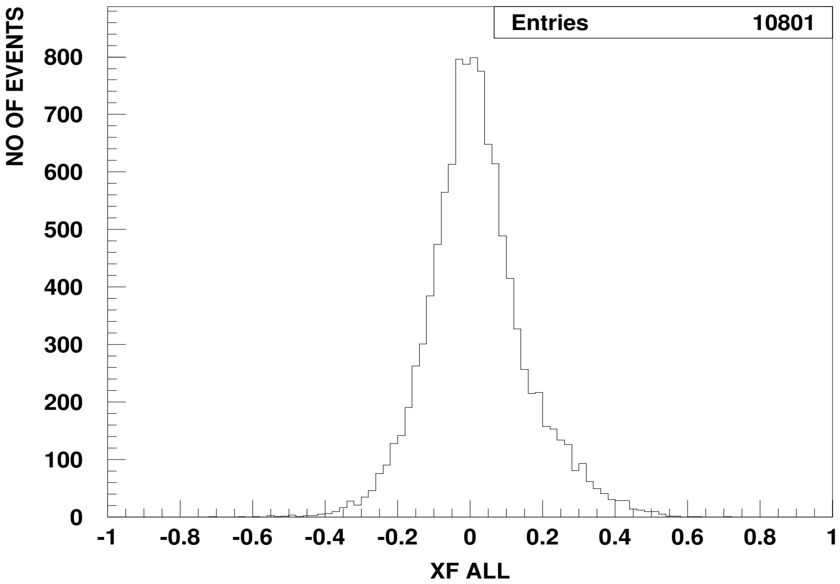

Figure 7.2: The x_F distribution for the central $K^0_S K^\pm \pi^\mp$ system.

Central events having the $f_1(1285)$ mass defined by

$$1.25 < \text{Mass } (X^0) < 1.32 \text{ GeV/c}^2.$$

were plotted for both channels. The distribution obtained for the $K^0_S K^\pm \pi^\mp$ channel is shown in figure 7.4. This is narrower than the distribution for the $\rho\pi\pi$ channel. A cut of $|x_F| < 0.15$ was decided upon since in this region the acceptance was reasonably uniform for central events. This cut allowed most of the events in the $f_1(1285)$ region of the $K^0_S K^\pm \pi^\mp$ x_F distribution to be considered. The cut also fell within the limits of the $\pi^+\pi^-\pi^+\pi^-$ central events in the $f_1(1285)$ window, where the acceptance was again reasonably flat. In this way, central events in the same kinematic region were selected for both channels.

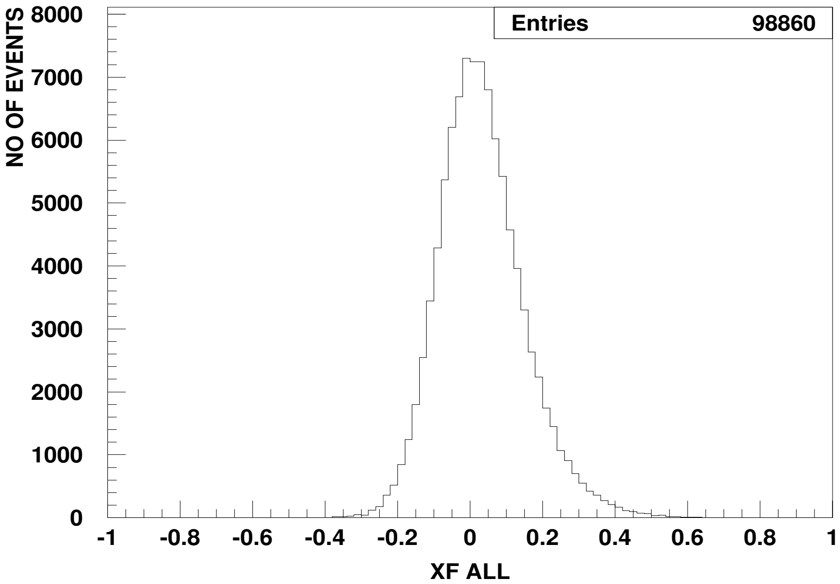

Figure 7.3: The x_F distribution for the central $\rho\pi\pi$ system.

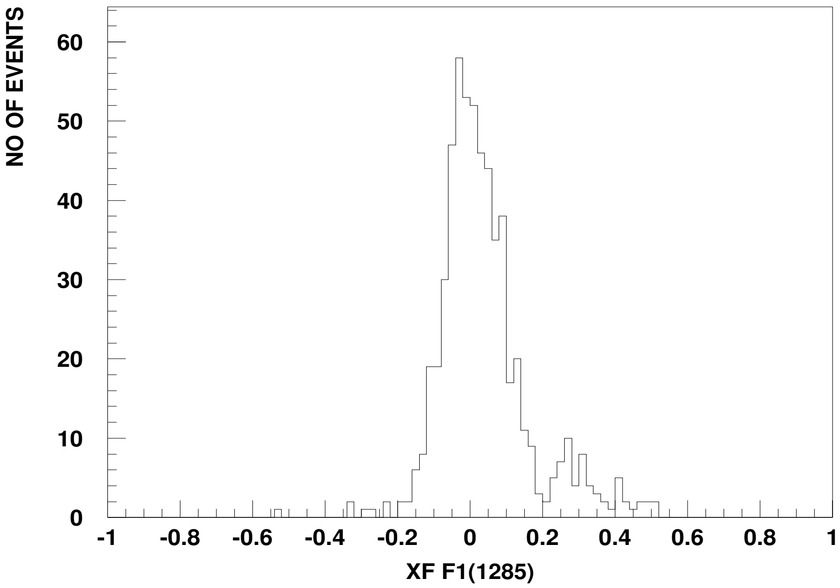

Figure 7.4: The x_F distribution for central $K_S^0 K^{\pm}\pi^{\mp}$ events within the $f_1(1285)$ mass window.

The mass spectra in the two channels was produced, having implemented the x_F cut. Both spectra were fitted in order to obtain the number of events in the $f_1(1285)$ region. In the $K^0_SK^\pm\pi^\mp$ channel, the number in the $f_1(1285)$ peak found by fitting the total spectrum, with a fit of the form described in chapter 6, is 338 $\pm$ 21. In the $\pi^+\pi^-\pi^+\pi^-$ channel there are a total of 2516 $\pm$ 86 events in the $f_1(1285)$ peak.

7.5 Acceptance corrections

The acceptances for both channels were calculated by using mixed events produced from real 2π events, and rotating them about the x-axis, and tracing tracks to see whether they were accepted. The acceptance as a function of mass of the central system is shown in fig 7.5. The acceptance for the $K^0_SK^\pm\pi^\mp$ channel has been shown in Chapter 5 fig 5.7. The acceptance in both channels decreases smoothly with increasing mass.

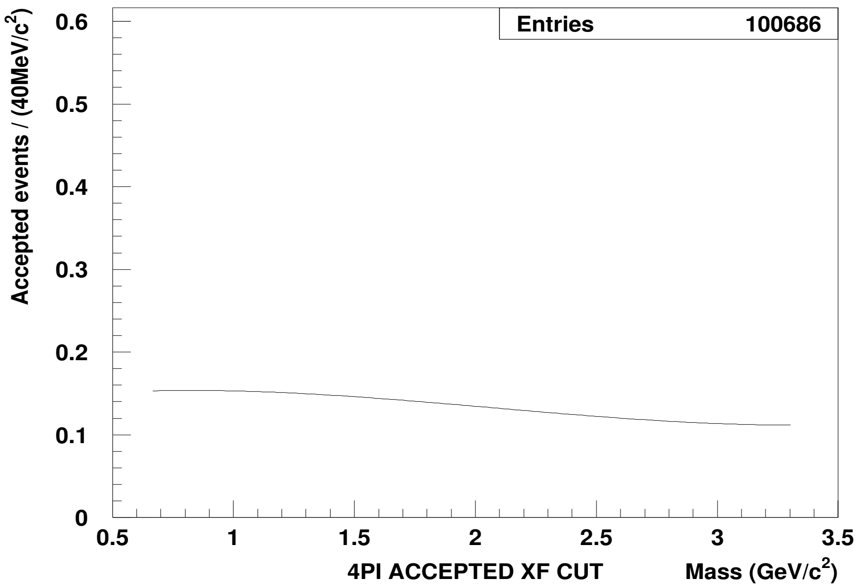

Figure 7.5: Geometrical acceptance as a function of $\rho\pi\pi$ effective mass.

7.6 Efficiency of the V^0 reconstruction code

One factor that has to be taken into account in the $K_S^0 K^\pm \pi^\mp$ channel is the efficiency for finding V^0 vertices. The number of true V^0's that are successfully reconstructed must be determined, and this number incorporated in the final evaluation of the branching ratio.

In order to calculate the efficiency of the V^0 program, code was written to simulate the decay of a central system to a $K^\pm$, $\pi^\mp$ and a K^0, smearing all tracks coming from the decay to take into account the experimental resolution of the WA91 experiment. These simulated events were read into the V^0 program to determine how many generated vertices were successfully reconstructed.

7.6.1 Generation of $K_S^0 K^\pm \pi^\mp$ Events

In order to generate simulated K^0 events, mixed $\pi\pi$ events from WA91 were used. Combinations of two π tracks that had a mass in the range 1.1-1.6 GeV were considered to form the central X^0 system. This central system was then made to produce a $K^\pm$, $\pi^\mp$ and K^0 three particle system.

A primary vertex was generated between -180 and -120 cm in x of the Omega system. A K_S^0 was then made to decay in the centre of mass to two pions, and the system boosted to the lab frame. The lifetime and decay distance were calculated, based on the lifetime of the K_S^0 ($c\tau = 2.676$ cm), and the secondary vertex produced by adding this decay distance to the primary vertex coordinates.

The two tracks making up the K^0 were then traced from the decay vertex to $x = -90$ cm in the Omega reference system, taking into account local field values in the tracing. This x coordinate is the position of the first of the WA91 MWPC's. At this point the direction cosines of each track were re-calculated. In order to check that the vertices so generated would be accepted by WA91, each track of the vertex was now traced to further downstream to check that it stayed in the sensitive region for the MWPCs. The requirement was:

$$\begin{aligned} \text{if } x_{VERTEX} &\leq -90 \text{ trace to } -50 \text{ cm} \\ \text{if } x_{VERTEX} &> -90 \text{ trace to } x_{VERTEX} + 30 \text{ cm} \end{aligned}$$

followed by the requirement that the track must lie within the region defined by the chamber i.e. :

$$|y| \; < \; 75 \text{ cm} \quad \text{and} \quad |z| \; < \; 50 \text{ cm}$$

after the extrapolation. This was implemented in order to check that tracks would pass through at least four of the MWPC chambers.

7.6.2 Smearing of Generated vertices

Subsequent to the generation and extrapolation described above, the direction cosines and positions of the tracks have to be smeared, in order to reproduce the kind of uncertainties found in real events due to the finite resolution of the detectors and the efficiencies of tracking routines.

In order to produce K^0's that mirrored real events, a Gaussian smearing function was used to smear the momenta of each of the two generated pion tracks, creating a spread in the total momentum of the V^0 produced by combining them.

$$\Delta p \; = \; \frac{p^2}{10^4 \sigma \sqrt{2\pi}} exp(-\frac{p^2}{2\sigma^2})$$

where $\sigma = 6$ MeV.

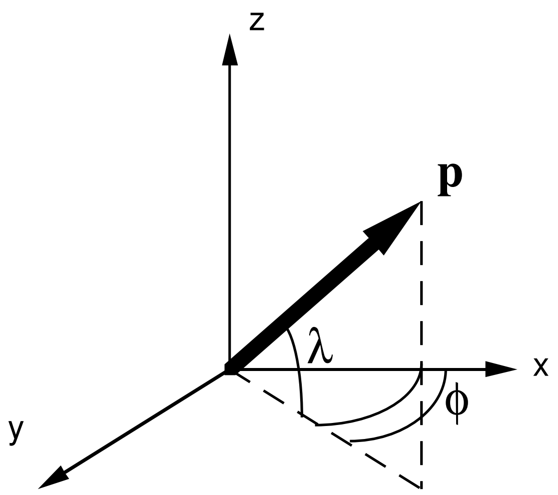

Figure 7.6: Dip angle (λ) and azimuthal angle (ϕ) defined by the momentum of a track, as used in the smearing described in the text.

Smearing was introduced on the azimuthal angle(ϕ) and dip angle (λ) of tracks (as represented in figure 7.6) according to the relations:

$$\Delta\phi = \frac{1.2}{\sigma\sqrt{2\pi}} exp(-\frac{\phi^2}{2\sigma^2})$$

and

$$\Delta\lambda = 1.5\Delta\phi.$$

where $\sigma = 6$ mradians.

The differences in resolution have been documented previously for the Omega experimental setup [70].

This difference reflects the difference in resolution of wire chambers with regard to y and z coordinates. Because of the way the z coordinate is produced, there is a greater uncertainty in z than in y or x. This in turn leads to a larger uncertainty in the angle of dip, λ.

The direction cosines for each of the two tracks making up the V^0 were now recalculated using the smeared values.

7.6.3 Smearing of first points of tracks

To correctly take account of experimental resolution, the proportion of tracks having their first points in the the 1mm chambers needs to be determined. This number was produced by looking at first points on tracks from real data. The proportion of real V^0's where both tracks had a first point in the 1mm chambers was 35.4% and the number having one of the two tracks in the 1mm chambers was 49.4%. The remaining 15.2% had first points for both tracks in the A or B MWPC planes. These numbers are important since the 1mm chambers have a smaller pitch than the A or B chambers, and as such need a smaller σ to describe the track resolution.

The generating code for the K^0 events were required to smear events according to the percentages quoted above. The first points of each track were smeared by an amount Δ_{point} according to the Gaussian distribution:

$$\Delta_{point} = \frac{1}{\sigma\sqrt{2\pi}} exp(-\frac{x^2}{2\sigma^2})$$

where

$$
\begin{aligned}
\sigma^{y}_{1mm} &= 320\mu \\
\sigma^{z}_{1mm} &= 320\mu \\
\sigma^{y}_{A,B} &= 650\mu \\
\sigma^{z}_{A,B} &= 2500\mu
\end{aligned}
$$

7.6.4 Smearing of the primary vertex position

The generated primary vertex has to have an uncertainty associated with it. When the primary vertex is calculated by the TRIDENT event reconstruction program, it uses the slow proton information and the re-traced slow track as mentioned previously. There is an uncertainty in position associated with this; the vertex position may not be properly reproduced since there may be multiple scattering effects in the target. In the light of this, the generated primary vertex position was smeared with a Gaussian distribution, in order to give a $\pm$ 0.5 cm spread about the generated value. This is the observed difference between tracks traced from the downstream chambers and the vertex position established using the slow proton and beam.

The distribution in the $\pi\pi$ mass spectrum after the application of the various smearings applied above were calibrated to the real $\pi\pi$ spectrum.

7.6.5 Differences between generated and reconstructed vertex position

Having implemented the smearing factors described above, the smeared direction cosines and smeared vertex positions were used as input to the V^0 recovery program. The original positions of the generated K^0 vertices were also used, and this enables comparisons to be made between reconstructed positions and generated ones.

The importance of having a good resolution for first points of tracks can be demonstrated by comparing the difference between the reconstructed vertex position and the original generated position. This difference was plotted having smeared the first points of tracks using each of the two different resolutions for the forward chambers. The plots in fig. 7.7 shows the difference between the reconstructed secondary vertex position and the generated one. Figure 7.7 a) is produced by using the 1mm chamber resolution for all tracks, whilst 7.7 b) is produced by using the resolution required for the A and B chambers in all cases. The resolution of the 1mm chambers clearly gives a far better first point for reconstructing tracks accurately, producing a more accurate vertex position.

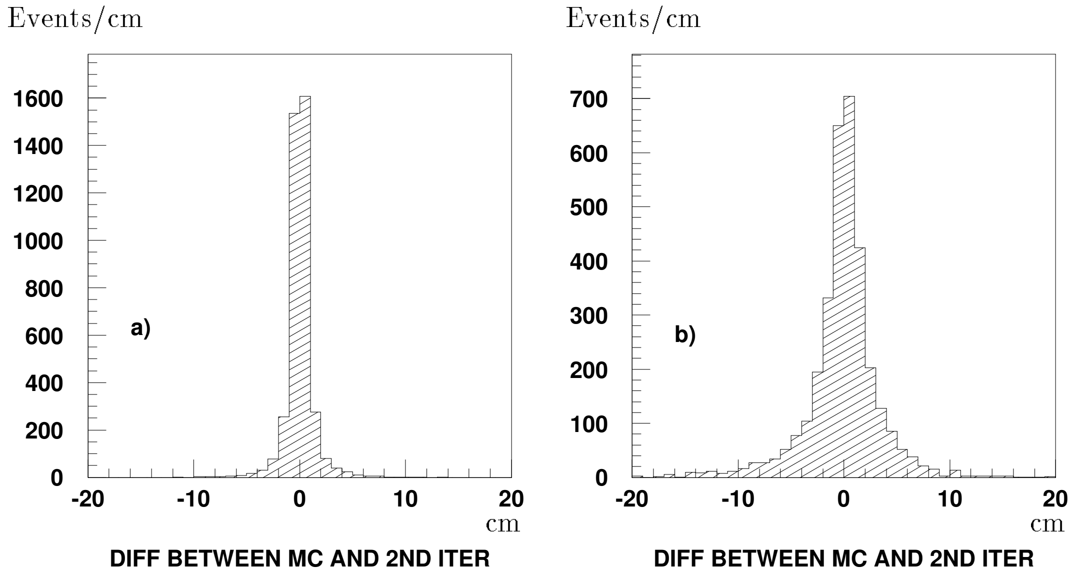

Figure 7.7: Difference between generated vertices and vertices reconstructed using a) the 1mm chamber and b) the A and B chamber resolution.

The difference between generated and reconstructed vertices for both the first and second vertex finding iterations are shown in fig 7.8 a) and 7.8 b) respectively. These plots are obtained by having no smearing on any tracks. As can readily be seen, the second iteration is a far better method for correct reconstruction of the generated position than just a simple helix approximation, justifying the need for a second iteration to be performed.

The same plots are shown in figure 7.9 after all the smearings described previously have been applied. The distribution obtained after the first iteration is shown in fig 7.9 a) and 7.9 b) shows the distribution after the second iteration. Both the distributions are centred about zero, with widths

$$\sigma_{1st} = 1.48 \pm 0.04 \text{ cm}$$

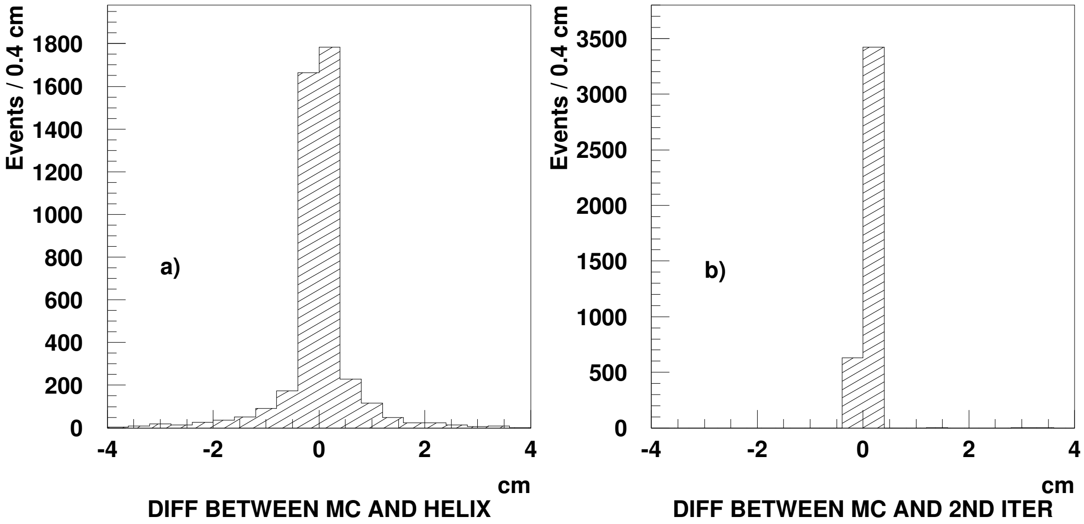

Figure 7.8: Difference between generated vertices and vertices reconstructed using a) the first iteration and b) the second iteration, where no smearing has been implemented.

$$\sigma_{2nd} \quad = \quad 1.19 \ \pm \ 0.03 \text{ cm}$$

respectively. Although smearing causes a greater uncertainty in the vertex position, the second iteration still produces a narrower distribution, and hence a more accurate vertex position.

Figure 7.10 shows the differences between generated and reconstructed vertex positions for x, y and z after the final iteration.

The plots have been fitted with single Gaussians, and the values obtained from the fit are :

$$\begin{aligned} \sigma_x &= 1.18 \ \pm \ 0.04 \text{ cm} \\ \sigma_y &= 0.056 \ \pm \ 0.001 \text{ cm} \\ \sigma_z &= 0.099 \ \pm \ 0.003 \text{ cm} \end{aligned}$$

7.6.6 Introduction of other tracks

In order to determine what effects the presence of other tracks besides the ones from the V^0 would have on vertex reconstruction, tracks originating from the primary vertex were written out for each event as well as that from the V^0 vertex. Two

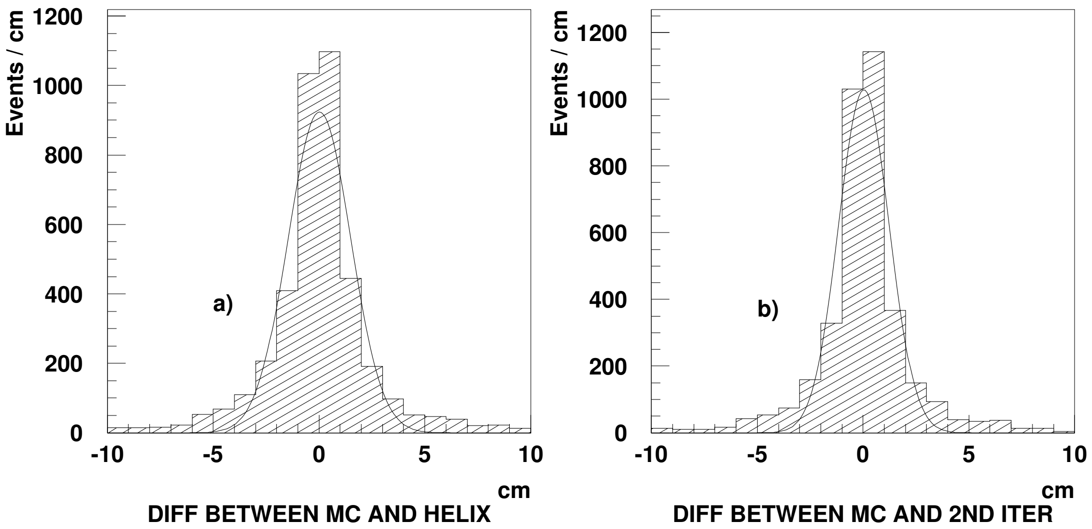

Figure 7.9: Difference between generated vertices and vertices reconstructed using a) the first iteration and b) the second iteration.

tracks were used for each event, one positive and one negative. These were traced from the primary vertex to the chamber positions, where the same smearing was performed on the track parameters as previously. These two extra tracks were then written out with the tracks from the V^0 for each event. 5000 such events were generated for the study of this effect.

The V^0 recovery program was used to read in the four tracks, and produce helices by looping over possible combinations. After the second iteration stage, the program was found to have produced vertices using combinations of tracks from both the primary and the secondary vertex. The difference between the calculated vertex position and the primary vertex is shown in figure 7.11, for the three different types of vertices reconstructed. These are :

- vertices reconstructed using both tracks generated at the primary vertex, as shown in figure 7.11 a)
- vertices where one of the vertex tracks comes from the generated V^0, as shown in figure 7.11 b)
- vertices where both tracks come from the generated V^0 tracks, as in 7.11 c).

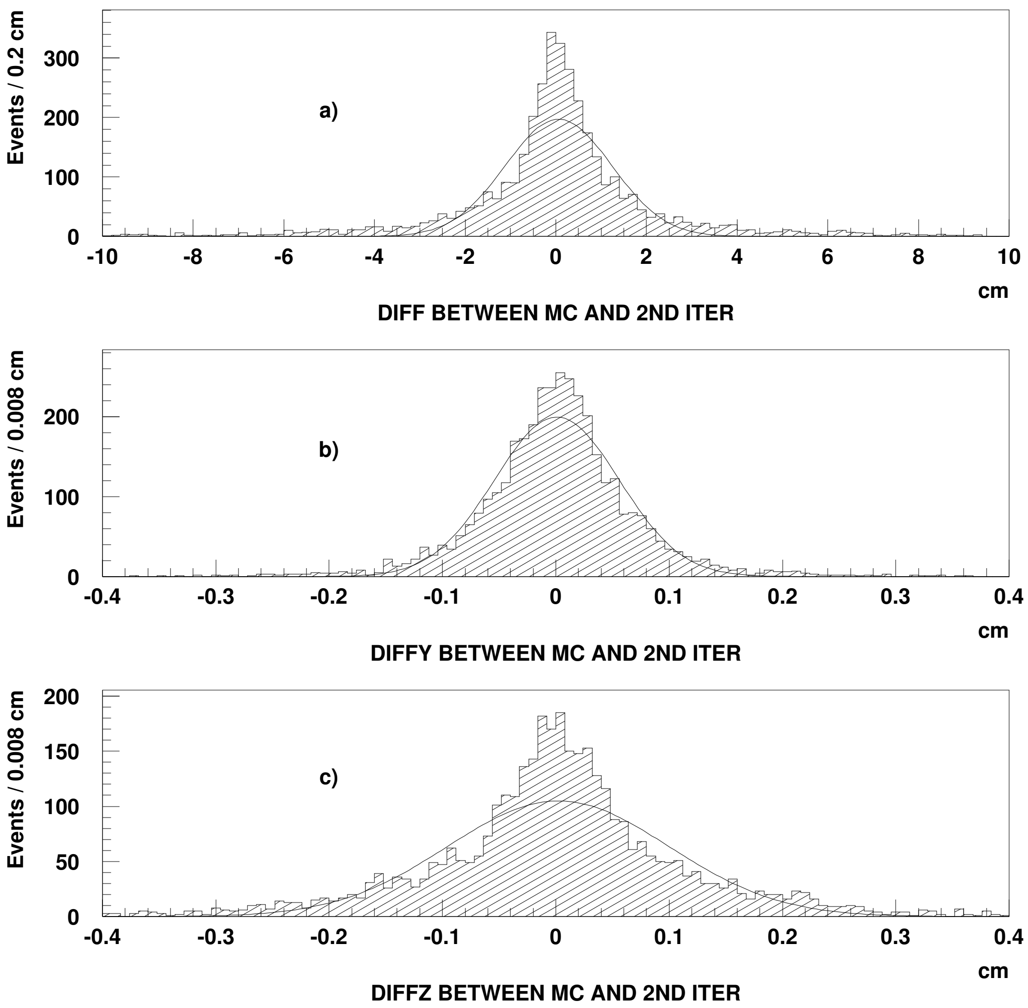

Figure 7.10: Difference between generated and reconstructed vertices for a) x position b) y position and c) z position. Fit is described in the text.

Ideally, all vertices reconstructed should come from the two tracks from the generated V^0. The vertices that are produced from the two primary vertex tracks lie predominantly at the primary vertex, and so most will be eliminated after the second iteration stage when the tight cuts are implemented. The main problem of incorrect vertex assignment comes when considering vertices that have been produced by combining one of the true V^0 tracks with one of the tracks from the primary vertex.

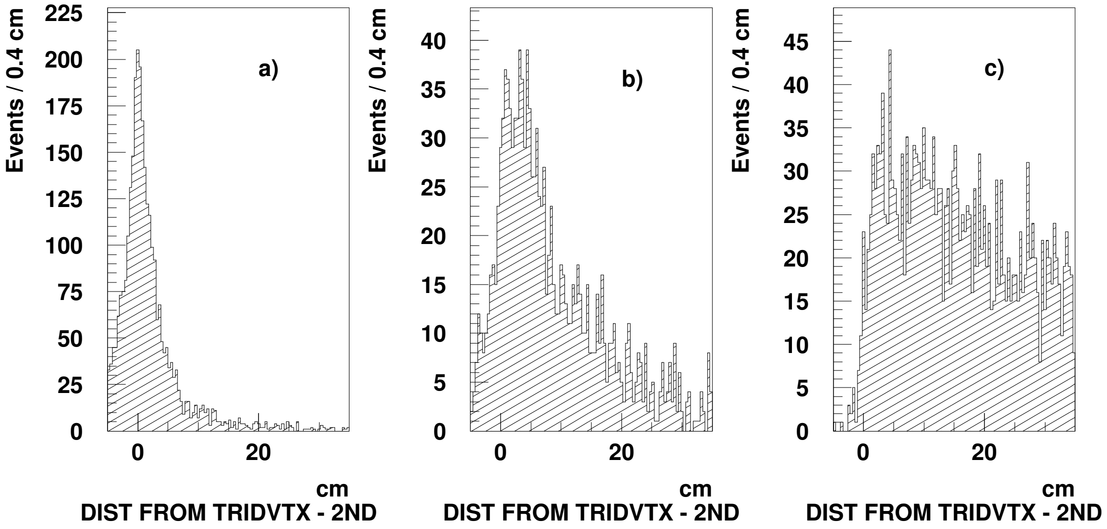

Figure 7.11: Distance from primary vertex after the second iteration for a) vertices where both tracks originate in the primary vertex b) where one of the vertex tracks comes from the primary vertex and c) where both vertex tracks come from the generated V^0.

Because of the smearing on the track parameters, this means that a significant number of these vertices are found at a distance that passes the *DIFFX* cut of 4cm. The same plots as described above are shown in figure 7.12, where the *DIFFX* cut has been made. The proportion of events passing the *DIFFX* cut are in the ratio $0.16 : 0.24 : 1$ for plots a), b) and c) respectively. In the final $\pi\pi$ mass plot, after all cuts had been applied, then the relative proportions had fallen to $0.02 : 0.02 : 1$, as indicated in table 7.1. The background is at a smaller level than that observed in the real data since real data contains events from other channels that have passed the $K^0_S K^\pm \pi^\mp$ selection cuts, yet do not have a K^0 vertex. The ratio calculated above serves to demonstrate the background produced from $K^0_S K^\pm \pi^\mp$ events only,

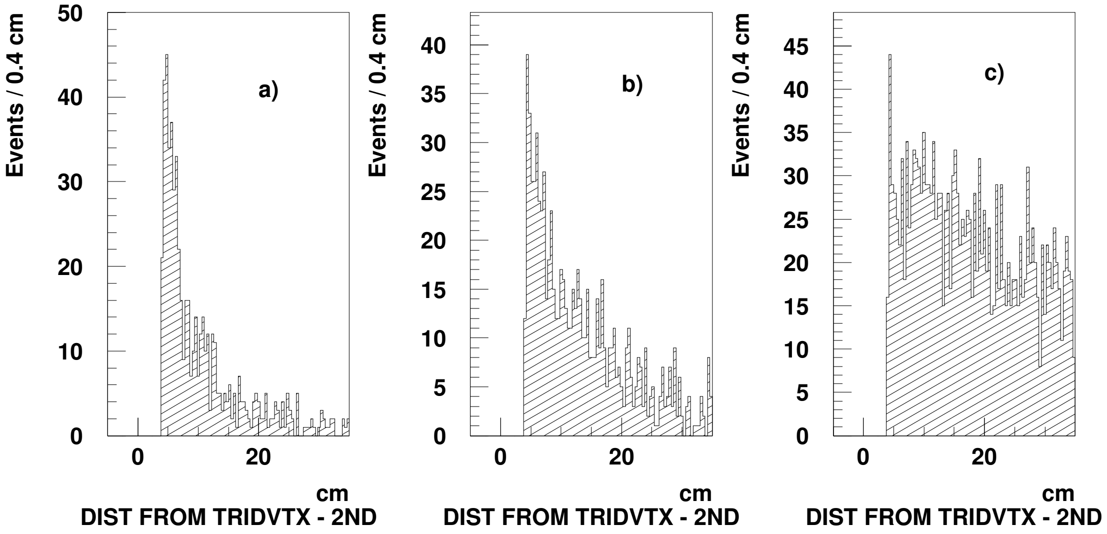

Figure 7.12: Distance from primary vertex after the second iteration and the *DIFFX* cut of 4 cm for a) vertices where both tracks originate in the primary vertex b) where one of the vertex tracks comes from the primary vertex and c) where both vertex tracks come from the generated V^0.

Iteration	both V^0 tracks	one V^0 track	none
first	4038	1492	2939
second and *DIFFX*	3631	892	614
second and all cuts	3393	78	70

Table 7.1: Number of vertices passing subsequent steps in selection, for the three types of vertices found by the V^0 recovery code.

and not events that may have come from mis-assigned events.

7.6.7 Efficiency for finding smeared vertices

It was found from a sample of 5000 generated vertices that 67.9 % were reconstructed and passed the cuts as described in earlier sections. The final $\pi\pi$ mass plot containing these reconstructed vertices is shown in figure 7.13. The plot has been fitted with two Gaussians and the distribution was found to have $\sigma_1 = 5.5$ MeV and $\sigma_2 = 10.1$ MeV. This is consistent with the fits to the $\pi\pi$ spectrum for real data.

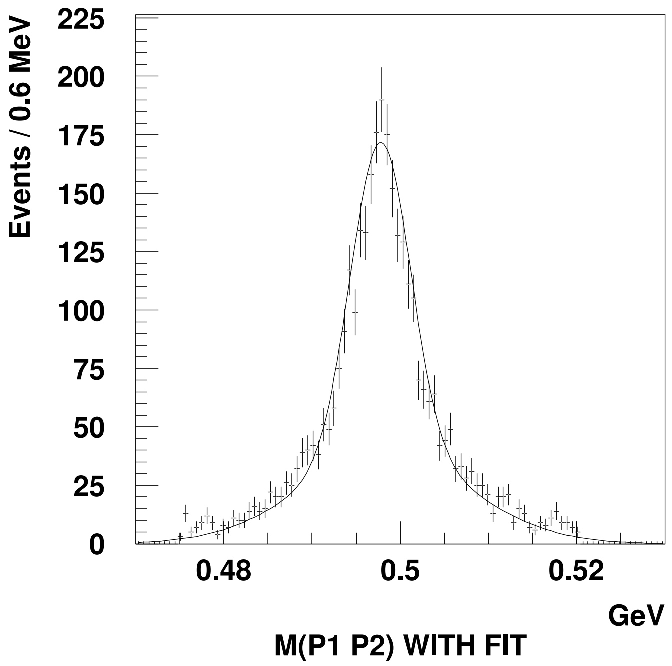

Figure 7.13: The generated $\pi\pi$ mass spectrum, fitted with two Gaussian distributions.

7.7 Branching ratio

The branching ratio for the $f_1(1285)$ with respect to the $K\overline{K}\pi$ and $\pi^+\pi^-\pi^+\pi^-$ channels is given by

$$\frac{f_1(1285) \to K\overline{K}\pi}{f_1(1285) \to \rho\pi\pi} = \frac{f_{K\overline{K}\pi}\ N_{K^0_S K^\pm \pi^\mp}\ Acc(4\pi)\ Eff(4\pi)}{f_{\rho\pi\pi}\ N_{4\pi}\ Acc(K^0_S K^\pm \pi^\mp)\ Eff(K^0_S K^\pm \pi^\mp)\ Eff(V^0)}$$

The track reconstruction efficiencies, $Eff(4\pi)$ and $Eff(K^0_S K^\pm \pi^\mp\ )$ were assumed to be the same for both channels, since the events being considered in the

Correction Factor	$K^0_S K^\pm \pi^\mp$ channel	$\rho\pi\pi$ channel
V^0 code efficiency	$Eff(V^0) = 0.679$	
TRIDENT V^0 efficiency	$Eff(V^0) = 0.75$	
Acceptance	$\mathrm{Acc}(K^0_S K^\pm \pi^\mp) = 0.138$	$\mathrm{Acc}(4\pi) = 0.144$
Unseen decay modes	$f_{K\overline{K}\pi} = 4.37$	$f_{\rho\pi\pi} = 3.0$

Table 7.2: Summary of corrections required in the the $K^0_S K^\pm \pi^\mp$ and $\rho\pi\pi$ channels for branching ratio evaluation.

calculation lie within the same kinematic region. The other correction factor values are summarized in table 7.2

Using the number of events in the $f_1(1285)$ mass window, $N_{K^0_S K^\pm \pi^\mp}$ and $N_{4\pi}$, and the above correction factors for each channel, the branching ratio for the $f_1(1285)$ was determined for both TRIDENT efficiency, and for V^0 efficiency. These values were then weighted by the number of events found by each V^0 finding method giving a value of branching ratio of :

$$\frac{f_1(1285) \to K\overline{K}\pi}{f_1(1285) \to 4\pi} = (0.29 \ \pm \ 0.07).$$

The Particle Data Group value [36] of the branching ratio for the two channels under consideration is

$$\frac{f_1(1285) \to K\overline{K}\pi}{f_1(1285) \to 4\pi} = (0.33 \ \pm \ 0.04).$$

It is worth noting that the PDG value comes from previous WA76 experimental analyses for $f_1(1285)$ decay, one set of analysis assuming both $a_0(980)\pi$ and $\rho\pi\pi$ intermediate states, the second assuming $\rho\pi\pi$ only.

Chapter 8

Conclusions

Predictions from Quantum Chromodynamics indicate that as well as the conventional bound states of quarks, the baryons and mesons, there should exist glueballs, hybrids and four-quark states. Several reaction mechanisms have been put forward as being 'glue-rich', where these gluon rich states may be produced. One such mechanism is central production, where the momentum exchange at each vertex is small.

This thesis describes the selection of the central production reaction

$$pp \rightarrow p_f(X^0)\ p_s$$

at 450 GeV/c incident proton beam. The data was obtained during a three month run in the autumn of 1992.

The method used to develop code that successfully recovers V^0 vertices in the WA91 experiment that were mis-assigned as coming from the primary vertex has been described. The method, involving two iterations in determination of vertex position has been demonstrated to be superior to a simple helix minimisation.

This code was implemented in order to recover events from the centrally produced $K^0_S K^\pm \pi^\mp$ system, this channel containing the $f_1(1420)$, which is currently without assignment in the established $q\overline{q}$ nonets. Clear signals for both the $f_1(1285)$ and $f_1(1420)$ are observed in the $K^0_S K^\pm \pi^\mp$ mass spectrum. A fit was performed on the $K^0_S K^\pm \pi^\mp$ data, establishing the masses and widths of the two mesons to be

$$\begin{aligned} \mathrm{M}_{f(1285)} &= 1281 \ \pm\ 2\ \mathrm{MeV/c^2} \\ \Gamma_{f(1285)} &= 19 \ \pm\ 5\ \mathrm{MeV/c^2} \end{aligned}$$

$$\begin{aligned} \mathrm{M}_{f(1420)} &= 1426 \ \pm \ 2 \ \mathrm{MeV/c}^2 \\ \Gamma_{f(1420)} &= 61 \ \pm \ 7 \ \mathrm{MeV/c}^2. \end{aligned}$$

These values are consistent with the values listed by the Particle Data Group.

A spin parity analysis has been performed using Zemach formalism. Single wave fits to the Dalitz plot, and subsequent two wave fits for all combinations of waves up to spin two demonstrated that both mesons have the quantum numbers $\mathrm{J}^{PG} = 1^{++}$. The $f_1(1285)$ is found to decay *via* the $a_0(980)\pi$ intermediate state. The $f_1(1420)$ decay is described by the intermediate state $K^*\overline{K}$. Consideration of the wave fits to the Dalitz plot in the $f_1(1420)$ region and its projections have determined that no 0^{-+} wave is required to describe the data, and have been used to ascertain the level of mis-assignment of charged particles in $K^0_S K^\pm \pi^\mp$ events. The energy dependence of the $f_1(1420)$ and the $f_1(1285)$ are found to be different, when the 450 GeV/c data is compared to earlier central production data at lower incident momentum.

The branching ratio

$$\frac{f_1(1285) \rightarrow K\overline{K}\pi}{f_1(1285) \rightarrow \rho\pi\pi}$$

has been determined from the $K^0_S K^\pm \pi^\mp$ and $\rho^0\pi^+\pi^-$ channels to be 0.29 $\pm$ 0.07, consistent with previous values.

The spin parity assignment determined from the 450 GeV/c data for the $f_1(1420)$ is of considerable interest. When trying to assign the $f_1(1420)$ a place in the established $q\overline{q}$ nonets, difficulties arise since there is a better candidate for the nonet where it would be envisaged that the $f_1(1420)$ would belong. This and other evidence all serves to suggest that the $f_1(1420)$ is non-$q\overline{q}$ in nature, and that it is most probably a $K^*\overline{K}$ molecule.

The WA91 experiment had a further experimental run in April 1994, with an experimental setup that incorporated Cerenkov detectors in addition to the Standard WA91 layout. This should enable the $K^0_S K^\pm \pi^\mp$ channel to be re-studied with less ambiguity between the K and the π for $K^0_S K^\pm \pi^\mp$ events than was present in the data considered in this thesis, and with greater statistics. This should result in a cleaner $f_1(1420)$ signal. Because of this, the $f_1(1420)$ should be able to be further studied, and more information on its nature will be produced.

Appendix A

The Ehrlich mass formula

The Ehrlich mass formula relies upon choosing two particles which can act as a particle-antiparticle pair. In the case of the $K_S^0 K^{\pm}\pi^{\mp}$ channel, then these two particles are the K_S^0 and the $K^{\pm}$. Their effective mass is calculated from the remaining particle and the momenta of the pair particles and plotted. If a correct assignment has been made then a peak at the K mass squared should appear.

For a central system decaying to final state $K_S^0 K^{\pm}\pi^{\mp}$ as in figure A.1 then by applying conservation of energy :

$$E = E_b + E_t = E_f + E_s + E_K + E_{K^0} + E_\pi$$

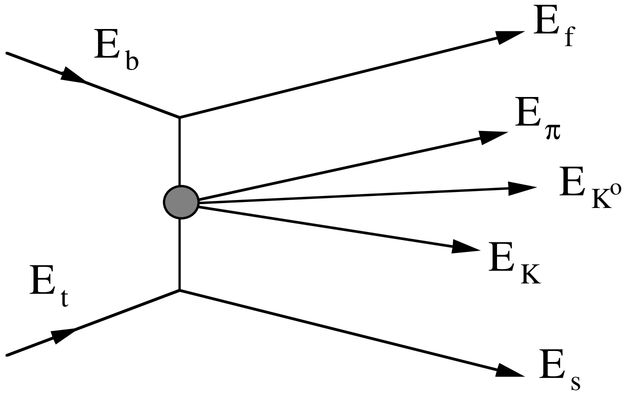

Figure A.1: Diagrammatic representation of the centrally produced $K_S^0 K^{\pm}\pi^{\mp}$ system.

Now define the quantity A by

$$\begin{aligned} A &= (E_K + E_{K^0})^2 = (E - E_f - E_s - E_\pi)^2 \\ &= E_K^2 + E_{K^0}^2 + 2E_K E_{K^0} \\ &= M_K^2 + p_K^2 + M_{K^0}^2 + p_{K^0}^2 + 2[(M_K^2 + p_K^2)(M_{K^0}^2 + p_{K^0}^2)]^{\frac{1}{2}} \end{aligned}$$

Now, assuming that $M_K = M_{K^0}$ then

$$A = 2M_K^2 + p_K^2 + p_{K^0}^2 + 2[M_K^4 + M_K^2 p_K^2 + M_K^2 p_{K^0}^2 + p_K^2 p_{K^0}^2]^{\frac{1}{2}}$$

Also,

$$(E - E_f - E_s - E_\pi)^2 = 2M_K^2 + p_K^2 + p_{K^0}^2 + 2[M_K^4 + M_K^2 p_K^2 + M_K^2 p_{K^0}^2 + p_K^2 p_{K^0}^2]^{\frac{1}{2}}.$$

and we define B by

$$\begin{aligned} B^2 &= [(E - E_f - E_s - E_\pi)^2 - p_K^2 - p_{K^0}^2]^2 \\ &= \left\{2M_K^2 + 2[M_K^4 + M_K^2(p_K^2 + p_{K^0}^2) + p_K^2 p_{K^0}^2]^{\frac{1}{2}}\right\}^2 \\ &= 4M_K^2 + 4[M_K^4 + M_K^2(p_K^2 + p_{K^0}^2) + p_K^2 p_{K^0}^2] + 8M_K^2[M_K^4 + M_K^2(p_K^2 + p_{K^0}^2) + p_K^2 p_{K^0}^2]^{\frac{1}{2}} \\ &= 8M_K^2 + 4M_K^2(p_K^2 + p_{K^0}^2) + 4p_K^2 p_{K^0}^2 + 8M_K^2[M_K^4 + M_K^2(p_K^2 + p_{K^0}^2) + p_K^2 p_{K^0}^2]^{\frac{1}{2}} \end{aligned}$$

From this,

$$\begin{aligned} B^2 - 4p_K^2 p_{K^0}^2 &= 4M_K^2\left\{2M_K^2 + p_K^2 + p_{K^0}^2 + 2[M_K^4 + M_K^2(p_K^2 + p_{K^0}^2) + p_K^2 p_{K^0}^2]^{\frac{1}{2}}\right\} \\ &= 4M_K^2(E_K + E_{K^0})^2 \end{aligned}$$

and thus

$$M_K^2 = \frac{B^2 - 4p_K^2 p_{K^0}^2}{4A}$$

i.e.

$$M_K^2 = \frac{[\{E - E_f - E_s - E_\pi\}^2 - p_K^2 - p_{K^0}^2]^2 - 2(p_K p_{K^0})^2)}{4\left\{p_K^2 + p_{K^0}^2 + \{(E - E_b - E_s - E_\pi)^2 - p_K^2 - p_{K^0}^2\}\right\}}$$

Appendix B

G parity Eigenstates and the Dalitz plot

B.1 G-parity

G parity is a 180^o rotation about the y axis in isospin space, followed by charge conjugation. Consider the G-operator acting on a pion wavefunction, $|\pi^+\rangle$. The rotation reverses I_3, converting $\pi^+ \rightarrow \pi^-$, and C flips the charge back, $\pi^- \rightarrow \pi^+$. We may write

$$\begin{aligned} G|\pi^+\rangle &= \pm|\pi^+\rangle \\ G|\pi^-\rangle &= \pm|\pi^-\rangle \\ G|\pi^0\rangle &= \pm|\pi^0\rangle \end{aligned}$$

Since the neutral pion is an eigenstate of C, with eigenvalue +1 as determined from $\pi^0 \rightarrow 2\gamma$, then the rotation eigenvalue is $(-1)^I$ = -1. From this, we can write

$$G|\pi^0\rangle = -|\pi^0\rangle.$$

Since charged pions are not eigenstates of C, they can arbitrarily be assigned a G-parity. The convention chosen is

$$G|\pi^\pm\rangle = -|\pi^\pm\rangle.$$

In this way, G-parity is useful for describing charged particle, which are eigenstates of G, but not of C. G-parity extends to the case of n pions, where the G-parity is $(-1)^n$.

and is usful in considering selection rules for meson decays. G-parity conservation applies in, for example, the pion decay modes of $\rho(770) \rightarrow 2\pi$ where G(ρ) = +1, and $\omega(783) \rightarrow 3\pi$ where G(ρ) = -1.

If one now considers the case of strange mesons, such as the K, then

$$\begin{aligned} G|K^+\rangle &= -|\overline{K}^0\rangle \\ G|K^0\rangle &= -|K^-\rangle \\ G|\overline{K}^0\rangle &= +|K^+\rangle \\ G|K^-\rangle &= +|K^0\rangle \end{aligned}$$

i.e. kaons are not eigenstates of either C or G. Only non-strange neutral mesons are eigenstates of C and G.

To construct wavefunctions involving kaons that are G-parity eigenstates, then combinations of different kaon states must be used.

B.2 G-parity and the $K^0_S K^\pm \pi^\mp$ system

Consider the $K\overline{K}\pi$ system. The amplitude for the state can be described in terms of the angular momentum of the $K\overline{K}$ system as

$$A = \sum_l a_l \Psi_l(K\overline{K})$$

Now, it is possible to construct an amplitude B that describes the interchange $K \rightarrow \overline{K}$ and vice versa where

$$\begin{aligned} B &= \sum_l a_l \Psi_l(\overline{K}K) \\ &= \sum_l (-1)^l a_l \Psi_l(K\overline{K}). \end{aligned}$$

These amplitudes can now be combined to form wavefunctions $\Psi_\pm$ that are either even or odd under $K \rightarrow \overline{K}$ interchange

$$\begin{aligned} \Psi_+ = \frac{(A+B)}{2} &= \sum_{l=even} a_l \Psi_l(K\overline{K}) \\ \Psi_- = \frac{(A-B)}{2} &= \sum_{l=odd} a_l \Psi_l(K\overline{K}) \end{aligned}$$

A neutral $K\overline{K}\pi$ system can be formed in two ways, as either $(K\overline{K})^0\pi^0$ or $(K\overline{K})^{\pm}\pi^{\mp}$. The charged $K\overline{K}$ system is the one of interest to WA91 and has I=1. G-parity may be written as

$$G = (-1)^{l+S+I}$$

where S = 0 for $K\overline{K}$ and I = 1. Since the G-parity of a π is negative, then this means

$$G\Psi_{\pm} = \pm\Psi_{\pm}$$

In order to obtain a complete wavefunction for the states possible, one must consider the Clebsch-Gordan coefficients. From tables,

$$\begin{aligned}
K^{*+} &= \sqrt{\frac{2}{3}}\pi^+K^0 - \sqrt{\frac{1}{3}}\pi^0K^+ \\
K^{*0} &= \sqrt{\frac{1}{3}}\pi^0K^0 - \sqrt{\frac{2}{3}}\pi^-K^+ \\
\overline{K}^{*0} &= -\sqrt{\frac{1}{3}}\pi^0\overline{K}^0 + \sqrt{\frac{2}{3}}\pi^+K^- \\
K^{*-} &= -\sqrt{\frac{2}{3}}\pi^-\overline{K}^0 + \sqrt{\frac{1}{3}}\pi^0K^-.
\end{aligned}$$

Considering the states with positive strangeness, a wavefunction can be construced for a neutral $K\overline{K}\pi$ system with isospin I,

$$A_I = \sqrt{\frac{1}{2}}(K^{*+}K^- - (-1)^I K^{*0}\overline{K}^0)$$

In a similar manner, the wavefunction for negative strangeness can be constructed by interchange of K and $\overline{K}$:

$$B_I = \sqrt{\frac{1}{2}}(\overline{K}^{*0}K^0 - (-1)^I K^{*-}K^+).$$

By combining these two possibilities, the total wavefunction for the $K\overline{K}\pi$ system is obtained, Φ_g where

$$\Phi_g = \sqrt{\frac{1}{2}}(A_I + gB_I)$$

where g is ± 1. This can be expresed in terms of the charge state of the π as

$$\Phi_g = \Gamma_g + \Theta_g$$

where

$$\Gamma_g = \sqrt{\frac{1}{6}}\left\{\left\{(\pi^+K^0)K^- + g(\pi^+K^-)K^0\right\} + (-1)^I\left\{(\pi^-K^+)\overline{K}^0 + g(\pi^-\overline{K}^0)K^+\right\}\right\}$$

$$\Theta_g = -\sqrt{\frac{1}{12}}\left\{\left\{(\pi^0K^+)K^- + g(\pi^0K^-)K^+\right\} + (-1)^I\left\{(\pi^0K^0)\overline{K}^0 + g(\pi^0\overline{K}^0)K^0\right\}\right\}$$

There are 4 possible reactions that can be observed in the WA91 $K^0_SK^\pm\pi^\mp$ channel, namely

$$\begin{aligned}
K^{*+}K^- &\rightarrow (\pi^+K^0)K^- \\
K^{*0}\overline{K}^0 &\rightarrow (\pi^-K^+)\overline{K}^0 \\
K^{*-}K^+ &\rightarrow (\pi^-\overline{K}^0)K^+ \\
\overline{K}^{*0}K^0 &\rightarrow (\pi^+K^-)K^0.
\end{aligned}$$

This means that for the expression for Φ_g, the term that is of importance is Γ_g. By setting g to either $+1$ or -1 it can be seen that the relation

$$G\Gamma_g = g\Gamma_g$$

is satisfied i.e. a neutral $K\overline{K}\pi$ system with a charged π has a G-parity given by g.

B.3 The Dalitz Plot

For the $K^0_SK^\pm\pi^\mp$ channel, there are four possible combinations which could be plotted against each other in a Dalitz Plot :

$$\begin{array}{ll}
a)\ \ M^2(\pi^+K^0) & b)\ \ M^2(\pi^+K^-) \\
c)\ \ M^2(\pi^-K^+) & c)\ \ M^2(\pi^-\overline{K}^0)
\end{array}$$

giving rise to two possible ways of presenting the $K^0_SK^\pm\pi^\mp$ data.

- Respect the charge of states, plotting the charged di-particle combinations against the neutral ones.
- Respect the strangeness of states, plotting positive strangeness combinations against negative *e.g.* a) against b).

In order to determine the significance of the two possible options, consider the following arguement. From the expression for Γ_g :

$$\begin{aligned}
\phi_g^+ &= (\pi^+ K^0)K^- + g(\pi^+ K^-)K^0 \\
\phi_g^- &= (\pi^- K^+)\overline{K}^0 + g(\pi^- \overline{K}^0)K^+
\end{aligned}$$

where the superscripts designate the charge state of the π. If we now assume that both of the charge states will have the same admixture of G-parity eigenstates, then

$$\begin{aligned}
\phi^+ &= \text{a } \phi_+^+ + \text{b } \phi_-^+ \\
\phi^- &= \text{a } \phi_+^- + \text{b } \phi_-^-
\end{aligned}$$

where a and b are two arbitrary complex numbers. If we now respect the strangeness of states, then this is equivalent to

$$\begin{aligned}
X &= (\pi^+ K^0)K^- = (\pi^- K^+)\overline{K}^0 \\
Y &= (\pi^+ K^-)K^0 = (\pi^- \overline{K}^0)K^+.
\end{aligned}$$

If these are now substituted into the expressions for ϕ^+ and ϕ^-, then

$$\begin{aligned}
\phi^+ &= a\ (X+Y) + b\ (X-Y) \\
\phi^- &= a\ (X+Y) + b\ (X-Y).
\end{aligned}$$

If the charges of the combinations is respected, then this means

$$\begin{aligned}
X &= (\pi^+ K^0)K^- = (\pi^- \overline{K}^0)K^+ \\
Y &= (\pi^+ K^-)K^0 = (\pi^- K^+)\overline{K}^0.
\end{aligned}$$

which leads to

$$\begin{aligned}
\phi^+ &= a\ (X+Y) + b\ (X-Y) \\
\phi^- &= a\ (X+Y) - b\ (X-Y).
\end{aligned}$$

Because of the choice of combinations, the two are now different.

If the strangeness of combinations is respected, then the two amplitudes are the same, and any background terms such as incoherent K^* production are entered equally on the Dalitz plot. However, in the case where charge is respected, then the amplitudes are different, this meaning that incoherent production would show up as an assymmetry in the Dalitz plot projections.

Appendix C

The Maximum Likelihood Fit

The Maximum Likelihood Fit method assumes that the observation of a set of quantities x_i is related to a set of parameters α_i by a probability distribution $P(\alpha_i, x_i)$. The maximum likelihood method consists of finding the set of values α_i which maximises the joint probability density for all the observations, given by

$$\mathcal{L}(\alpha) = \prod_n P(\alpha_i, x_i)$$

where $\mathcal{L}(\alpha)$ is known as the likelihood, and the product is over the total number of events observed in the experiment. If one now takes the logarithmic likelihood

$$\ln(\mathcal{L}(\alpha)) = \sum_n \ln(P(\alpha_i, x_i))$$

then this is an easier quantity to deal with as we now have a sum rather than a large product, and both $\mathcal{L}(\alpha)$ and $\ln(\mathcal{L}(\alpha))$ are maximised for the same set of α. In the case of fitting the Dalitz plot each x_i is a Zemach amplitude for the event, and α_i is the amount of that amplitude. The overall probability for each event is given by

$$P(\alpha_i, x_i) = \sum_i \alpha_i \mid \mathcal{M}_i^{JP} \mid^2 + (1 - \sum_i \alpha_i)$$

where $\mathcal{M}_i^{JP}$ is the Zemach amplitude for a specific wave with spin J and parity P, α_i is the amount of that amplitude, and $(1 - \sum \alpha_i)$ represents the background.

Bibliography

[1] F. Halzen and A.D. Martin, *Quarks and Leptons: An Introductory Course in Modern Particle Physics*, John Wiley and Sons, 1984.

[2] D.H. Perkins, *Introduction to High Energy Physics*, Addison-Wesley Publishing Company, Third Edition 1987.

[3] J.F. Donoghue et al., Phys. Lett. **99B** (1981) 416.
M. Chanowitz and S. Sharpe, Nucl. Phys. **B222** (1983) 211.

[4] C.E. Carlson, Phys. Rev. **30D** (1984) 1594.

[5] G. Schierholz, AIP. Conf. Proc. 185, Particles and Fields 36, *Glueballs, hybrids and exotic hadrons* (1988) 281.
S. Sharpe, *ibid* (1988) 55.

[6] C. Michael, Proc. of the Workshop on QCD, Aachen, 9-13 June 1992.

[7] F. Close, *Gluonic Hadrons*, RAL-87-072 (1987).

[8] C.N. Yang, Phys. Rev.**77** (1950) 242.

[9] N. Isgur, *ibid* (1988) 3.

[10] H.J. Behrend et al., Phys. Lett. **B257** (1991) 505.

[11] R.L Jaffe, Phys. Rev. Lett. **38** (1977) 195.

[12] A. Palano, *The search for gluonic matter*, CERN-EP/87-92 (1987).
Proc. XXII *Rencontres de Moriond*, Les Arc, France 1987.

[13] T. Barnes, *The status of Molecules*, RAL-94-056 (1994).

[14] J. Weinstein and N. Isgur, Phys. Rev. Lett. **48** (1982) 659.

[15] M.R. Pennington, University of Durham report **TDP-94/26** (1994).

[16] J. Weinstein and N. Isgur, Phys. Rev. **D41** (1990) 2236.

[17] J. Weinstein, Phys. Rev. **D47** (1993) 911.

[18] C. Edwards et al., Phys. Rev. Lett. **48** (1982) 458.

[19] T. A. Armstrong et al., Phys. Lett. **B227** (1989) 186.

[20] Bolonkin et al., Nucl. Phys. **B309** (1988) 426.

[21] L.P. Chen et al., Hadron 91 conference **SLAC PUB 5669** (1991).

[22] N. Tornqvist, Phys. Rev. Lett.**67** (1991) 556.

[23] V.V. Anisovich et al., Phys. Lett.**B323** (1994) 233.

[24] F. Binon et al., Nuovo Cimento **A78** (1983) 313.

[25] D. Alde et al., Nucl. Phys. **B269** (1986) 485.

[26] F. Binon et al., Nuovo Cimento **80** (1984) 363.

[27] R. Akhoury and J.M Frere, Phys. Lett. **B220** (1989) 258.

[28] C. Amsler et al,, Phys. Lett. **B291** (1992) 347.

[29] T. Armstrong et al., Phys. Lett.**B228** (1989) 536.

[30] F. Antinori et al., **CERN/PPE 93-133** (1993).

[31] WA91 Proposal, **CERN SPSC/90-2/P249** (1990).

[32] A. Donnachie and P.V. Landshoff, Nucl. Phys. **B244** (1984) 322.

[33] D. Robson, Nucl. Phys. **B130** (1977) 328.

[34] D.M. Chew and G.F Chew Phys. Lett. **B53** (1974) 191.

[35] R. Fernow, *Introduction to experimental particle physics*, Cambridge University Press, 1990.

[36] *Review of Particle Properties* Phys. Rev. **D50** (1994).

[37] P. Baillon et al., Nuovo Cimento **50A** (1967) 393.

[38] C. Dionisi et al., Nucl. Phys. B **169** (1980) 1.

[39] D. Scharre et al., Phys. Lett. **B97** (1980) 329.

[40] C.D. Edwards et al., Phys. Rev. Lett. **49** (1982) 259.

[41] T.A. Armstrong et al., Phys. Lett. **B146** (1984) 273.

[42] A. Palano et al., **CERN/EP 83-107** (1983) 273.

[43] A. Ando et al., Phys. Rev. Lett. **57** (1986) 1296.

[44] S.U. Chung et al., Phys. Rev. Lett. **55** (1985) 779.

[45] T.A. Armstrong et al., Phys. Lett. **B221** (1989) 216.

[46] P.Hill et al., Z. Phys. C **42** (1989) 355.

[47] H.J. Behrend et al., Z. Phys. C **42** (1989) 367.

[48] W.S. Lockman, Proc. Rheinfels Workshop on Hadron Mass Spectrum, St. Goar, 1990, North Holland 1991, Nucl. Phys. **B21** 55 (1990).
M. Burchell, *ibid* (1990) 132.

[49] A. Birman et al., Phys. Rev. Lett. **61** (1988) 1557.

[50] H. Aihara et al., Phys. Rev. **38D** (1988) 1.

[51] F. M. Renard, Nuovo Cim. **80A** (1984) 1.

[52] Z. Bai et al., Phys. Rev. Lett. **49** (1990) 2507.

[53] T.A. Armstrong et al., Z. Phys. C **52** (1991) 389.

[54] Gidal et al., Phys. Rev. Lett. **59** (1987) 2012.

[55] Ph. Gavillet et al., Z. Phys. C **16** (1982) 119.

[56] S.I. Bityukov et al., Phys. Lett. **203B** (1988) 327.

[57] D.O. Caldwell, Mod. Phys. Lett. **10A** (1987) 772.

[58] R.S. Longacre, Phys. Rev. **D42** (1990) 1874.

[59] J. Weinstein and N. Isgur, Phys. Rev. **D27** (1983) 588.
J. Weinstein and N. Isgur, Phys. Rev. **D41** (1990) 2236.

[60] J.Podolanski and R. Armenteros, Phil. Mag **45** (1954) 13.

[61] T. A. Armstrong et al., Z. Phys. C **56** (1992) 29.

[62] R. Ehrlich et al., Phys. Rev. Lett. **20** (1968) 686.

[63] F. James, FOWL, CERN Computer Centre W505 (1977).

[64] F. James and M. Roos, MINUIT Computer Physics Communications **10** (1975) 343.

[65] K. McDonald, Properties of the Maximum liklihood method, CALT-68-321.

[66] S. M. Flatté, Phys. Lett. **63B** (1976) 224.

[67] D. Morgan, Phys. Lett. **51B** (1974) 71.

[68] S.U. Chung et al. Proc. of EPS conference, Bari (1985) 318.

[69] J. Iizuka et al. Phys. Rev. **36D** (1987) 1422.

[70] W. Beusch, Omega Prime, **CERN/SPSC/77-70** (1977).